Magnetic Resonance Imaging of Flow Instabilities

By

Heather E. L. Rose

A thesis submitted to
The University of Birmingham
For the degree of
DOCTOR OF PHILOSOPHY

School of Chemistry
College of Engineering and Physical Sciences
The University of Birmingham
February 2013

Abstract

This research project investigated the formation of flow instabilities and probed this formation using Magnetic resonance imaging. The coupling of hydrodynamic instabilities was investigated with regards to four different systems.

The formation of 3-dimensional viscous fingers has been investigated in a packed bed using magnetic resonance imaging. Fingering patterns are produced as a result of two different chemically reactive interfaces and one non-reactive interface. By the formation of a highly viscous wormlike micelle solution formed at the interface between solutions of cetyltrimethylammonium bromide (CTAB) and sodium salicylate (NaSal) viscous fingers were produced under flow. Both a non-reactive and reactive system with a pre-existing viscosity gradient, which remains unchanged throughout the experiment, is studied. The structure of the fingering patterns, which were found to be sensitive to flow rate, were analysed using histogram plots characterising the distribution of pixels containing High signal fluids. We also present an alternative method for plume visualisation and direct measurement of velocities within a solution of *Chlamydomonas nivalis cells.* We have carried out experiments to investigate the applicability of magnetic resonance imaging to investigate behaviour in this system.

Dedicated to

S.I.Rose

Acknowledgements

First and foremost, I would like to thank my supervisor, Dr Melanie M. Britton, for giving me the opportunity to undertake this research. I would also like to thank her for the great deal of support and advise she has given me throughout my PhD.

I would like to thank my parents for their help and support throughout every wild and wacky challenge I have set myself, including my PhD. I would also like to extend that gratitude to the rest of my family, who have been there through thick and thin, with a special mention to Aunty June for just being great.

I would like to thank Jan, Nicola, Sue, Matt, Ismalia, Catherine and Christian and everyone past and present on the second floor for putting up with me. With a special thanks to Antoine, Amanda and Charlotte, for putting up with me even more than everyone else. I would also like to thank all of my friends who have been great fun over the years, there are too many of you to mention by name but it’s been a blast! With a special thank you to Cristina (¡gracias), Jan, Milla, Jess and Helen. Also not forgetting Rob, who as well as being a brilliant friend has allowed me to treat him like my personal IT consultant.

I would like to thank Dr Martine Bees and Dr Otti Croze for their support during the work carried out for the bioconvection chapter of this thesis.

To everyone at the BGI past and present a big thank you. From the management who have been very understanding of my high work load, everyone front of house (including Geoff) for making my shifts so much more enjoyable and everyone in the kitchen for making me smile even when I have had the worst day and finally a special mention for Bill and Ben who always raise a smile.

To Tony, Cheryl, Jack, Jessica and Holly thank you for all your support and for providing a home from home when I have needed to unwind.

I would like to thank all the support staff from the chemistry department for all their support especially Steve the glassblower for the countless little jobs, many at the last minute, and for many, many cups of tea, Stuart for his regular guidance and Graham Burns who's advice was invaluable at the beginning of my research.

A thank you to all the staff and cadets, some gone but not forgotten, of 479 (Rubery) ATC with a special thanks to Sarah, Andy and Ben.

I owe special thanks to Waheed, who encouraged me to undertake my studies at The University of Birmingham.

And finally I would like to thank my husband, Richard who has supported me throughout my PhD, the ups, the downs and the in-betweens.

List of figures

Contents

1 Introduction

In nature there are many incidences where there is perturbation of flow. These perturbations are referred to as flow instabilities and arise due to variations of different parameters across the fluid. There are many different types of flow instabilities which can occur, determined by a variety of controlling parameters. These can include shear velocity, Kelvin-Helmholtz instabilities[1], surface tension, Marangoni convection perturbations[2], density, Rayleigh-Taylor instability[3] and viscosity, Saffman-Taylor instabilities[4] to name just a few.

1.1 Flow instabilities

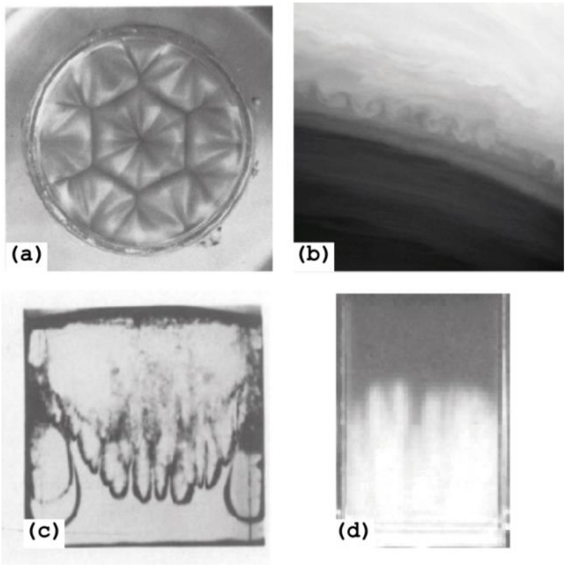

Figure 1.1 (a) A photograph showing the formation of Marangoni convection patterns in a layer of silicon oil heated from below. Reprinted from Physical letters, 112A, 8, Cerisier et. al A New Experimental Method To Select Hexagonal Patterns In Bernard-Marangoni Convection,366-370., Copyright (1985), with permission from Elsevier[5] (b)A photograph showing the formation of Kelvin-Helmholtz instabilities between the atmospheric layers of Saturn[6]. Courtesy NASA/JPL/Space Science Institute, (c) A photograph showing the displacement of ethanol by air through a Hele-shaw cell. Reprinted from Physica, 12D, Read, Experimental Investigation of Turbulent Mixing by Rayleigh-Taylor Instability,45-58, Copyright (1984), with permission from Elsevier[3] (d) A photograph showing the displacement of sugar cane by dyed water through a thin packed bed. Reprinted from Chemical Engineering Science, 1 /6, Hill, Channelling in Packed columns,247-253., Copyright (1952), with permission from Elsevier[7]

Figure 1.1 shows several examples of flow instabilities. Figure 1.1(a) shows the Marangoni instabilities which form when silicon oil is heated from below by a metal plate[5]. The variation of temperature across the liquid leads to different regions of fluid having different surface tensions. Areas of high surface tension, the cooler regions, draw liquid away from the hotter regions which have a lower surface tension. As the liquid moves away from the low surface tension regions, fluid is drawn from below to replace it, setting up cyclic convection conduits. It is this that creates the hexagonal patterns seen in Figure 1.1(a). The cloud formation seen in Figure 1.1(b)[6] shows an entirely different complex pattern being formed, the Kelvin-Helmholtz instability. This cloud formation, observed between the atmospheric bands of Saturn, is the result of shear forces. The shear force experienced as one atmospheric layer passes over another, emphasizes any bulges at the interface, due to a pressure drop, creating these "breaking wave" patterns. Both of these instabilities result due to an externally applied parameter, whereas the instabilities shown in Figure 1.1(c and d) result from the properties of the fluids themselves. The finger formation (Figure 1.1 (c))[3] is the result of two fluids of varying density coming into contact under flow. This branching structure forms when a less dense fluid, in this case air, drives a more dense fluid, ethanol, or a heavy fluid is placed above a lighter fluid, under gravity[3]. Similarly, Saffman-Taylor instabilities are fingers produced when a less viscous fluid displaces a more viscous fluid, through a porous media[8]. An example of this is shown in Figure 1.1 (d) [7]. Dyed water was used to displace a viscous sugar solution through a packed bed constructed of glass beads as a model for the purification of sugar cane.

These are just a small sample of the vast number of instabilities that can occur, and to make the variety even greater, these instabilities can be coupled with other influential factors. With flow instabilities it can be much more complex than one single force or fluid property influencing the flow. Shear velocities can couple with density[1] to emphasis wave formation, Marangoni convection patterns can be altered by changing the viscosity of the fluid[9] and even the presence of swimming microorganisms can alter the velocities in simple pipe flow[10].

1.2 Coupling chemistry with flow

A branch of research has developed where this coupling has been between chemistry and flow[11-17]. Chemical reactions can produce products that alter the physical and chemical properties of a system[18-20]. These chemical reactions can affect the structure of the flow and in turn, the flow within a system can affect the chemical reaction. Much work has focused on how flow in a system affects the chemistry[21, 22]. Oscillating chemical reactions, such as the *Belousov–Zhabotinsky (BZ)* reaction, are a perfect example of how flow and chemistry can be coupled. The BZ reaction is a complex reaction, of which a comprehensive description can be found elsewhere[23]. As the reaction moves towards equilibrium a metal catalysis oscillates between two states, such as Fe^{2+} and Fe^{3+}, creating optical contrast, and through the reaction-diffusion of products, across a fluid system, chemical patterns can be observed. When coupled with plug flow through a packed bed the chemical patterns become spatially distributed[24] and the patterns formed can be altered by changing factors such as flow rate, initial chemical concentrations and temperature[15]. Other flow systems, such as Taylor curette flow, have also been coupled with the BZ reaction in order to further understand not only the reaction but also the flow[12].

Here, the reverse is investigated where chemistry is employed to influence the flow of a fluid, specifically concentrating on the inclusion of a chemical reaction at the interface between two fluids, to induce or alter Saffman-Taylor instabilities.

1.3 Saffman-Taylor instabilities

Viscous fingers, also commonly referred to as Saffman-Taylor instabilities, occur when a less viscous fluid displaces a more viscous fluid through a porous media[7]. These instabilities are not only of interest due to their dynamic nature, but also as analogues for systems such as growth in microorganism colonies[25], finger growth in combustion[26] and the structure of lava flows[27]. Much comparison has also been made between viscous fingering and factual formations such as Diffusion limited aggregation[28]. Although the discovery of this instability is attributed to Saffman and Taylor[4] the first detailed experimental investigation of this system was carried out by Hill[7]. Although the phenomena was well known in various fields[4], Hill investigated the, sometimes inefficient, processes of sweetening on and off, whereby concentrated cane sugar solutions were added and removed from porous columns for the purpose of purification. During sweetening on, water in the column was displaced by the sugar cane solution and for sweetening off, water displaces the sugar cane solution already in the column. A subsequent feature of these processes was the lowering of sugar cane concentration in the final solutions. Hill investigated this by systematically running scaled down experiments and optically imaging the movement of eluent through ‘transparent’ columns. The sweetening off of sugar cane, where water displaced the sugar cane solution, revealed a breakdown of the horizontal interface between the two solutions. Hill showed the channeling of the water into and through the more viscous sugar solution. The reverse system, sugaring on, where sugar cane solutions displaced the water also showed the formation of channels but only over a given velocity[7]. From Hill’s experiments it became clear that not only does viscosity play a role in the formation of instabilities, but also the arrangement of the solutions is influential. It was Saffman and Taylor that brought together mathematical analysis and the use of Hele-shaw cells for visualization[4].

1.3.1 Finger formation

Finger formation is affected by several influential factors. Differences in dynamic viscosity, the force required to overcome the internal forces within a fluid[29], and the packing structure of a porous media both influence the formation of fingers. The packing of porous media can be described using the terms porosity and permeability. Porosity is the amount of void space in a porous media[30] whereas the permeability is a measure of a mediums ability to allow a fluid to flow through it[30]. Whether a fluid is Newtonian or non-Newtonian also affect the instabilities which form. A Newtonian fluid displays a linear relationship between its viscosity and the shear applied to it whereas the viscosity of a non-Newtonian fluid is dependent on shear[29].

Darcy's law describes how fluids flow through a porous medium[8] and relates the pressure gradient, ∇p, with the velocity, U, the dynamic viscosity of the fluid, μ, the permeability of the medium, k, the density of fluid, ρ, and gravity, **g**. Eq 1.1 is Darcy's law in one dimension

$$\frac{dp}{dx} = -\frac{\mu U}{K} + \rho g \qquad 1.1$$

To determine whether an instability will form and develop in a flow system, eq 1.2 is used to calculate the pressure force, δp, over a given distance, where p_1 is the pressure of the displaced fluid and p_2 the pressure of the driving fluid. If the pressure force is positive, a perturbation at the interface will develop into a finger[4].

$$\delta p = p_2 - p_1 = \left[\frac{(\mu_1 - \mu_2)U}{K} + (\rho_2 - \rho_1)g\right]\delta x \qquad 1.2$$

Depending on the arrangement of fluids, with regards to each other and gravity, factors such as velocity, gravity and viscosity can be both stabilizing and destabilizing. In Figure 1.2 a schematic of vertical flow, where a dense, more viscous fluid (black) is displaced by the downward flow of a less dense/viscous fluid (grey) is shown.

Figure 1.2: A schematic diagram showing the development of a viscous finger over time. Where a more dense/viscous fluid (black) is displaced by a less dense/viscous fluid (grey).

If a given parameter, such as the difference in viscosity between the fluids, is positive then it destabilizes the system and encourages finger formation, and the opposite is true for negative values. In this case $\mu_1 - \mu_2$ is positive and $\rho_2 - \rho_1$ is negative. Therefore, in this case gravity is negative and stabilizing due to a less dense fluid displacing a more dense fluid in the direction of gravity, whereas viscosity $(\mu_1 - \mu_2)$ is positive and destabilizing. For the system to be unstable overall and a finger to form the velocity, U, needs to exceed a given value, the critical velocity, U_c. The critical velocity needs to be large enough to counteract the stabilizing effect of gravity and is defined by eq 1.3[8].

$$\boldsymbol{U_c = -\frac{(\rho_2 - \rho_1)gK}{(\mu_1 - \mu_2)}} \qquad 1.3$$

Viscosity, gravity and velocity obviously all influence whether a finger will be formed under flow. This therefore dictates the properties and arrangement of the fluids required for instabilities to form.

1.3.2 Visualization of Fingering

Traditionally viscous fingers are difficult to visualize due to the opaque nature of porous media. The Original study by Hill[7] used photographic images of Perspex vials, with a thickness of 25 mm, packed with glass beads of diameter 0.4 mm to monitor instability formation[7]. Colored water was used to enable the two fluids to be distinguished. However, only instabilities at the outer walls were visible in the images. The proposal for the use of a Hele-Shaw cell was on the basis that the cell was a model porous medium. However it is a rather simplified model which is at best, a pseudo 2 dimension experiment[4].

1.3.2.1 Hele-shaw cell

A Hele-Shaw cell consists of two glass sheets separated by a small gap, b, which is typically less than 1 mm[31]. The gap between the two plates mimics the porous nature of a system, and is related to the permeability, k, by eq 1.4 [8].

$$\boldsymbol{K} = \frac{\boldsymbol{b}^2}{\mathbf{12}} \qquad 1.4$$

Hele-shaw cells can take several arrangements including the radial and rectangular flow shown in Figure 1.3. The benefits of using a Hele-Shaw cell is that it is easy to visualize fluid within the system and can be set up horizontally, therefore removing the effect of gravity.

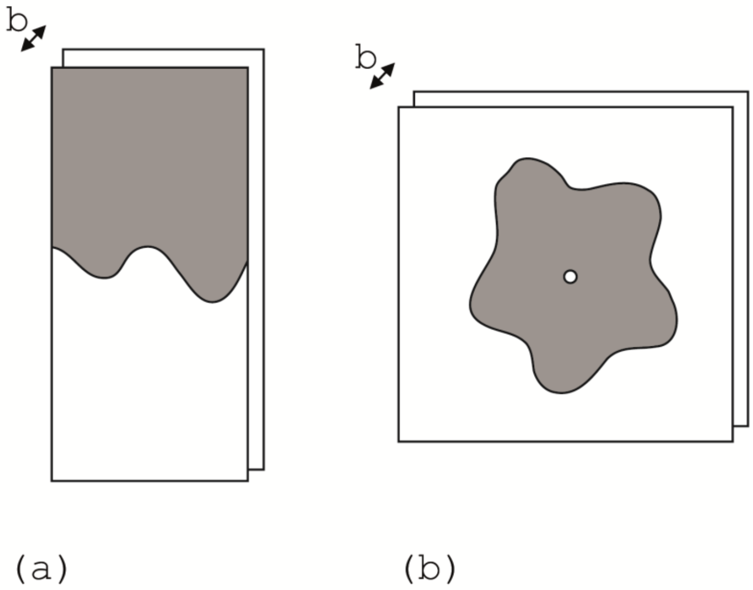

Figure 1.3: A Schematic diagram showing two possible arrangements for a Hele-Shaw cell with rectangular (a) and radial (b) flow.

The benefit of Hele-Shaw cells is that easy visualisation enables study of specific flow behaviour and finger development[32]. Finger formation and development can be characterised by several different methods. Originally the width of a stable finger, λ, was found to be dependent, when the viscosity of the driving fluid was negligible and the fluids were immiscible, on the capillary number, C_a, (eq 1.5) where μ is the viscosity of the displaced fluid, U the velocity of the finger and T the interfacial tension between the fluids[33]. As C_a approaches zero, the viscosity or finger velocity decreases or the interfacial tension increases, then λ increases giving a broader, less defined finger.

$$c_a = \mu U/T \qquad 1.5$$

This analysis however, does not apply to fingers that are not at steady state or characterise features such as finger tip-splitting or other factual behaviour that may be seen. These more detailed features of unstable fingers are described using the terms shielding, splitting and spreading[8]. As deviations at the interface develop, due to a positive pressure gradient, it is not only a single finger that is formed. Several perturbations will develop into fingers initially but one finger will dominate the system and accelerate in front of the others. This shielding effect was visualised by Maxworthy *et. al* when investigating fingering in Rayleigh-Taylor instabilities[34]. It was found that as one finger dominates it grows slightly longer that the others, due to small differences at the initial interface. That finger creates unsteady flow that stabilises the fingers behind it. As the finger grows this stabilising effect increases. This shielding leads to the one single finger which accelerates away from the interface spreading in width. This finger however does not remain stable. On reaching a critical width determined by the width of the

Hele-Shaw cell[35] the tip of the finger becomes unstable and splits into multiple fingers[36-38]. The process of shielding again dominates and the cycle of shielding, spreading and splitting begins again.

1.3.2.2 Porous media flow

The flow in a Hele-Shaw cell can be described using Darcy's law with regards to one and two dimensions but not when it is in three dimensional media. The Hele-Shaw cells fail to simulate the restricted nature of a porous media filled with miscible fluids[8]. In a Hele-Shaw cell flow is restricted effectively to 2 dimensions and takes no account of the tortuous nature of a 'real' porous media.

1.3.2.3 Imaging in-situ

The limited ability of Hele-shaw cells to model the flow behavior in porous media and the requirement of good color contrast for optical measurements has led to the use of alternative methods of visualization for finger formation in porous media. Several techniques have been employed to visualize opaque systems, such as packed bed reactors. Barci *et. al* were the first to carry out analysis of three-dimensional viscous fingering in a packed bed[39, 40]. They used an acoustic method to obtain one-dimensional averages, showing the concentration profiles through the porous media. Using this method, the effect of flow rate and viscosity variations were observed. It was confirmed experimentally that the increase of viscosity and flow rate enhanced the growth of fingers[40]. While no optical contrast was required for this experiment, only one-dimensional data was provided which gave little detail about the finger structure. Shalliker *et. al* used optical imaging to analysis viscous fingering in size exclusion chromatography[41-44]. Increasing the viscosity of the displaced fluid was again found to increase the occurrence of instability formation. Again there were limitations to the experiments. While detailed optical images of finger formation were obtained, the experimental setup was complex and only systems with optical contrast could be used.

Magnetic resonance (MR) imaging was also employed to image real porous media, to improve the understanding and visualization of viscous fingers[45]. The very first experiments, carried out by Davies[45], utilizing MR imaging in these systems actually looked at Hele-shaw cells rather than a 3-dimensional porous media. The cells were visualized using a MR technique that exploited different relaxation properties of the system to obtain contrast[45], meaning that no optical contrast was required. Images were obtained of a non-Newtonian gel, carboxymethylcellulose, being displaced by manganese doped water solution. While showing the imaging capabilities of the technique, drawbacks such as long acquisition times, ~70 seconds, and diffusion of the MRI contrast agent, manganese, through the system were highlighted. Further studies concentrated on in-situ visualization of size exclusion chromatography where the dilution of samples, through instability formation had become an issue. Fernandez *et. al* used glycerol as a model compound and Bovine serum albumin as a model macro molecule to further investigate instabilities in porous media[46]. With the aim of reducing the occurrence of instabilities, several investigations were carried out to characterize the effect of viscosity[46], flow rate[46] and structure of the porous media[47, 48]. Increased viscosity of the more viscous fluid was shown experimentally to agree with Darcy's law, with increased viscosity leading to more pronounced fingers. Increased flow rate also shows the same trend[46]. Fernandez *et. al* were the first to construct three dimensional images of these instabilities in situ[48].

All Fernandez’s work focuses on non-reactive systems and in some cases moved away from using MRI and involved other imaging techniques[49]. In this project we propose the use of 2-dimensional and 3-dimensional MRI techniques to visualize a variety of system where viscous fingering occurs.

1.4 Reactive interfaces

Most research has relied on fluids which have intrinsically different viscosities, however, in this thesis focus is on more complex systems whereby reactive interfaces influence the physical properties of the system, altering or inducing the formation of viscous fingers. Nagatsu *el. al*[50] carried out one of the first experimental studies of miscible viscous fingering with the inclusion of a chemical reaction. The displacement of 97% glycerol by a less viscous solution was combined with the reaction of iron(III) nitrate and Potassium thiocyanate (KSCN), and visualized optically in a Hele-Shaw cell. It was found that the inclusion of the reaction altered the pattern formation seen under flow, although little explanation is given as to why. It was also seen that the structure of the viscous fingers formed was dependent on reactant concentration[50] and flow rate[51].

Further studies were also carried out by Nagatsu *et al.* into systems where a pre-existing viscosity gradient was coupled with a chemical reaction[18, 52]. The Reactive interfaces were found to reduce the shielding behavior of fingers by instantaneously increasing the viscosity of the more viscous fluid. This was achieved by utilizing the dependence of viscosity of some polymer solutions on pH[52].

1.4.1 Alteration of porous media structure

While these chemical reactions have been included to induce changes in the viscous fingers, chemical reactions can also change the physical structure of the Hele-Shaw cell or porous media[18]. The reaction between iron(III)nitrate and potassium hexacyanoferrate(II), shown in eq 1.6, results in the formation of the precipitate, iron(III) hexacyanoferrate(II).

$$Fe^{3+}(NO_3)_3 + K_4[Fe^{2+}(CN)_6] \rightarrow KFe^{3+}[Fe^{2+}(CN)_6] + 3KNO_3 \qquad 1.6$$

When this reaction is included in the displacement of glycerol by a less viscous solution, in a Hele-Shaw cell the formation of precipitate at the interface has been shown to stop the ability of fingers to undergo splitting[18]. This is due to the restrictive nature of a solid interface. Weaknesses in the interface are exploited by the flow, enabling the fingers to develop, but the instability shape is greatly affected. When the concentration of the reactants is high enough the flow in the system is restricted causing straight, extended fingers to form. With even higher concentrations of precipitate, the restrictive nature of the interface can completely change the direction of flow leading to jagged fingers being formed[18], shown in Figure 1.4 .

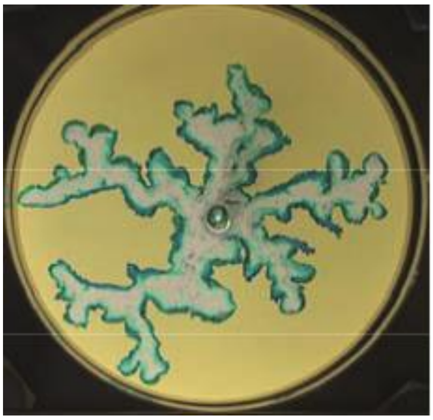

Figure 1.4: Optical image of effect of Precipitate formation of flow instabilities in a Hele-Shaw cell. Reprinted figure 5d with permission from Miscible viscous fingering with a chemical reaction involving precipitation, Nagatsu et. al, PHYSICAL REVIEW E, 77, 067302,3,2008. Copyright (2008) by the American Physical Society.

It is however, important to note that not all viscous finger-producing systems require a pre-existing viscosity gradient, when a reactive interface is included in the system.

1.4.2 Reaction induced viscosity gradients

Podgorski *et. al* found experimentally[53] and De Wit *et. al* theoretically[20] that when two miscible fluids of similar viscosity reacted to form a third, highly viscous fluid, the formation of viscous fingers can be induced[54]. Recent studies, both experimental[18, 54, 55] and theoretical[56, 57], have shown the development of viscous fingers in a Hele-Shaw cell where no viscosity gradient is initially present.

The formation of wormlike micelles by the mixing of the surfactant, Cetyltrimethylammonium bromide (CTAB), Figure 1.5(a), and co-surfactant, sodium salicylate, Figure 1.5(b), is an example of such a system.

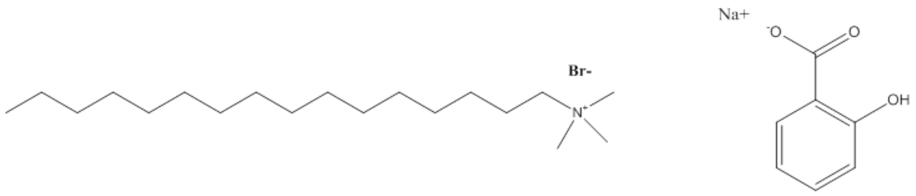

(a) (b)

Figure 1.5: Schematic diagrams for the chemical structure of (a) Cetyltrimethylammonium bromide (b) sodium salicylate.

Separately, both solutions have a viscosity not dissimilar to water[54], but on contact form wormlike micelles. Wormlike micelles are a highly viscous non-Newtonian fluid that forms when a surfactant is mixed with a co-surfactant, which then screens the long range electrostatic repulsion of the head group on the surfactant. This results in the formation of wormlike micelles form rather than spherical micelles[58]. In the study carried out by Podgorski *et. al*, stoichiometric ratios of the chemicals were used with concentrations and flow rates altered systematically. Finger shape and development was found to be influenced by increasing concentration or input flow rate[54].

Figure 1.6[54], taken from the original Hele-shaw cell study, shows the effect of increased flow rate.

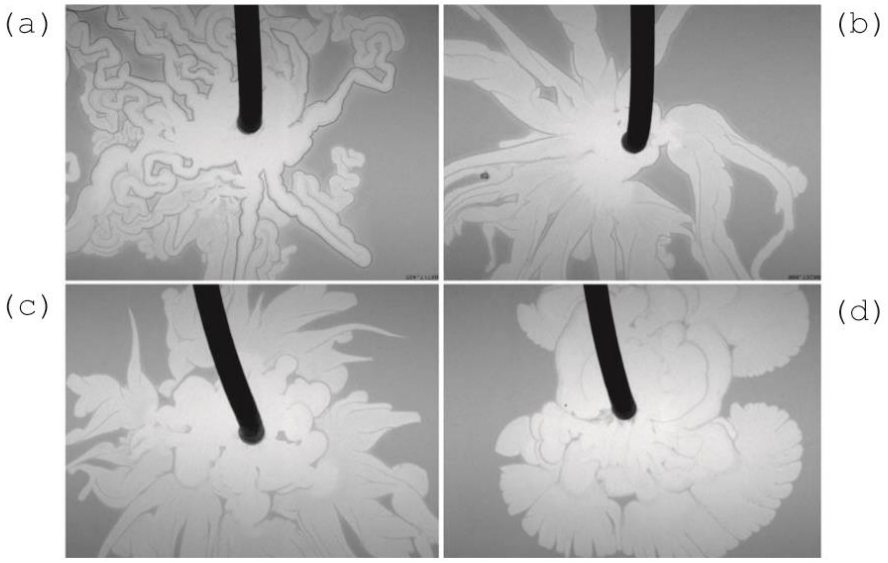

Figure 1.6: Patterns formed in a Hele-shaw cell when 50mM CTAB is injected into 50 mM sodium salicylate at a rate of (a) 20, (b) 50 ,(c) 100 and (d) 200 ml/hr. Reprinted figure 3 with permission from Fingering instabilities of a reactive micellar interface, Podgorski et. al, PHYSICAL REVIEW E, 76, 016202,3,2007. Copyright (2007) by the American Physical Society.

As the flow rate is increased, instabilities are seen to evolve from narrow, finger-like tendrils to broad, blooming mushroom shapes. The behavior seen in this study contradicts the results from studies into both reactive and non-reactive systems, whereby it is the higher flow rates which produce the narrower, faster moving fingers. This contraction can be explained due to the development of the interface. At the lower flow rates the interface has greater time to develop, making it thicker and more capable of restricting flow to a given path. While the fingers are clearly visible the Hele-Shaw cell experiments still do not provide a true representation of behavior in ‘real’ porous media. Several fields of science involve the combination of reactive interfaces and ‘real’ porous media. Extraction methods used in oil fields include the use of viscoelastic solutions to drive oil through the rock bed[59]. On contact with hydrocarbons the viscosity of the driving fluid reduces leading to more efficient fluid extraction and prevents the porous rock remaining occupied by the driving fluid after oil extraction. The transport of bacteria through subsurface environments can also be considered as a reactive system moving through porous media[60]. Chemical and physical properties of the porous media influence the position and growth of bacteria as water flows through the system. While these two systems are very different they both show how reactive interfaces can combine with porous media and flow. The varied occurrences of reactive interfaces in porous media make it desirable to understand further the ways in which reactive interfaces influence flow in such systems.

1.4.3 Motivation for research

While much work has been carried out to understand the formation of viscous fingers in reactive and non-reactive systems, much is still not understood about the complex finger formations. In this thesis the reactive systems investigated by Nagatsu et. al[18] and Podgorski et al[53], where precipitate formation and the development of a visco-elastic interface, will be investigated. To further develop on the work previously carried out, MR imaging will be used to investigate finger development in a 3-dimensional packed bed reactor.

1.5 Nuclear magnetic resonance

Nuclear magnetic resonance (NMR) is the fundamental technique on which magnetic resonance (MRI) is based. MRI is a non-destructive/non-invasive technique and can be used to probe optically opaque systems making it ideal for the investigation of the human body[61-63] but also in-situ analysis of chemical reactions and processes particularly in porous media[13, 64-67]. This chapter will provide an introduction to the various MR techniques used in this project. For a more detailed explanation of NMR and MRI there are a variety of informative text books[68-71].

MRI exploits an ability to manipulate the nuclear spins of nuclei by the application of external magnetic fields and radio frequency (rf) pulses. The technique requires nuclei with nuclear angular momentum, most typically ^1H.

1.5.1 Theory of nuclear magnetic resonance

For nuclei to be NMR active they must possess nuclear spin and so nuclear angular momentum, **P**. Angular momentum arises due to the presence of unpaired nucleons, protons and neutrons, in the nuclei. Each unpaired proton or neutron provides a spin of $I= ½$, with the overall spin of a nucleus being the sum of these. The nuclear angular momentum is a vector quantity and so possesses magnitude and direction. With the nuclei spinning and also possessing a charge, a nuclear magnetic moment, $\boldsymbol{\mu}$ is generated. The angular momentum and the magnetic moment of a nucleus are related (eq (1.7) by the gyromagnetic ratio (γ) which provides a measure of how strongly magnetic the nucleus is.

$$\mu = \gamma \boldsymbol{P} \qquad 1.7$$

1.5.1.1 Nuclear spin

The most commonly used nucleus in the field of NMR is ^1H, which has one unpaired proton and hence a nuclear spin of

I = ½. When placed in a static magnetic field (**B₀**), the nuclear spins align either with or against the direction of **B₀**. The number of orientations, and hence energy levels, allowed is determined by the spin quantum number I, with $(2I + 1)$ levels possible. In an external magnetic field, the nuclear spin energy levels (m_I) are non-degenerate. ^{1}H nuclei have two possible orientations: $m_I = -1/2$ (spin-up) and $m_I = +1/2$ (spin-down) which are separated by an energy gap, ΔE.

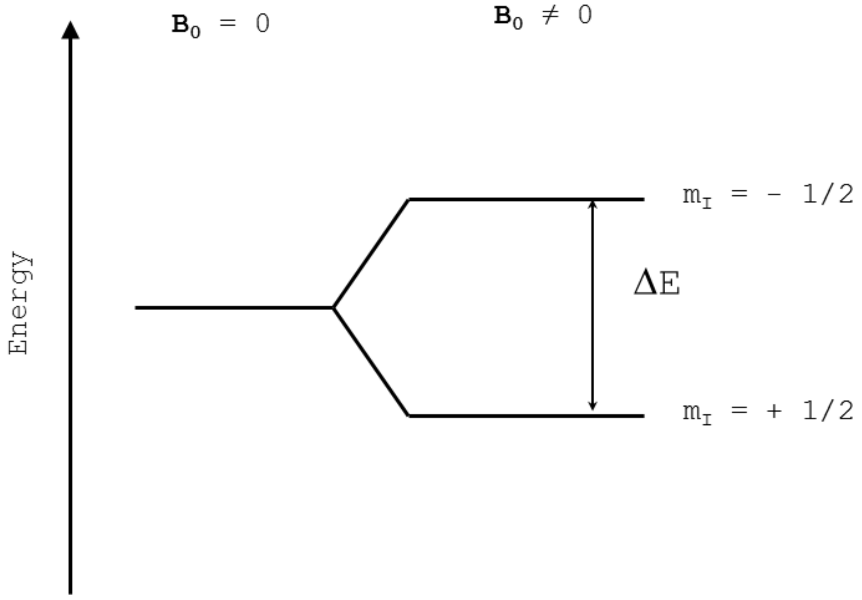

Figure 1.7: Energy level diagram for $I = 1/2$ nuclei

Nuclei distribute between these two energy levels according to the Boltzmann distribution[72] (eq 1.8), where $N_{1/2}$ and $N_{-1/2}$ are populations of the spin up and spin down states energy levels respectively, k is Boltzmann constant and T the temperature.

$$\frac{N_{-1/2}}{N_{+1/2}} = e^{-\Delta E/kT} \qquad 1.8$$

As ΔE is relatively small, the populations of each energy level are almost equal, with only a slight excess of spin-up nuclei.

In an external magnetic field, nuclei experience a torque force which results in precession about the axis of the applied field. The frequency of precession is determined by γ and $\boldsymbol{B_0}$, (eq 1.9 (in rad s^{-1}) or (eq 1.10 (in Hz)) and is known as the Larmor frequency.

$$\omega = \gamma B_0 \qquad 1.9$$

$$\nu = \frac{\gamma B_0}{2\pi} \qquad 1.10$$

The Larmor frequency is related to the energy difference, ΔE, between the spin states by eq 1.11, where h is Plank's constant.

$$\Delta \mathrm{E} = h\nu = \frac{h\gamma B_0}{2\pi} \qquad 1.11$$

An ensemble average of the spin vectors in a system results in a macroscopic magnetisation (**M_0**) aligned with **B_0**, (figure 1.8). It is this vector that is manipulated in NMR experiments and results in the NMR signal.

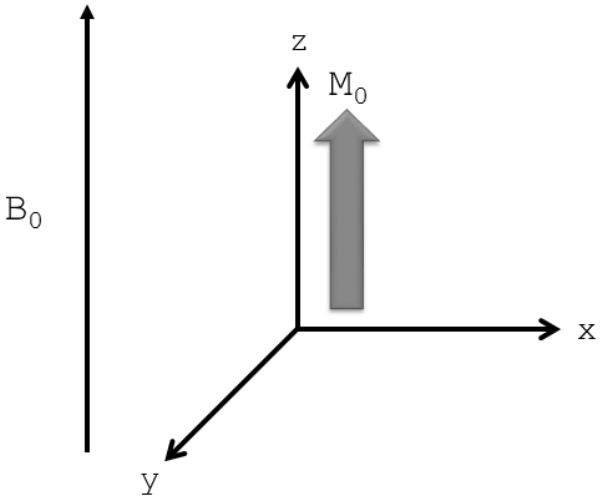

Figure 1.8: A schematic diagram of the orientation of M_0 with regards to the magnetic field, B_0.

By using radio frequency (rf) pulses of the appropriate frequency, the distribution of spins between the energy levels can be manipulated resulting in a deflection of **M_0**. The power and duration of the rf pulses leads to the flipping of **M_0** about the *z, x, y* axis.

1.5.1.2 NMR pulses

The NMR signal is produced only when the magnetisation vector is in the transverse plane. The rf pulses that are employed to manipulate the magnetisation originate from the rf coil, and only pulses at the Larmor frequency will induce the transitions of spins between the two spin states and alter the orientation of **M₀**. The amount by which **M₀** is deflected is known as the tip angle, θ. This tip angle is dependent on the magnitude, ***B₁***, and duration, t_p, of the pulse. The tip angle, as shown in eq 1.12, is defined in degrees.

$$\theta = \frac{360\gamma}{2\pi} B_1 t_p \qquad 1.12$$

Most NMR pulse sequences require a combination of 90° and 180° pulses, their names defined by their effect on the direction of **M₀**. Flowing a radio frequency pulse, nuclei in the system will return to thermal equilibrium and result in **M₀** returning to its original orientation. After a 90° rf pulse, spins have phase coherence, which is where all spins align along a specific direction on the transverse plane. Following the rf pulse, spins lose phase coherence, and will start to dephase within the transverse plane. Each process has characteristic time constants which are defined as the T_1 and T_2 relaxation times, of the system. Relaxation processes will be explained in greater detail later in this chapter.

1.5.1.3 Rotating Frame

After the application of a $90°_x$ pulse $\mathbf{M_0}$ will be located on the *y* axis initially and precess at the Larmor frequency. It is deviation from this initial state which is of interest, but also makes the system more complex to work with. For simplification a *x,y* rotating frame is used. The *x,y* axis rotate at the *L*armor frequency of a reference within the sample. All the spins rotating at this frequency will then appear stationary and are said to be “on-resonance”. Spins that precess at a different frequency to that of the reference will appear to rotate either clockwise or anti clockwise with respect to the rotating frame.

1.5.1.4 NMR signal and Free induction decay

The NMR signal is produced when the magnetisation vector is in the transverse plane. While in the transverse plane, the magnetisation will precess and induce a small oscillating voltage in the rf coil. This oscillating current is the NMR signal, known as the free induction decay (FID). As can be seen from Figure 1.9 the oscillating signal reduces in amplitude over time, which is due to the loss of magnetisation in the transverse plane. The relaxation process will be discussed later in further detail.

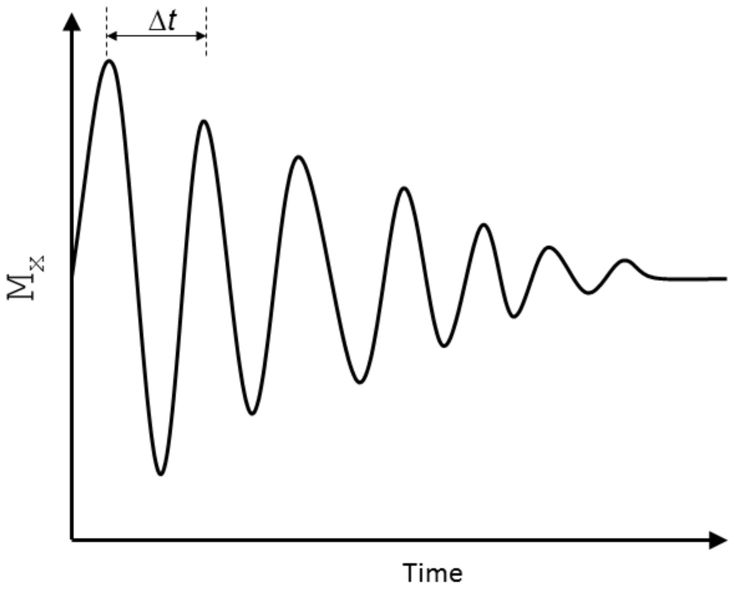

Figure 1.9: A schematic of the Free Induction Decay, showing the magnetisation along the x axis, M_x, as a function of time

The signal received by the rf coil, is collected and amplified before being digitized. The NMR signal is in the time domain and then needs to be converted into the frequency domain in order to produce a spectrum. There is an inverse relationship between these domains, given by eq 1.13 where Δt is the period of the oscillation and ν the frequency of the corresponding peak in a spectrum. Fourier transformation of the time domain data results in the frequency domain data.

$$\nu = \frac{1}{\Delta t} \qquad 1.13$$

1.5.2 Relaxation processes

Following a r.f. pulse, $\mathbf{M_0}$ will return to thermal equilibrium through the relaxation processes T_1 and T_2.

1.5.2.1 T_1 relaxation/ spin-lattice Relaxation

While $\mathbf{M_0}$ is aligned along the direction of the $\mathbf{B_0}$ field, which is typically defined as the *z* axis, it is also denoted as $\mathbf{M_z}$. After the application of a $90_x°$ pulse, there will be no magnetisation along *z*, and hence $\mathbf{M_z} = 0$, however $\mathbf{M_y} = \mathbf{M_0}$ as the magnetisation will be aligned along the *y* axis. The system has been moved away from thermal equilibrium and over time must return to its original spin arrangement. The return to thermal equilibrium is facilitated by interactions between the nuclei and the lattice around it. As shown by eq 1.14 the time taken for $\mathbf{M_z}$ to return to thermal equilibrium is controlled by the time constant, T_1, and this process is exponential in nature.

$$M_z = M_0\left(1 - e^{-t/T_1}\right) \qquad 1.14$$

Following a 90° pulse, $\mathbf{M_z}$ will start to increase until thermal equilibrium is re-established. This is shown in Figure 1.10. The T_1 of nuclei is dependent on the spectrometer frequency (ω) and the physical environment and chemical composition of the system.

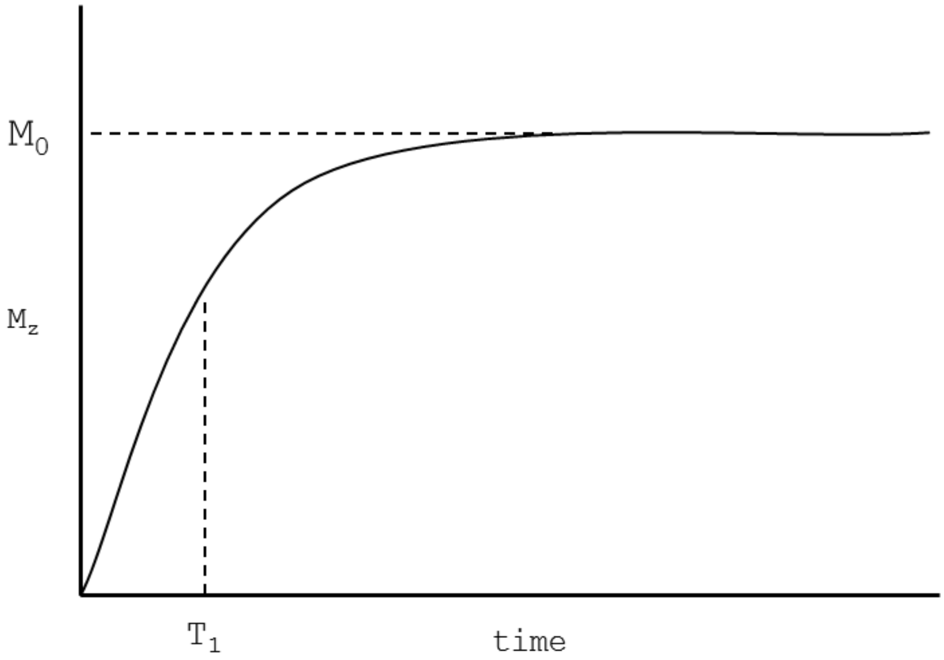

Figure 1.10: A plot showing the exponential recovery of magnetisation (M_z) along the z axis.

1.5.2.2 *T_2 relaxation/ spin-spin relaxation*

Following a 90° rf pulse, the magnetisation is on the transverse plane, where the spins will have phase coherence. Phase coherence is where all spins contributing to the transverse magnetisation are orientated along the same axis and, at that point of time, precess at the same rate resulting in the summation of the spin vector in to one single vector in the transverse plane. Over time, the spins de-phase due to the influence of non-uniform magnetic fields and the magnetic influences of neighbouring molecules. As a result the NMR signal in the transverse plane reduces in amplitude[73]. This relaxation process is called spin-spin relaxation, and is governed by a time constant, T_2. It is important to note that this relaxation process occurs simultaneously with spin-lattice relaxation and that the value of T_2 cannot exceed that of T_1. Here we denote $\boldsymbol{M_0}$ on the transverse plane as $\mathbf{M_{xy}}$. This process is exponential in nature, as shown by eq 1.15 and as time progresses there is a decrease in the amplitude of $\mathbf{M_{xy}}$.

$$M_{xy} = M_0 e^{-t/T_2} \tag{1.15}$$

Spin-spin relaxation is governed by two key factors, inhomogeneity in $\boldsymbol{B_0}$ and molecular interactions. As shown in eq 1.16, contributions of this inhomogeneity towards the measured T_2^*, are governed by the time constant $T_{2(\Delta \boldsymbol{B}_0)}$.

$$\frac{1}{T_2^*} = \frac{1}{T_2} + \frac{1}{T_{2(\Delta B_0)}} \tag{1.16}$$

As $T_{2(\Delta B_0)}$ arises due to hardware influences, actions can be taken to reduce the effect, therefore reducing $T_{2(\Delta B_0)}$. Shimming coils are integrated into the spectrometer's probe, the section which houses the sample. These coils carry small, controllable electrical currents that generate small magnetic fields which help compensate for $\boldsymbol{B_0}$ inhomogeneities.

For spectroscopy we are much more interested in the dephasing of spins due to molecular interactions, the intrinsic T_2 rather than $T_{2(\Delta B_0)}$. The magnetic environment of a spin is dependent on its surroundings, and in this case its proximity to molecules affecting the local magnetic field. Through employing specific pulse programs we can tailor our experiments to give accurate values of T_2.

1.5.3 MR experiments

Magnetic resonance experiments can be used to acquire a variety of information about a chemical system. Spectra showing the connectivity of a molecule, spin-echo or Carr, Purcell, Meiboom and Gill (CPMG) experiments measuring the T_2 of a system and inversion recovery experiments measuring T_1 are all examples of MR experiments that can provide information about a system.

Through a combination of various pulses some form of magnetisation will be bought onto the transverse plane where a current is then induced in the rf coil and an NMR signal is recorded. The simplest of these sequences is the pulse acquire where a 90_x° is applied and the NMR signal recorded immediately after. Multiple repetitions of these pulse programs can result in the improvement of the signal to noise ratio but signal amplitude is also dependent on the number of spins present, the T_1 of the system and the repetition time between repeats.

1.5.3.1 Spin-echo

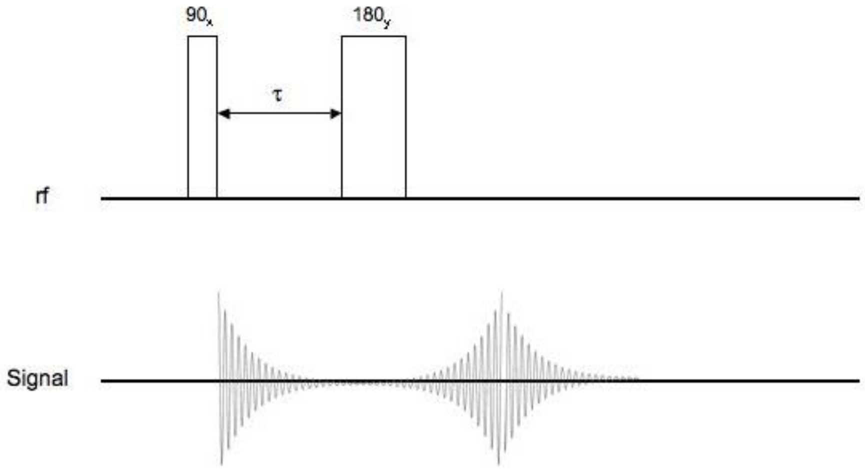

Figure 1.11 As schematic diagram showing the spin-echo pulse program

The spin-echo pulse sequence, shown in Figure 1.11, forms the basis of many pulse sequences used in spectroscopic and imaging experiments. After the $90_x°$ pulse brings $\mathbf{M_0}$ into the xy plane the spins begin to lose phase coherence due to T_2 relaxation and is shown by the decaying FID in figure 1.11. Using a $180_x°$ pulse the magnetisation of the spins are flipped about the x-axis. They will continue to dephase, but now their direction of dephasing has been reversed and their continued dephasing refocuses the echo. This pulse sequence was originally known as the Hahn experiment[73].

A limitation with measuring T_2 in this manner is that the technique is sensitive to magnetic field inhomogeneity and so the inclusion of T_2*. The diffusion of spins between the $90_x°$ and $180_x°$ pulses means that when the $180_x°$ pulse is applied the spins will not fully refocus. The Hahn experiment was further developed by Carr, Purcell, Meiboom and Gill[74]. In their sequence, multiple 180° pulses are used which repeatedly refocus the magnetisation, reducing the effect of dephasing due to ΔB_0. This experiment has become known as the CPMG experiment.

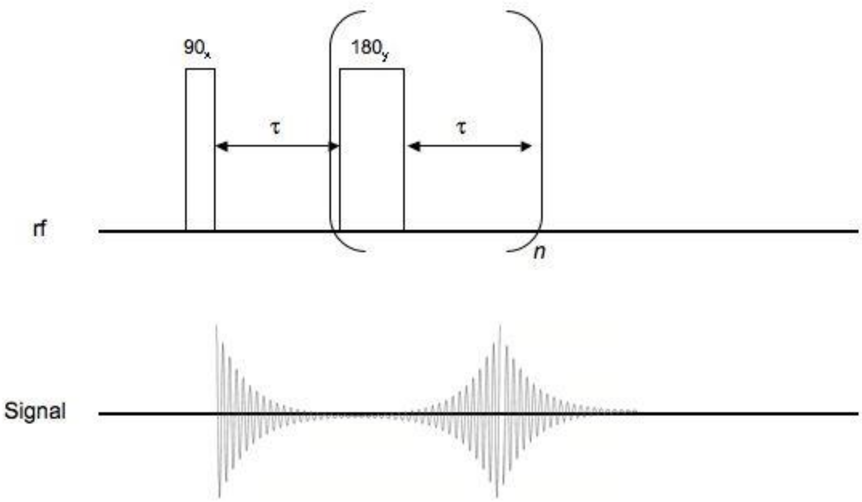

Figure 1.12 A schematic diagram of the CPMG pulse sequence

From Figure 1.12, it can be seen that the 180_y° pulses are repeated multiple times, *n*. The repetitive refocusing of spins gives a series of refocused echoes, shown in Figure 1.13, the decay of these multiple echoes can be fitted to acquire T_2, rather than a T_2*.

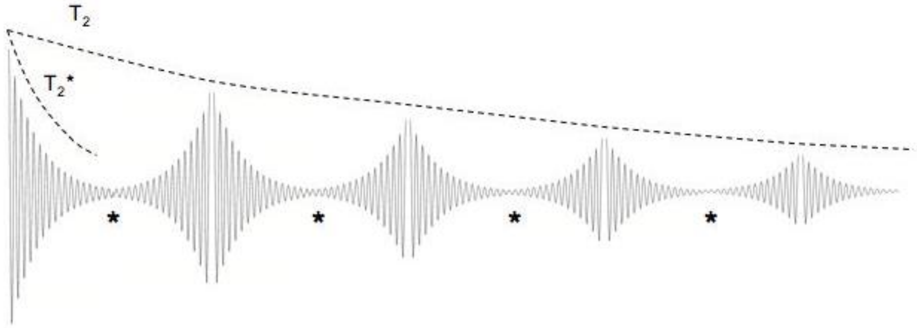

Figure 1.13 A schematic diagram showing the refocused FIDs obtained during a CPMG sequence. The * represents the position of the refocusing 180° pulse and the dotted lines represent the T_2^* and T_2 decays.

1.5.3.2 *Inversion recovery*

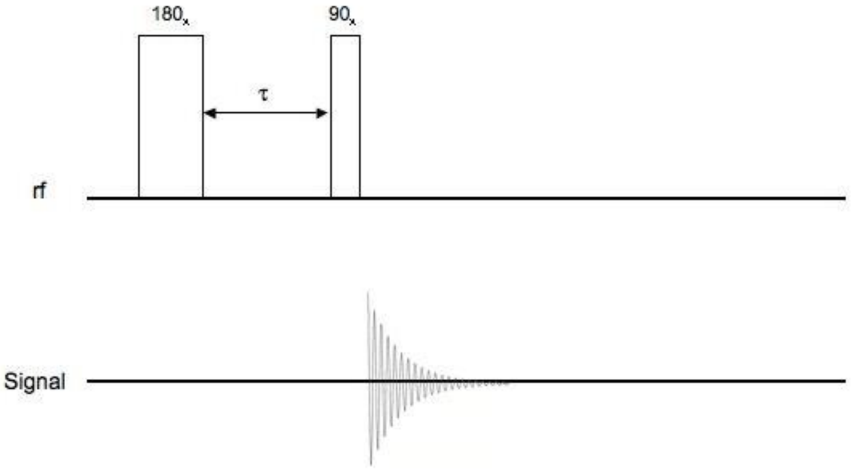

Figure 1.14 A schematic diagram showing the inversion-recovery pulse program. The 180° pulse brings the magnetisation vector on to the –z axis. The spins then return to thermal equilibrium before a 90° pulse brings the magnetisation onto the transverse plane and a FID can be acquired.

The T_1 inversion-recovery experiment is a method used to measure T_1 relaxation. From the pulse sequence in Figure 1.14 it can be seen that the initial pulse used is a $180_x°$ pulse rather than $90_x°$ as in the spin-echo sequence. This takes $\mathbf{M_0}$ from the $+z$-axis to the $-z$-axis. After the $180_x°$ pulse, the system will begin to return to thermal equilibrium through a redistribution of spins between the two energy levels. The time taken for this to happen is dependent on T_1 and can be monitored by varying the time delay, τ, between 180° and 90° pulses, allowing re-establishment of $\mathbf{M_0}$ to be followed. The $90_x°$ pulse brings the recovered $\mathbf{M_0}$ vector onto the x,y plane where it can be recorded as the NMR signal. By using multiple acquisitions of varying values of τ the recovery of $\mathbf{M_0}$ can be measured and plotted and T_1 determined by fitting to eq 1.14.

1.6 MRI

While NMR is able to acquire bulk measurements of chemical and physical properties, magnetic resonance imaging (MRI) is able to spatially resolve these properties through the inclusion of magnetic field gradients. These gradients allow the precessional frequency of spins to be dependent on their position, allowing the construction of images, where the distribution of signal intensity is dependent on factors such as spin density, relaxation times and molecular motion.

1.6.1 Magnetic field gradients

When a magnetic field gradient is applied the Larmor frequency, $\omega(_r)$, of spins becomes spatially dependent, with a linear relationship between $\omega(_r)$ and ***r***, where ***r*** is the position of spins along the direction of the magnetic field gradient (eq. 1.17).

$$\omega(\mathrm{r}) = \gamma \mathrm{B}_0 + \mathrm{gG} \bullet \mathrm{r} \qquad 1.17$$

G is the gradient of the static $\mathbf{B_z}$ and can be defined along the three Cartesian axes (eq 1.18 – 1.20).

$$X \text{ direction: } \boldsymbol{G_x} = \frac{d\boldsymbol{B_z}}{dx} \qquad 1.18$$

$$Y \text{ direction: } \boldsymbol{G_y} = \frac{d\boldsymbol{B_z}}{dy} \qquad 1.19$$

$$Z \text{ direction: } \boldsymbol{G_z} = \frac{d\boldsymbol{B_z}}{dz} \qquad 1.20$$

When a magnetic field gradient is applied along a sample, the spins are often referred to as spin packets, which are ensemble averages of localised spins.

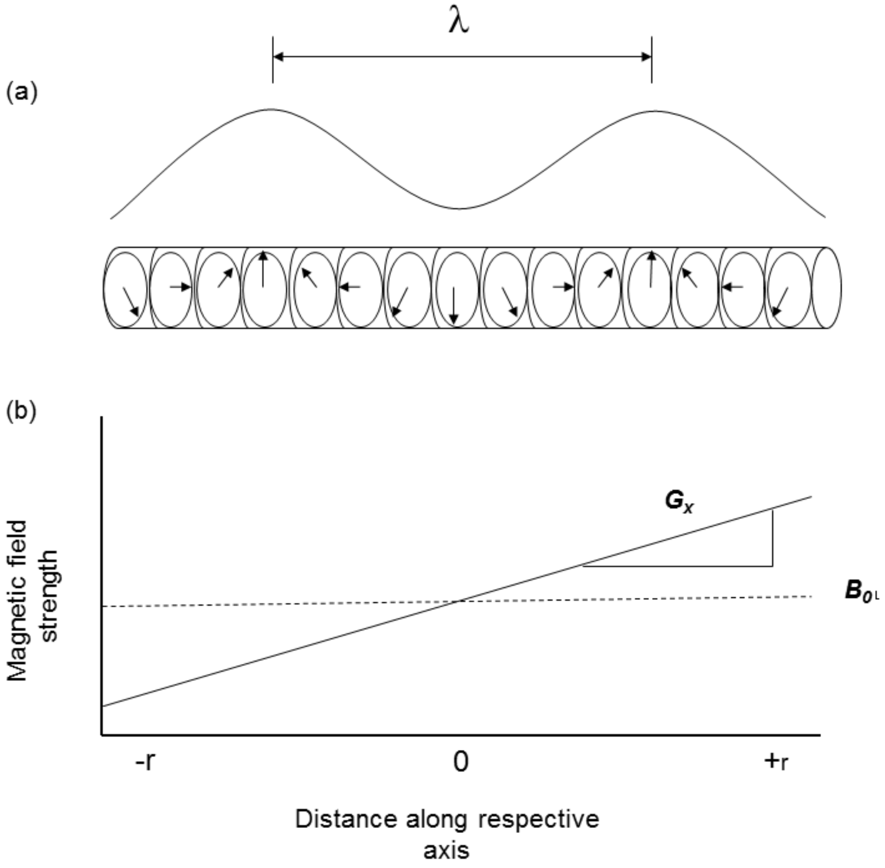

Figure 1.15:(a) Schematic diagram showing the effect of a magnetic gradient on the Larmor frequency for a series of spin packets. (b) Plot showing the relationship between the static magnetic field, B_0, and B_z as a function of a applied magnetic gradient, G_x.

In Figure 1.15 (a), the frequencies of spins within a sample are shown to be dependent on position. The helix of phase formed is directly related to the applied magnetic gradients shown in Figure 1.15 (b). By measuring

ω, and Fourier transforming, it is possible to map the position of these spins and construct an image. To create a 2D image, gradients in two directions are required. This can be done by using the reciprocal space vector, $\boldsymbol{k}$, (eq 1.21) which is related to the wavelength, λ, (eq 1.22) for the helix of spins wound by the magnetic field gradient (Figure 1.15).

$$k = (2\pi)^{-1}\gamma G t \qquad 1.21$$

$$\boldsymbol{k} = \lambda^{-1} \qquad 1.22$$

The $\boldsymbol{k}$-space vector is the reciprocal of λ (eq 1.22) and therefore traversing $\boldsymbol{k}$-space enables the navigation of real space required to construct an image. $\boldsymbol{k}$ is proportional to the gradient strength and time. By varying these factors $\boldsymbol{k}$-space can be traversed by either a progression in time or gradient magnitude. To help visualise this we use a $\boldsymbol{k}$-space raster, (Figure 1.16). The centre of the raster corresponds to $\boldsymbol{k}=0$ where all spins are focused. Utilising the dependence of $\boldsymbol{k}$ on gradient strength and time, $\boldsymbol{k}$-space can be navigated. To move along the x-axis known as the read direction a technique called frequency encoding is employed. To move in the *y*-axis, known as phase direction a second technique known as phase encoding is used. Multiple techniques are required as, to construct a multi-dimensional image, differentiation between the various directions traversed is needed.

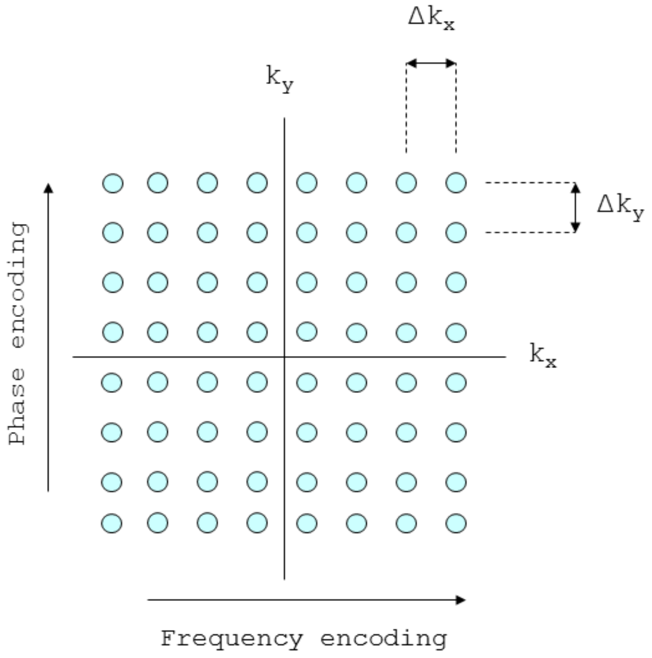

Figure 1.16 A schematic representation of a *k*-space raster.

1.6.2 Frequency encoding

Frequency encoding encodes for position directly by applying a gradient and measuring the different frequencies while the gradient is on and so traverses ***k***-space through progression in time. A magnetic gradient is applied while the signal is acquired. While the magnetic gradient is maintained $\omega(_{r})$ is dependent on position. As time progresses the read (*x*) axis of ***k***-space is traversed (Figure 1.17).

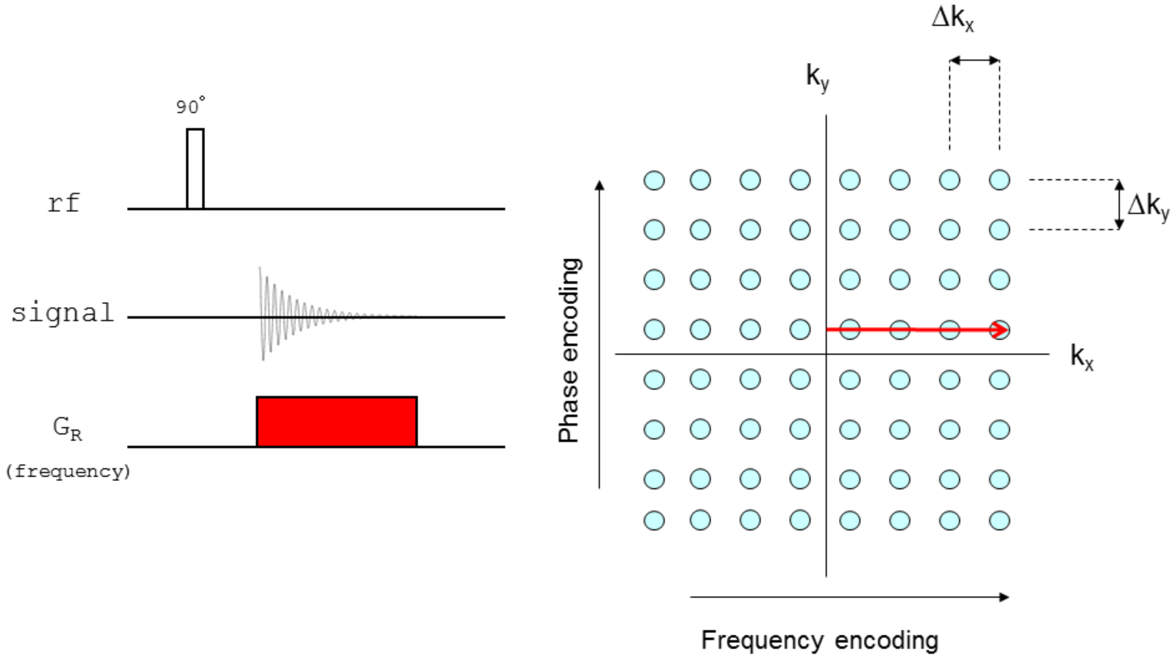

(a) (b)

Figure 1.17: (a) the basic components of a 2D imaging sequence required to navigate positive k-space by frequency encoding. (b) a k space raster showing how read gradients result in movement across k-space

While the gradient is on, the signal acquired is for a 'full' line of ***k***-space and requires only a single acquisition. To acquire frequency data from the ***-k*** area of the raster a "precursor" read gradient is applied.

This is directly before, and half of the area of, the standard read gradient. While providing a method for the acquisition of negative ***k***-space, the left hand side of the ***k***-space raster, this "precursor" gradient means that data collection starts at the outer regions of ***k***-space. The dead time before a gradient can lead to some dephasing and signal loss. The outer regions of ***k***-space make less contribution towards the final image than the centre of ***k***-space, minimising the effect of gradient dead time on the final image.

1.6.3 Phase encoding

To acquire a two-dimensional image, the ***k***-space raster must be traversed along a second axis using phase encoding. In phase encoding the gradient is applied before the signal is acquired for a fixed time, but at varying amplitudes (Figure 1.18).

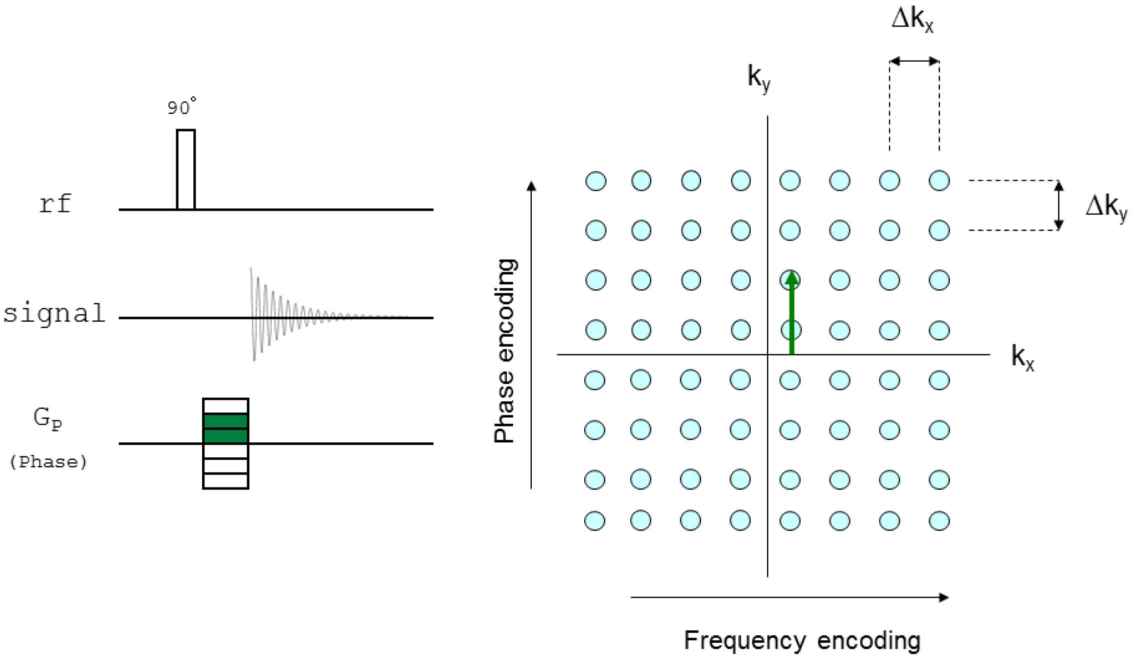

(a) (b)

Figure 1.18: (a) the basic components of a 2D imaging sequence required to navigate positive k-space by phase encoding. (b) A k space raster showing how phase gradients result in movement across k-space

By applying a gradient of negative or positive sign at different amplitudes different lines in the ***k***-space raster are selected. Negative and positive gradient increments navigate the negative and positive areas of k-space respectively. While the gradient is applied, the frequency of the spins is spatially dependent. Once the gradient is switched off, the spins precess at the same frequency but the phase of the spins is different. It is this difference in phase that provides the spatial information. A secondary phase gradient can be included when acquiring a 3-dimentional image.

1.6.4 Slice selection

Two-dimensional images are typically acquired by selecting a slice and then encoding in the two directions. These slices can be of any orientation, with a specified position and thickness. Soft rf pulses are frequency selective pulses that excite a specific range of frequencies depending on the duration of the pulse. The magnetic field gradient is applied perpendicular to the required slice, frequency encoding the position of each spin packet. By then applying a frequency selective soft pulse only spin packets with specific frequencies will be excited, leading to only a slice of specific position and thickness being imaged. The spread of frequencies is inversely proportional to the length of a r.f. pulse. Therefore short “soft” pulses will excite a wide range of frequencies with increased duration leading to thinner slice selections.

1.6.5 Spin-Echo Imaging

Spin echo imaging sequences are the most commonly imaging sequences used when investigating porous media. Spin-echo sequences are based on the basic 90 – 180 rf pulse sequence. In this thesis we acquire images using the

RARE[75] pulse sequence which will be described later in this thesis.

1.6.5.1 Spin echo

Spin echo pulse programs use phase and frequency encoding gradients to navigate ***k***-space as described previously. A simple spin-echo, slice selective pulse sequence is shown in Figure 1.19.

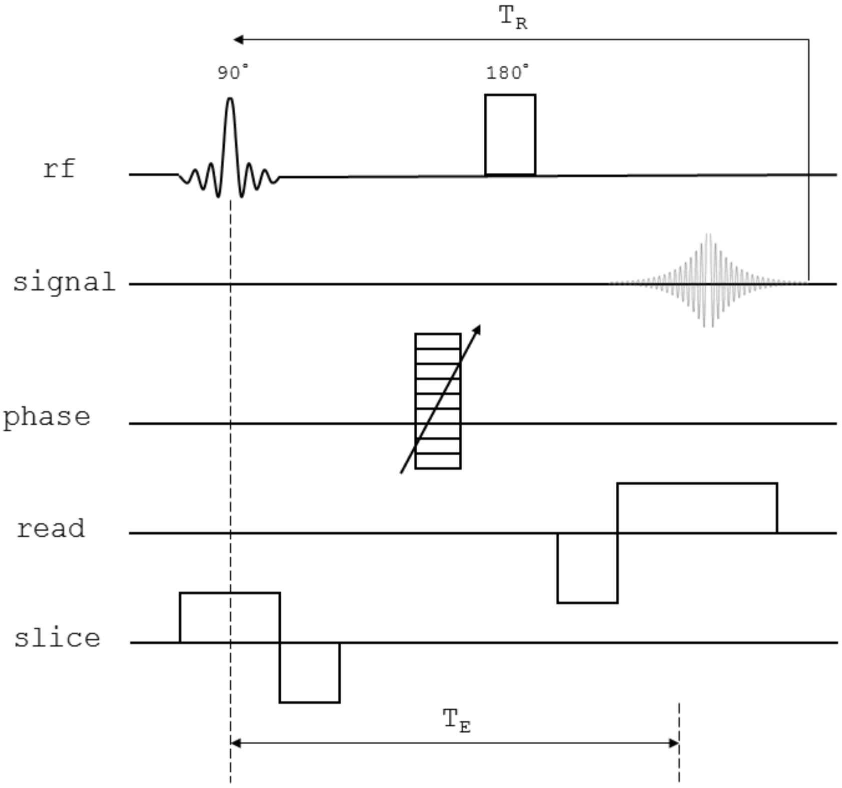

Figure 1.19: A schematic diagram showing a spin-echo imaging pulse sequence. The magnetisation is deflected onto the transverse plane by the 90° pulse. A combination of phase and frequency encoding gradients acquire NMR signal for each image pixel.

Specific alterations to the spin echo pulse program will be discussed with reference to their specific contrast capabilities.

1.6.6 Experiment time

The time it takes to acquire an image is dependent of several factors. The number of phase pixels, N_{pe}, is important as each data point much be acquired separately. The number of scans, N_{rep}, and also the repetition time, T_r contribute to the overall experiment time. An approximate experiment can be calculated using eq 1.23.

$$Experiment\ time = N_{pe} \times T_r \times N_{rep} \qquad 1.23$$

1.6.7 Image contrast

To enable useful information to be obtained from an MR image, there needs to be a method for distinguishing between different regions within the sample giving rise to image contrast. There are several parameters that can be used to create image contrast, with the most common being spin density, relaxation, chemical shift and motion.

i. Spin density

The number of spins in a pixel creates contrast in an image. The more spins, the higher the spin density the greater, the signal from that pixel. Spin density images are produced in spin echo images by keeping T_E much shorter than T_2 and T_R greater than 5 x T_1, so removing relaxation effects.

ii. T_1 and T_2 Relaxation

By altering the parameters of a spin echo experiment contrast can be produced from T_2 and/or T_1 relaxations. These images are known as parameter weighted images. By extending T_E so it approaches T_2 and keeping T_R longer than 5 x T_1, the influence of T_1 becomes negligible and the image is T_2 weighted. Alternatively if both T_E and T_R are kept short then the images become T_1 weighted. This type of contrast becomes important when images are required to distinguish between areas of varying chemical environments but with comparable spin densities. As well as images weighted by relaxation measurements, relaxation maps can be acquired for both T_1 and T_2. In this work we have only acquired T_2 maps. This is done acquiring multiple images with varied T_E. By analysing how the signal of each pixel changes between the images the T_2 decay of each pixel can be calculated and a T_2 relaxation time assigned to each specific pixel, creating the T_2 map.

iii. Chemical shift

When there is more than one chemical species present within a system there will be different chemical shifts and so different Lamour frequencies. This means that the frequencies in the system are no longer purely dependent on position. This can create problems when imaging, namely artefacts, but can also be used to create image contrast. Data needs to be acquired in a 4th dimension where chemical shift information is encoded. This can be done by either using a chemically selective pulse, which will only excite the chemical species of interest or a complete spectrum can be acquired for each pixel.

iv. Motion

By manipulating the helix of spins wound by the magnetic field gradients it is possible to monitor the movement of these spin packed. Movement of spin packed can result in increased or reduced signal. Both coherent motion, flow, and incoherent motion, diffusion, can be monitored using a pulsed gradient spin echo pulse ,PGSE, program.

1.6.8 RARE Imaging

All the systems studied in this project are subjected to flow, and as a result long experimental times can result in the blurring of images. To shorten the experiment time and reduce the occurrence of image blurring the majority of imaging carried out in this project was done using the **R**apid **A**cquisition with **R**elaxation **E**nhancement (RARE)[75] pulse sequence, (Figure 1.20).

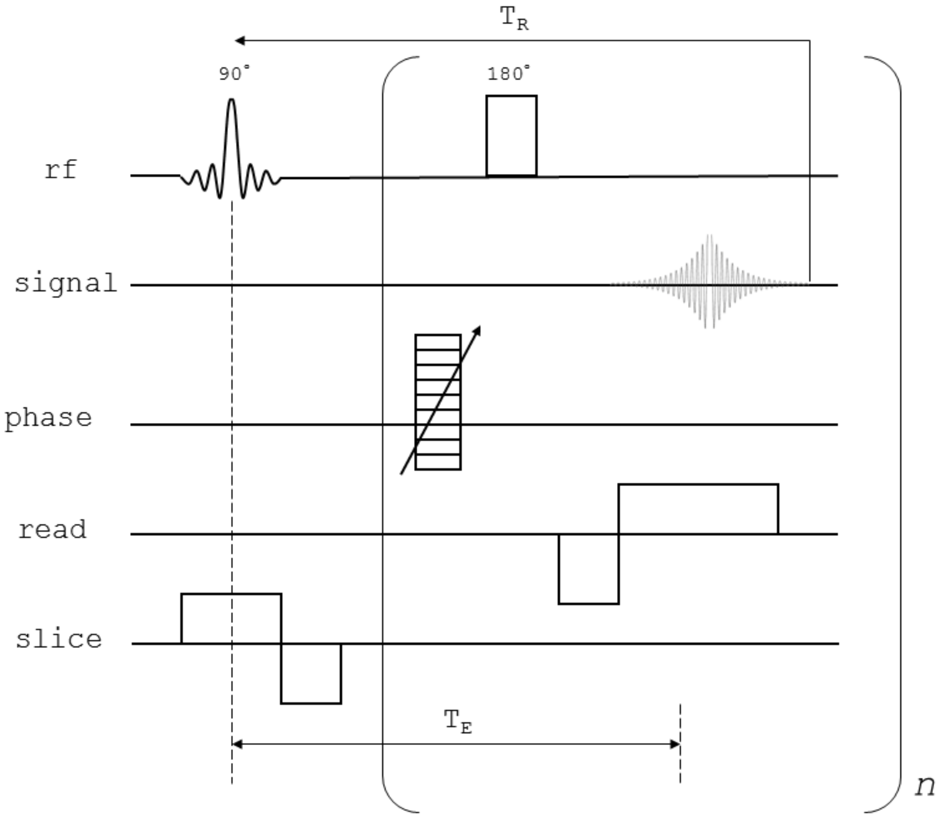

Figure 1.20: A schematic diagram showing a RARE[75] imaging pulse sequence. A *n* number of echoes are acquired for each excitation.

This imaging sequence provides a method for obtaining T_2 weighted images with a reduced experiment time. This is done by acquiring multiple echoes per excitation. The number of echoes acquired per excitation is the RARE factor. The higher the RARE factor the more echoes are acquired per excitation and the shorter the experiment time, eq 1.24.

$$Experiment\ time = \frac{N_{pe}}{RARE\ factor} \times T_r \times N_{rep} \qquad 1.24$$

As the RARE factor is increased there is a longer period between excitations. Species with a short T_2 are able to relax, and signal is lost, while signal is still seen from species with a longer T_2.

1.6.9 Pulsed gradient spin echo

To use motion for contrast in an MR image, spin packets within the system needs to be labelled in some way so that their movement can be monitored. We do this by using the **P**ulsed **G**radient **S**pin **E**cho (PGSE)[76] pulse sequence (Figure 1.21). Spin packet labelling is achieved through control of the phase shift.

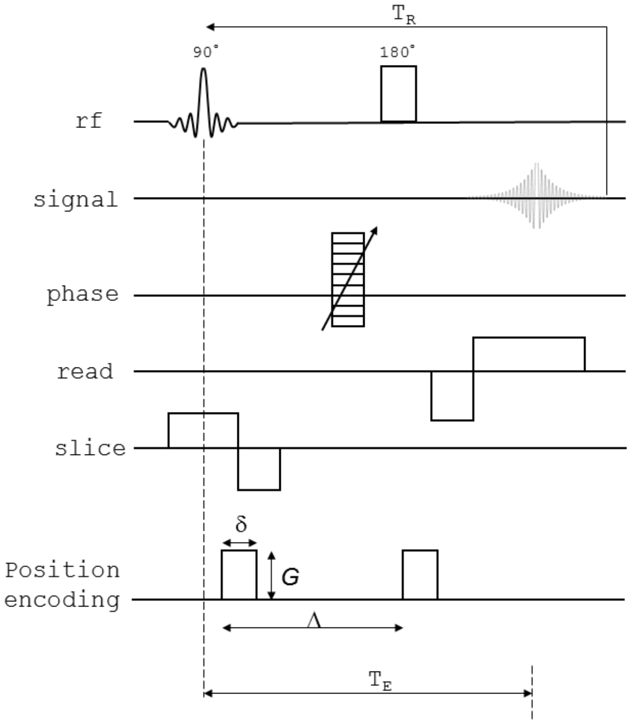

Figure 1.21 A Pulsed gradient spin echo pulse program. The two phase encoding gradients wind and unwind a helix of spin to determine motion within a system.

In addition to the imaging sequence already described there are two identical gradients of strength G, duration δ separated by delay of Δ. With the magnetisation bought down onto the transverse plane due to the initial 90° pulse, a helix of spin is wound by the first gradient of amplitude $\boldsymbol{G}$ and duration δ. If no flow was present and Δ was below the rate of diffusion the second, identical gradient, would "unwind" the helix of phase and there would be no attenuation of signal. By altering $\boldsymbol{G}, \delta$ and Δ

signal attenuation can provide information about coherent and non-coherent motion within the system.

1.6.9.1 Non-coherent flow

Non-coherent motion, diffusion, within a system can be characterized by attenuation of signal, when the Stejskal-Tanner relationship is satisfied (eq 1.25).

$$\frac{a_{\Delta}}{a_{\circ}} = \exp\left\{-\gamma^2 G^2 \delta^2 D\left(\Delta - \delta/3\right)\right\} \qquad 1.25$$

As *Δ* is increased the effects of diffusion become apparent in the signal acquired. Spins diffusing during the experiment are now in a different position when the second gradient is applied and therefore are not refocused, resulting in an attenuation of signal. The faster the rate of diffusion, or the longer *Δ*, the greater the degree of signal attenuation.

1.6.9.2 Velocity measurements

When coherent motion, flow, is present in the system the phase of the magnetisation in the transverse plane is shifted proportionally to the velocity of the flow (eq 1.26).

$$\varphi = \frac{\gamma v G_{\Delta} \delta \Delta}{2\pi} \times 360 \qquad 1.26$$

As previously shown **M$_0$** is brought down on to the transverse plane. The effect of gradient pulses on the phase of spins in motion is shown in figure 1.22.

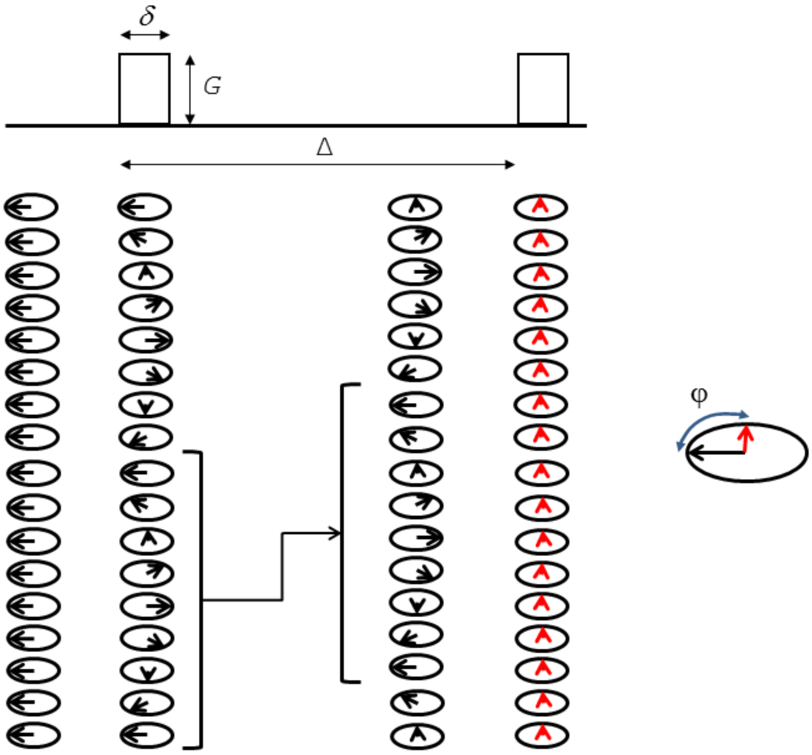

Figure 1.22: A schematic showing the relationship between the position encoding phase gradients of pulsed gradient spin echo and the spins along the axis of flow.

When considering only the effect of the two phase encoding gradients the effect of coherent flow on the helix of spins is clear. A coherent shift in spins results in all the spins being refocused, but all with a phase given phase shift. By spacially resolving these phase shifts images mapping the velocity of a flow system, can be constructed.

1.7 Focus of research

The aim of this research is to employ Magnetic resonance Imaging techniques to visualize the formation of hydrodynamic instabilities, namely flow instabilities influenced by viscosity differences, as well as other contributing factors. These experiments will be carried out in a 'real' porous media. The classic system of water driving glycerol will be imaged as will chemically reactive systems. A new analysis technique will be used to analyse and identify the formation and development of fingers through a packed bed reactor.

1.8 References

1. Hooper, A.P. and W.G.C. Boyd, *Shear-flow instability at the interface between two viscous fluids.* Journal of Fluid Mechanics, 1983. **128**: p. 507-528.
2. Scriven, L.E. and C.V. Sternling, *Marangoni Effects.* Nature, 1960. **187**(4733): p. 186-188.
3. Read, K.I., *Experimental investigation of turbulent mixing by Rayleigh-Taylor instability.* Physica D: Nonlinear Phenomena, 1984. **12**(1-3): p. 45-58.
4. Saffman, P.G. and G. Taylor, *The Penetration of a Fluid into a Porous Medium or Hele-Shaw Cell Containing a More Viscous Liquid.* Proceedings of the Royal Society of London Series a-Mathematical and Physical Sciences, 1958. **245**(1242): p. 312-329.

5. Cerisier, P., et al., *A new experimental method to select hexagonal patterns in Bénard-Marangoni convection.* Physics Letters A, 1985. **112**(8): p. 366-370.
6. Nasa. Available from: http://www.nasa.gov/images/content/556780main1_PIA06502-226.jpg.
7. Hill, S., *CHANNELLING IN PACKED COLUMNS.* Chemical Engineering Science, 1952. **1**(6): p. 247-253.
8. Homsy, G.M., *Viscous Fingering in Porous Media.* Annual Review of Fluid Mechanics, 1987. **19**(1): p. 271-311.
9. Selak, R. and G. Lebon, *Benard-Marangoni Thermoconvective Instability in Presence of a Temperature-Dependent Viscosity.* Journal De Physique Ii, 1993. **3**(8): p. 1185-1199.
10. Pedley, T.J. and J.O. Kessler, *Bioconvection.* Science Progress, 1992. **76**(299): p. 105-123.
11. Novak, J., et al., *Low frequency temperature forcing of chemical oscillations.* Physical Chemistry Chemical Physics, 2011. **13**(26): p. 12321-12327.
12. Thompson, B.W., et al., *Inward propagating chemical waves in Taylor vortices.* Physical Review E, 2010. **81**(4).
13. Britton, M.M., *Magnetic resonance imaging of chemistry.* Chemical Society Reviews, 2010. **39**(11): p. 4036-4043.
14. Taylor, A.F. and M.M. Britton, *Magnetic resonance imaging of chemical waves in porous media.* Chaos, 2006. **16**(3): p. 037103.
15. Toth, R., et al., *Flow-driven instabilities in the Belousov-Zhabotinsky reaction: Modelling and experiments.* Physical Chemistry Chemical Physics, 2001. **3**(6): p. 957-964.
16. Vallatos, A., et al., *Characterising stationary and translating vortex flow using magnetic resonance.* Epl-Europhys Lett, 2012. **99**(6): p. 68001.
17. Yang, J., et al., *Rayleigh-Taylor instability of reaction-diffusion acidity fronts.* Journal of Chemical Physics, 2002. **117**(20): p. 9395-9408.
18. Nagatsu, Y., et al., *Miscible viscous fingering with a chemical reaction involving precipitation.* Physical Review E, 2008. **77**(6): p. 067302.
19. Nagatsu, Y., et al., *Spiral pattern in a radial displacement involving a reaction-producing gel.* Physical Review E, 2008. **78**(2): p. 026307.
20. Nagatsu, Y., et al., *Experimental evidence of reaction-driven miscible viscous fingering.* 2012. **85**(1): p. 015304.
21. Kaern, M. and M. Menzinger, *Experiments on flow-distributed oscillations in the Belousov-Zhabotinsky reaction.* Journal Of Physical Chemistry A, 2002. **106**(19): p. 4897-4903.

22. McGraw, P.N. and M. Menzinger, *General theory of nonlinear flow-distributed oscillations.* Physical Review E, 2003. **68**(6): p. 066122.
23. Scott, S.K., *Oscillations, waves, and chaos in chemical kinetics.* Oxford chemistry primers1994, Oxford ; New York: Oxford University Press. 90 p.
24. Kaern, M. and M. Menzinger, *Flow-distributed oscillations: Stationary chemical waves in a reacting flow.* Physical Review E, 1999. **60**(4): p. R3471-R3474.
25. Goriely, A. and M. Tabor, *Self-similar tip growth in filamentary organisms.* Physical Review Letters, 2003. **90**(10): p. 4.
26. Zik, O., Z. Olami, and E. Moses, *Fingering instability in combustion.* Physical Review Letters, 1998. **81**(18): p. 3868-3871.
27. Griffiths, R.W., *The Dynamics of Lava Flows.* Annual Review of Fluid Mechanics, 2000. **32**(1): p. 477-518.
28. Ball, P., *The self-made tapestry : pattern formation in nature*1999, Oxford England ; New York: Oxford University Press. vi, 287 p.
29. Jim W Goodwin, R.W.H., *Rheology for chemists*2008: The royal society of chemists. 264.
30. Walker, P.M.B., *Larousse dictionary of science and technology*1995: Larousse.
31. Hele-Shaw, Transactions of Royal Institution of Naval Architects, 1898. **40**(21): p. 218-237.
32. Tanveer, S., *Surprises in viscous fingering.* Journal of Fluid Mechanics, 2000. **409**: p. 273-308.
33. SAFFMAN, P.G., *Selection Mechanisms and Stability of Fingers and Babblesin Hele-Shaw Cells.* IMA Journal of Applied Mathematics, 1991. **46**(1-2): p. 137-145.
34. Maxworthy, T., *The Nonlinear Growth of a Gravitationally Unstable Interface In a Hele-Shaw Cell.* Journal of Fluid Mechanics, 1987. **177**: p. 207-232.
35. Wooding, R.A. and H.J. Morelseytoux, *Multiphase Fluid-flow Through Porous-media.* Annual Review of Fluid Mechanics, 1976. **8**: p. 233-274.
36. Degregoria, A.J. and L.W. Schwartz, *A Boundary-integral Method For 2-phase Displacement In Hele-shaw Cells.* Journal of Fluid Mechanics, 1986. **164**: p. 383-400.
37. Tabeling, P., G. Zocchi, and A. Libchaber, *An Experimental-study Of The Saffman-taylor Instability.* Journal of Fluid Mechanics, 1987. **177**: p. 67-82.
38. Maxworthy, T., *Experimental study of interface instability in a Hele-Shaw cell.* Physical Review A, 1989. **39**(11): p. 5863-5866.
39. Bacri, J.C., et al., *Miscible Viscous Fingering - Experiments Versus Continuum Approach.* Physics of Fluids a-Fluid Dynamics, 1992. **4**(8): p. 1611-1619.

40. Bacri, J.C., D. Salin, and R. Woumeni, *3-Dimensional Miscible Viscous Fingering in Porous-Media.* Physical Review Letters, 1991. **67**(15): p. 2005-2008.
41. Catchpoole, H.J., et al., *Visualising the onset of viscous fingering in chromatography columns.* Journal of Chromatography A, 2006. **1117**(2): p. 137-145.
42. Shalliker, R.A., B.S. Broyles, and G. Guiochon, *Visualization of viscous fingering in high-performance liquid chromatographic columns - Influence of the header design.* Journal of Chromatography A, 1999. **865**(1-2): p. 73-82.
43. Shalliker, R.A., B.S. Broyles, and G. Guiochon, *Visualization of solute migration in liquid chromatography columns.* Journal of Chromatography A, 1998. **826**(1): p. 1-13.
44. Broyles, B.S., et al., *Visualization of viscous fingering in chromatographic columns.* Journal of Chromatography A, 1998. **822**(2): p. 173-187.
45. Davies, E.S., *Visualization of Viscous Fingering by Nuclear Magnetic Resonance Imaging.* Journal of Magnetic Resonance, 1992. **96**: p. 210-215.
46. Plante, L.D., P.M. Romano, and E.J. Fernandez, *Viscous Fingering In Chromatography Visualized Via Magnetic-Resonance-Imaging.* Chemical Engineering Science, 1994. **49**(14): p. 2229-2241.
47. Fernandez, E.J., et al., *A column design for reducing viscous fingering in size exclusion chromatography.* Biotechnology Progress, 1996. **12**(4): p. 480-487.
48. Fernandez, E.J., et al., *The Effects Of Permeability Heterogeneity On Miscible Viscous Fingering - A 3-Dimensional Magnetic-Resonance-Imaging Analysis.* Physics Of Fluids, 1995. **7**(3): p. 468-477.
49. Dickson, M.L., T.T. Norton, and E.J. Fernandez, *Chemical imaging of multicomponent viscous fingering in chromatography.* Aiche Journal, 1997. **43**(2): p. 409-418.
50. Nagatsu, Y., et al., *Experimental evidence of reaction-driven miscible viscous fingering.* Physical review E, 2012. **85**(1): p. 015304.
51. Nagatsu, Y. and T. Ueda, *Effects of finger-growth velocity on reactive miscible viscous fingering.* Aiche Journal, 2003. **49**(3): p. 789-792.
52. Nagatsu, Y., et al., *Experimental study on miscible viscous fingering involving viscosity changes induced by variations in chemical species concentrations due to chemical reactions.* Journal of Fluid Mechanics, 2007. **571**: p. 475-493.
53. Podgorski, T., et al., *Fingering instabilities of a reactive micellar interface.* Physical Review E, 2007. **76**(1): p. 016202.

54. Podgorski, T., et al., *Fingering instabilities of a reactive micellar interface.* Physical Review E, 2007. **76**(1).
55. Nagatsu, Y., et al., *Spiral pattern in a radial displacement involving a reaction-producing gel.* Physical Review E, 2008. **78**(2).
56. Gerard, T. and A. De Wit, *Miscible viscous fingering induced by a simple A plus B -> C chemical reaction.* Physical Review E, 2009. **79**(1): p. 10.
57. Nagatsu, Y. and A. De Wit, *Viscous fingering of a miscible reactive A+B -> C interface for an infinitely fast chemical reaction: Nonlinear simulations.* Physics of Fluids. **23**(4): p. 13.
58. Kim, W.J. and S.M. Yang, *Effects of sodium salicylate on the microstructure of an aqueous micellar solution and its rheological responses.* Journal of Colloid and Interface Science, 2000. **232**(2): p. 225-234.
59. Yang, J., *Viscoelastic wormlike micelles and their applications.* Current Opinion in Colloid & Interface Science, 2002. **7**(5-6): p. 276-281.
60. Zhang, H., N.A. Nordin, and M.S. Olson, *Evaluating the effects of variable water chemistry on bacterial transport during infiltration.* Journal of Contaminant Hydrology, 2013. **150**(0): p. 54-64.
61. Davidson, A., et al., *Proton magnetic resonance spectroscopy (H-1-MRS) of the brain following high-dose methotrexate treatment for childhood cancer.* Medical and Pediatric Oncology, 2000. **35**(1): p. 28-34.
62. Pinsker, M.O., et al., *Electrode implantation for deep brain stimulation in dystonia: A fast spin-echo inversion-recovery sequence technique for direct stereotactic targeting of the GPi.* Zentralblatt Fur Neurochirurgie, 2008. **69**(2): p. 71-75.
63. Wang, X.H., et al., *Evaluation of quantitative measures of breast tissue density from mammography with truth from MRI data.* Medical Imaging 2003: Image Processing, Pts 1-3, 2003. **5032**: p. 82-89.
64. Li, L.Q., H. Han, and B.J. Balcom, *Spin echo SPI methods for quantitative analysis of fluids in porous media.* Journal of Magnetic Resonance, 2009. **198**(2): p. 252-260.
65. Duh, A., et al., *The elimination of magnetic susceptibility artifacts in the micro-image of liquid-solid interfaces: internal gradient modulation by the CPMG RF train.* Journal of Magnetic Resonance, 2003. **160**(1): p. 47-51.
66. Britton, M.M., R.G. Graham, and K.J. Packer, *Relationships between flow and NMR relaxation of fluids in porous solids.* Magnetic Resonance Imaging, 2001. **19**(3-4): p. 325-331.

67. Goelman, G. and M.G. Prammer, *The Cpmg Pulse Sequence in Strong Magnetic-Field Gradients with Applications to Oil-Well Logging.* Journal of Magnetic Resonance Series A, 1995. **113**(1): p. 11-18.
68. Callaghan, P.T., *Translational dynamics and magnetic resonance : principles of pulsed gradient spin echo NMR*2011, Oxford ; New York: Oxford University Press. xvii, 547 p.
69. Callaghan, P.T., *Principles of nuclear magnetic resonance microscopy* 1991, Oxford England New York: Clarendon Press ;Oxford University Press. xvii, 492 p.

70. Freeman, R., *Magnetic resonance in chemistry and medicine* 2003, Oxford ; New York: Oxford University Press. xii, 278 p.
71. Levitt, M.H., *Spin dynamics : basics of nuclear magnetic resonance*. 2nd ed2008, Chichester, England ; Hoboken, NJ: John Wiley & Sons. xxv, 714 p., 7 p. of plates.
72. Atkins, P.W. and J. De Paula, *Atkins' Physical chemistry*. 7th ed 2002, Oxford ; New York: Oxford University Press. xxi, 1149 p.
73. Hahn, E.L., *SPIN ECHOES.* Physical Review, 1950. **80**(4): p. 580-594.
74. Carr, H.Y. and E.M. Purcell, *Effects Of Diffusion On Free Precession In Nuclear Magnetic Resonance Experiments.* Physical Review, 1954. **94**(3): p. 630-638.
75. Hennig, J., A. Nauerth, and H. Friedburg, *Rare Imaging - a Fast Imaging Method for Clinical Mr.* Magnetic Resonance in Medicine, 1986. **3**(6): p. 823-833.
76. Stejskal, E.O. and J.E. Tanner, *Spin Diffusion Measurements: Spin Echoes In The Presence Of A Time-dependent Field Gradient.* Journal of Chemical Physics, 1965. **42**(1): p. 288-+.

2 Reaction Induced Viscosity Gradients

Viscous fingers can be seen in both reactive[1-3] and non-reactive systems[4-6]. In this chapter we investigate the reactive system where two, low viscosity solutions react to form a highly viscous interface[7] with a variety of MR techniques. Podgorski *et. al* investigated the displacement of Cetyltrimethylammonium bromide (CTAB) solutions by sodium salicylate in a Hele-Shaw cell as a function of flow rate[8]. The mixing of CTAB and sodium salicylate develops a wormlike micelle layer which is highly viscous[9]. It was found that as the flow rate was increased the fingers formed became broader and slower. These findings are in contradiction with the trends found in both non-reactive [4, 5] and reactive systems[10] by previous studies. Broyles *et. al* investigated the displacement of viscous fluids through a chromatography column using optical visualization[5]. By increasing the flow rate, the pressure force within the system was increased. This resulted in the formation of narrow, fast moving fingers. This flow dependence has also been seen in reactive systems where a pre-existing viscosity gradient has been combined with a chemical reaction[10]. Nagatsu *et. al* analysed the development of fingers when glycerol was displaced by a less viscous fluid in a Hele-

Shaw cell. A reaction that resulted in the deposition of a precipitate at the interface between the two fluids was included. Even with the addition of this reactive interface the same dependence of finger formation on flow rate was seen[10]. Here we have used MRI to image, in 3-dimensions, the effect of flow rate on the development of viscous fingers when CTAB is used to drive sodium salicylate through a packed bed reactor, and also when sodium salicylate is used to drive CTAB. Several flow rates have been investigated and multiple image analysis techniques are applied to the data collected. MR imaging techniques have also been used to further understand the development of the wormlike micelle layer.

2.1 Experimental

2.1.1 Materials

A glass tube 30 cm in length with a 11 mm inner diameter were used to construct all packed bed reactors. For all flow experiments borosilicate glass beads (Sigma) of diameter 1 mm were used as the packing material. The porosity of theses packed beds was found to be ~ 0.3. The porosity was calculated by using a macro to calculate the void space, from each 3-D MR image. The packing material was rinsed with concentrated nitric acid and then distilled water to remove any paramagnetic species. All packing was dried in an oven at 80°C and then allowed to cool to room temperature before use. Cetyltrimethylammonium bromide (CTAB) (Sigma Aldrich, ≥ 98 %) and sodium salicylate (Sigma Aldrich, ≥ 99.5%) were used without further purification. Solutions of 20 - 70 mM CTAB and 20 - 100 mM NaSal were prepared using distilled water. These solutions were used for both relaxation measurements and imaging experiments. Wormlike micelle solutions were made by mixing, in equal parts, 100 mM sodium salicylate solution and 50 mM CTAB solution and stirring for 24 hrs. As CTAB crystallizes at low temperatures all experiments were run at 294.0 ± 0.3 K.

2.1.2 Packed bed reactor setup

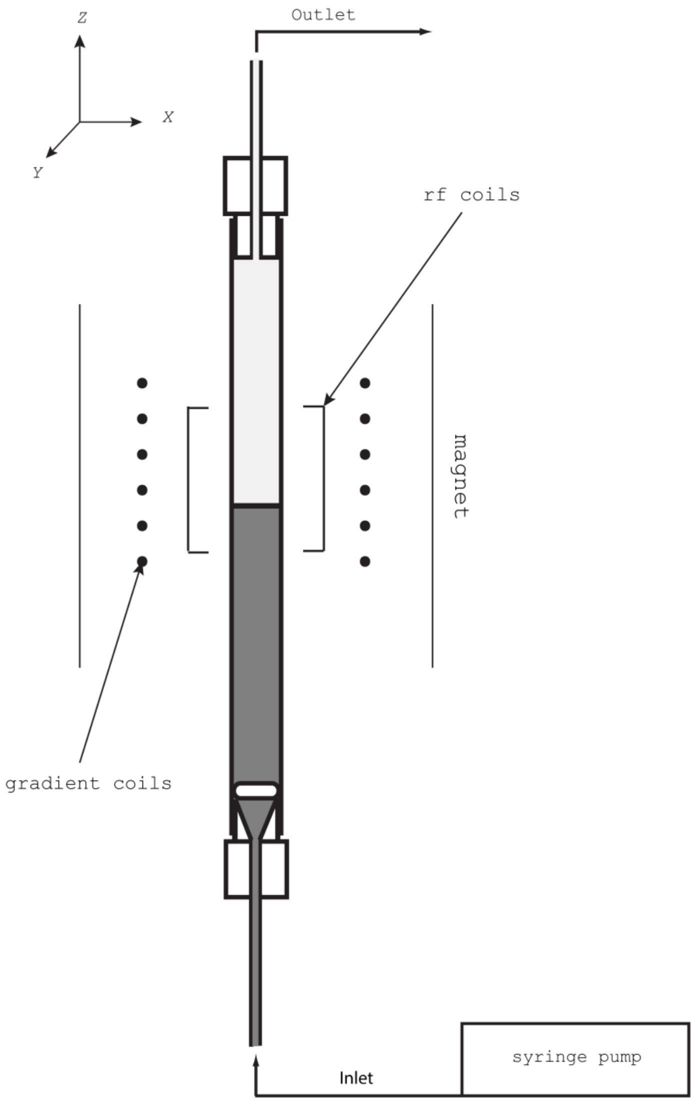

Figure 2.1: A schematic showing the experimental setup of a packed bed reactor with respect to the magnet. The arrangement of solutions is varied during the experiments. The interface between the two solutions is positioned in the bottom third of the rf coil.

Solutions of 100 mM sodium salicylate and 50 mM CTAB were used to fill a packed bed. The packed bed was held vertically in a 7T magnet. Experiments were performed when the sodium salicylate solution was positioned above the CTAB solution and the CTAB solution was pumped from below using a syringe pump (Harvard pump 22) at flow rates of 1 – 4 ml hr^{-1}. In these experiments the CTAB solution displaced sodium salicylate solution. The interface between the two solutions was positioned in the bottom third of the homogeneous region of a 25 mm birdcage radiofrequency resonator before pumping was started (Figure 2.1). Experiments were then performed where the orientation of the solutions was reversed so that the sodium salicylate solution was used to drive the CTAB solution. In these experiments the sodium salicylate solution displaced the CTAB solution.

2.1.2.1 Stationary interface set up

In order to acquire MR images of developing interfaces, stationary interfaces were constructed in a boiling tube. 50 mM CTAB solution was dropped into a boiling tube containing 100 mM sodium salicylate. In some experiments 1 mm borosilicate beads were added as a packing material.

2.1.1 Nuclear magnetic spectroscopy

All magnetic resonance (MR) experiments were acquired using a Bruker DMX 300 spectrometer, operating at a ^{1}H resonance frequency of 300.13 MHz. A 10 mm radiofrequency resonator was used for all spectroscopy experiments. Data was acquired using XWIN-NMR 2.6 software. Measurements were carried out in a 5 mm NMR tube. All samples were allowed to equilibrate to the temperature inside the magnet bore, 294.0 ± 0.3 K, for 30 minutes before any measurements were acquired. T_1 relaxation measurements were made for CTAB and sodium salicylate solutions ranging from 20 to 100 mM using inversion recovery experiments. Inversion recovery (IR) experiments were performed to measure the T_1 times for solutions, using 16 experiments with IR delays logarithmically spaced between 5 μs and 15 s. 90° and 180° r.f. pulses were 24.07 and 48.14 μs respectively at an attenuation of 10 db. A spectral width of 10 KHz was used with 2 signal averages, each acquiring 16k complex points. Carr-Purcell-Meiboom-Gill[11] (CPMG) experiments were performed to measure the T_2 for the solutions, acquiring a maximum of 512 echoes with an echo spacing of 20 ms. A spectral width of 10 KHz was used with 2 signal averages, each acquiring 16k complex points. 90° and 180° rf pulses were 24.07 and 48.14 μs respectively at an attenuation of 10 db. All T_1 and T_2 relaxation measurements were acquired through analysis carried out in Prospa NMR analysis software[12].

2.1.2 Magnetic Resonance Imaging

All magnetic resonance imaging was carried out using PARAVISION 2.1.1 software. A 25 mm radiofrequency resonator with an observable region of 2.5 cm x 4 cm was used for all imaging experiments. Three-dimensional images were acquired using the fast spin-echo imaging technique RARE[13], with a field of view of 40 mm × 20 mm × 12 mm and a pixel array of 256 (z) ×128 (x) ×16 (y), respectively. A RARE factor of 128 was used, giving an effective echo time of T_{eff} = 575 ms, resulting in high signal intensity (SI) for the water in the CTAB solution and low SI for the NaSal and micelle solutions. The spectral width was 50 KHz. The repetition time was T_R = 1 s, with a time resolution between images of 120 s unless otherwise stated. All images were analysed using prospa NMR anaylisis software.

2.1.2.1 Imaging of a stationary interface

A 25 mm radiofrequency resonator with an observable region of 2.5 cm x 4 cm was used to acquire images of the stationary interface. Two-dimensional images were acquired using the fast spin-echo imaging technique RARE[13], with a field of view of 40 mm × 20 mm and a pixel array of 256 (z) ×128 (x) respectively. A Gaussian rf pulse was used to selectively excite a slice of 1 mm in thickness. A RARE factor of 128 was used, with a T_e = 8.9 ms and T_R = 1 s. The spectral width was 50 KHz. To acquire T_2 maps of the interface a field of view of 40 x

20 mm was used with a pixel array of 128 (z) × 64 (x). The RARE factor was reduced to 64 with 8 echoes used. Pixel intensity in the T_2 maps provides a measure of T_2 relaxation for each spin packet.

The time resolution between all images was 5 minutes. All images were analysed using prospa NMR anaylisis software.

2.2 Results and discussion

Although magnetic resonance imaging does not require optical contrast for imaging purposes, MR contrast must be acquired so that the regions containing CTAB and sodium salicylate can be distinguished. Differences in relaxation times were used to attain this image contrast.

2.2.1 Relaxation measurements

Figure 2.2 shows a plot of the T_1 relaxations of the water peak of CTAB solutions of a concentration range 20 mM to 70 mM and of the water peak in sodium salicylate solutions of concentration range 20 mM to 100 mM. There is little or no concentration dependence of these relaxation times. There is no variation in T_1 relaxation time with concentration therefore T_1 cannot be used as an image contrast parameter.

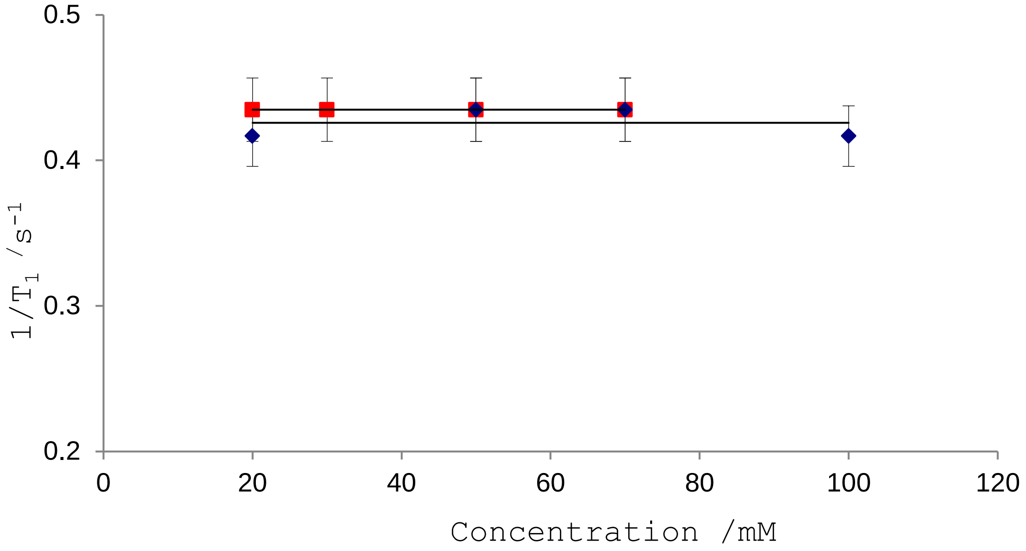

Figure 2.2: Shows a plot of $1/T_1$ relaxation rates for water in CTAB,■,20 mM to 70 mM solution, and in sodium salicylate, ◆, 20 mM to 100 mM solutions.

It can be seen, Figure 2.3, that there is no concentration dependence for the T_2 relaxation of the water peak in the CTAB solutions. However, there is concentration dependence for the T_2 of the water peak in sodium salicylate solutions.

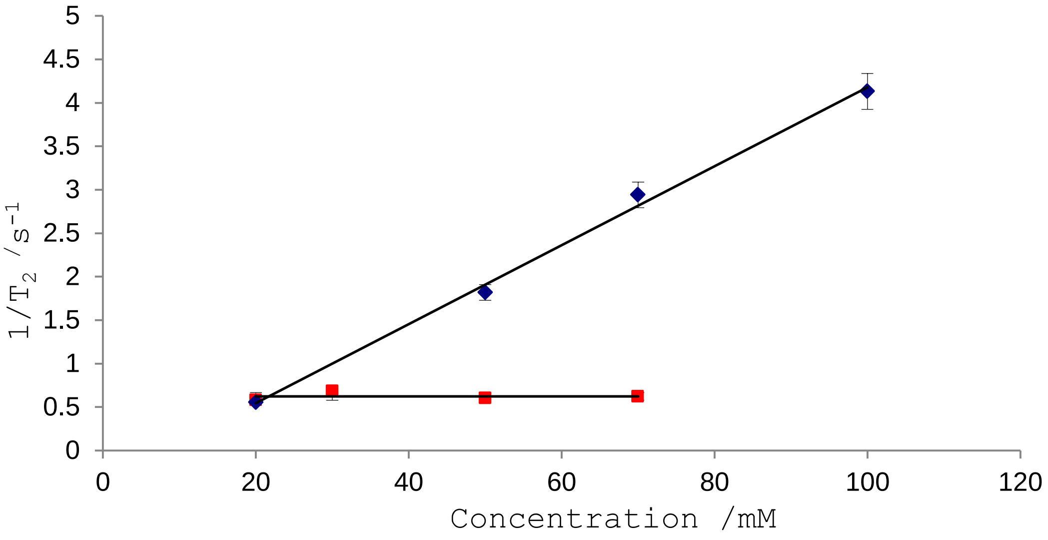

Figure 2.3: Shows a plot of $1/T_2$ relaxation rates for water in CTAB,■, 20 mM to 70 mM solution and sodium salicylate, ◆, 20 mM to 100 mM solutions.

The origin of this reduction in T_2 relaxation time as the concentration of sodium salicylate increases is expected to be due to fast-proton exchange occurring between the water and the hydroxide group of the sodium salicylate. This resonance is typically not detected in NMR spectra where water is used as the solvent. However, in deuterated dimethylsulfoxide the chemical shift for this resonance for lithium salicylate is extremely high at 15.7 ppm[14] and as it is sufficiently different from water, it is expected that proton exchange between these two resonances will reduce the T_2 relaxation time of the solvent.

To exploit this relaxation dependence to create image contrast, solutions of 50 mM CTAB with a T_1 relaxation time of 2.4 ± 0.1 s and a T_2 relaxation of 1660 ± 10 ms, and 100 mM sodium salicylate, with a T_1 relaxation time of 2.3 ± 0.1 s and a T_2 relaxation of 240 ± 8 ms, were used for all imaging experiments. A 50:50 mixture of the two solutions provided a wormlike micelle solution that could be used to indicate the relaxations of any interface that was to develop during the experiments. The T_1 and T_2 relaxation times of this solution were found to be 2.3 ± 0.1 s and 664 ± 8 ms respective.

2.2.2 Image contrast

As previously shown, the T_2 relaxation times of CTAB and sodium salicylate vary providing a possible route for image contrast. To test the image contrast between the solutions, a RARE horizontal 2-dimensional image of a phantom that had been constructed from three 5 mm NMR tubes, each containing one of the three experiment solutions was acquired. In a T_2 weighted image the spins with shorter T_2 relaxation times have low signal intensity and those with longer T_2 relaxation times have high signal intensity.

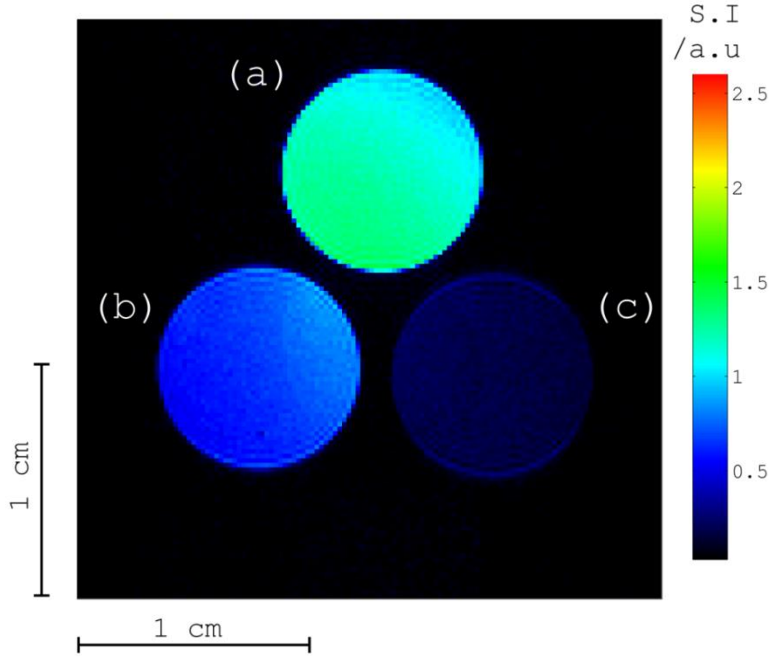

Figure 2.4: A 2-dimensional, horizontal, RARE MR image showing three 5 mm nmr tubes containing 50 mM CTAB,(a), 100 mM sodium salicylate,(c) and wormlike micelles, (b). FOV was 2 x 2 cm with a pixel array of 128 x 128. A RARE factor of 128 was used.

In Figure 2.4 a horizontal two-dimensional RARE image of 5 mm nmr tubes containing 50 mM CTAB, (a), 100 mM sodium salicylate, (c), and a solution of wormlike micelles equal parts a and c, (b). By Using a RARE factor of 128 the three solutions can be distinguished. Water in the sodium salicylate solution has low signal intensity while the water in the CTAB solution has high signal intensity. The signal intensity for the water in the wormlike micelle solution lies between. As well as providing image contrast for the investigation of finger development the T_2 dependence of these solutions also provides a means to monitor a developing micelle interface

2.2.3 Development of interface over time

Previous studies have questioned how the development of the wormlike micelle interface over the period of an imaging experiment affects the formation of fingers[3, 8]. Wormlike micelle interfaces were setup and different imaging techniques were used to understand how the interface develops over time. Figure 2.5 shows a series of time lapse images for the development of a wormlike micelle interface.

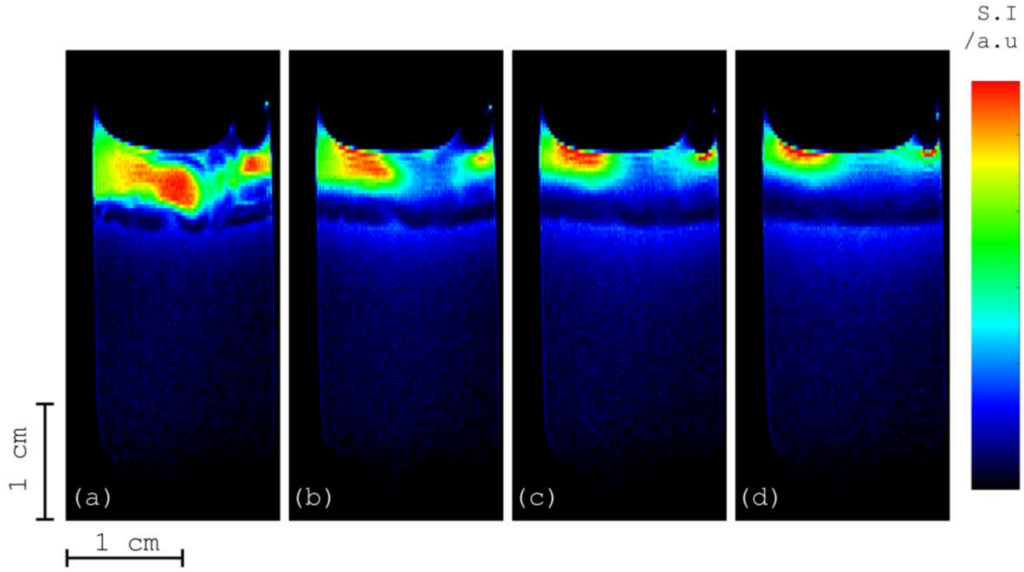

Figure 2.5: A time lapse series of RARE MR images showing the development of a wormlike micelle interface between a solution of 50 mM CTAB, high signal intensity, and 100 mM sodium salicylate, low signal. FOV was 4 x 2 cm with a pixel array of 256 x 128. A RARE factor of 128 was used. Images are shown at 10 minute intervals.

In Figure 2.5(a) 50 mM CTAB solution, high signal, is seen to form a layer at the top of the image. The low signal region below this layer is 100 mM sodium salicylate. When comparing Figure 2.5 (a) and Figure 2.5 (d) the regions directly above and below the initial interface show changes in signal intensity. The area where CTAB, high signal intensity, was seen just above the original interface now has slightly reduced in signal intensity. The reverse is seen just below the interface, where the signal intensity has increased slightly. These changes in signal intensities indicates differences in the T_2 relaxations of the solutions, and are due to the diffusion of CTAB and sodium salicylate resulting in the broadening of the wormlike micelle interface. This diffusion continues throughout the times series, with the regions of CTAB and sodium salicylate decreasing in volume and the interface developing out from its original position.

The experiment was repeated and Figure 2.6 shows a series of time lapse images for the development of a wormlike micelle interface with the addition of 1 mm borosilicate glass beads.

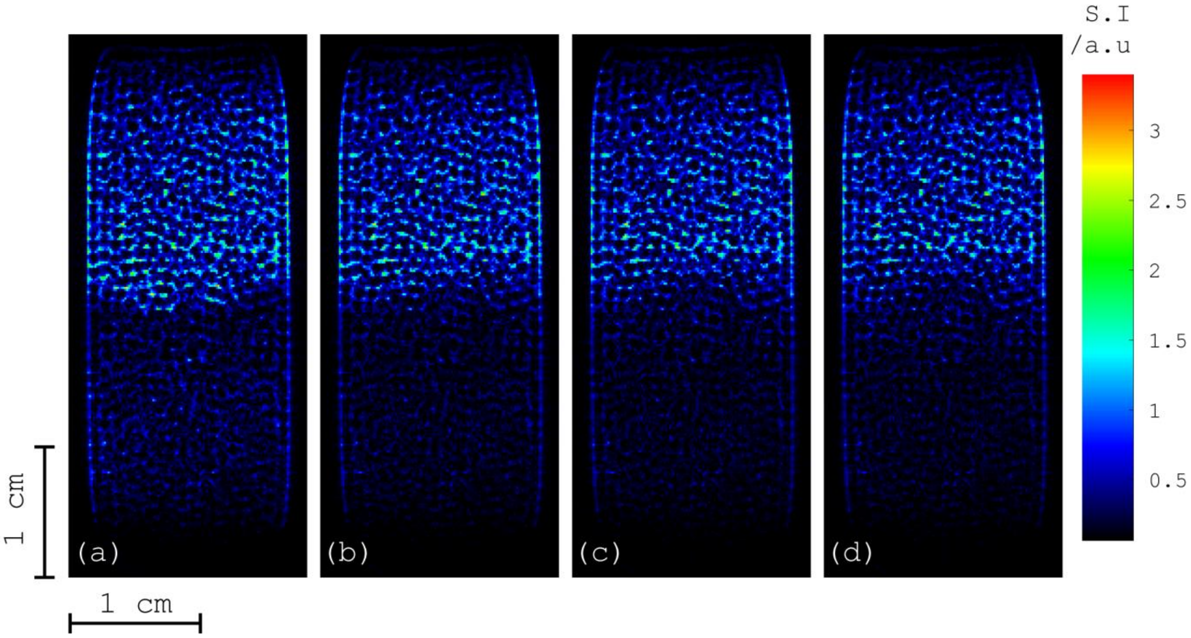

Figure 2.6: A time lapse series of RARE MR images showing the development of a wormlike micelle interface between a solution of 50 mM CTAB, high signal intensity, and 100 mM sodium salicylate, low signal with 1 mm borosilicate glass beads as a packing material. The Field of view was 4 x 2 cm with a pixel array of 256 x 128. A RARE factor of 128 was used. Images are shown at 10 minute intervals.

In Figure 2.6 (a) CTAB, high signal intensity, is seen in the top half of the image and sodium salicylate, low signal intensity, in the bottom half of the image. While these two solutions are still distinguishable with the addition of packing material, the signal from the wormlike micelle layer is no longer obvious. In Figure 2.6 (b) the region of the packed bed occupied by CTAB reduces slightly, retreating away from the initial interface position. This behaviour is most obvious when comparing Figure 2.6 (a) and (d). This can be attributed to the development of the wormlike micelle layer. However, being unable to identify the wormlike micelle layer directly, it cannot be assumed that the same behaviour is not occurring below the initial interface in the sodium salicylate region.

While it has been confirmed that the wormlike micelle layer develops and expands over time, without specific T_2 measurements it can be difficult to identify the separate components of the system.

To learn more about the developing interface the experiment was repeated, without the presence of packing, but this time T_2 maps were acquired every 10 minutes. Each pixel in the images now provides a T_2 relaxation time rather than signal intensity.

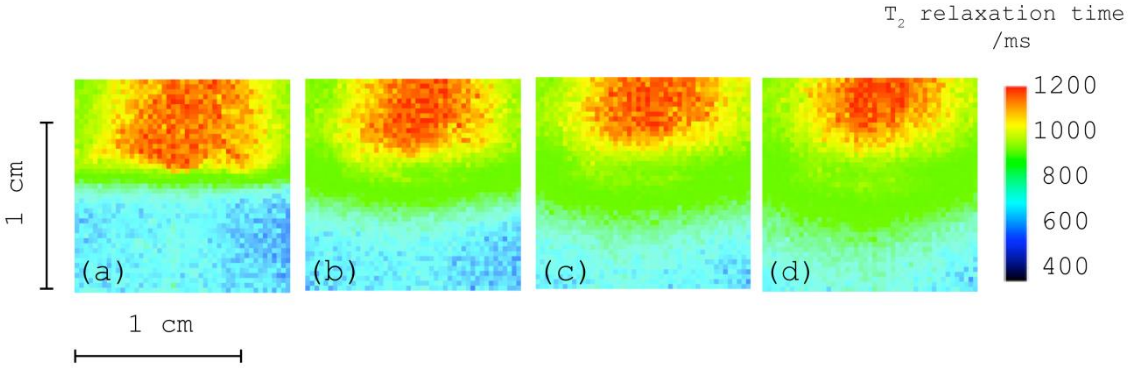

Figure 2.7: A time lapse series of T_2 maps showing the development of a wormlike micelle interface between a solution of 50 mM CTAB, and 100 mM sodium salicylate. The field of view is 4 x 2 cm with a pixel array of 128 x 64. A RARE factor of 64 was used and 8 echoes acquired. Only the section of the T_2 maps containing the interface is shown. Images are shown at 10 minute intervals.

In Figure 2.7(a) the CTAB solution (red) is seen in the top half of the image, T_2 ~1.2 s, while sodium salicylate solution (dark blue) is seen in the bottom half of the image, T_2 ~ 0.5 s. However there are several regions that have T_2 values lying between the maximum and minimum T_2 of the initial reactants. The areas in images (a) through to (d) that have a T_2 ~ 0.8 s indicate the formation of the wormlike micelle layer (green). In Figure 2.7 (a) this region forms uniformly between the two reactants, but also up the sides of the area containing CTAB. These additional regions of wormlike micelles are formed during the process of adding the CTAB to the tube. Around all regions of CTAB a fluid with a T_2 ~ 1 s is seen (yellow) and in parallel to this around all regions of sodium salicylate a fluid with a T_2 ~ 0.7 s is seen (light blue). In Figure 2.7 (b) both of these regions are seen to have migrated towards their respective reactant with the growth of the micelle layer. These regions indicate the initial stages of wormlike micelle development where either reactant is still the main component and dominates the T_2. In Figure 2.7 (c) and (d) the wormlike micelle layer continues to expand in width, while the volume of the reactants decreases. As expanding wormlike micelle layers grows outwards from its original position, it encroaches on the areas previously occupied by both CTAB and sodium salicylate, showing no dominance of diffusion in either direction.

In Figure 2.8 a plot of the T_2 relaxation times against position across the interface is shown. By taking a single, vertical profile through each image the change in relaxations over time can be seen.

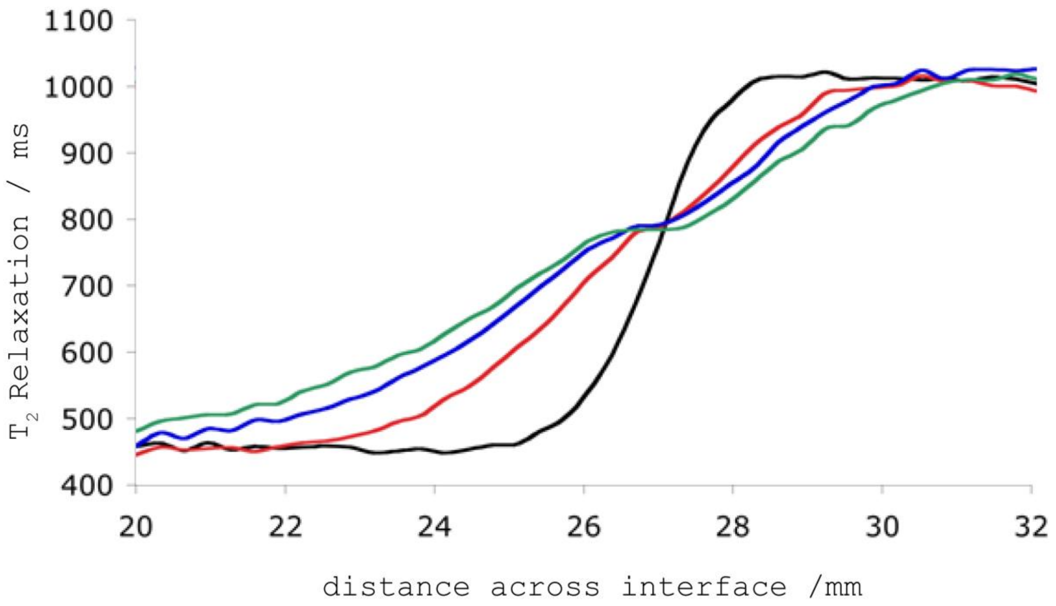

Figure 2.8: A plot of T_2 relaxation times against distance from profiles taken from T_2 maps of an interface between 50 mM CTAB and 100mM sodium salicylate, where *t* = 0 min (black), *t* = 10 min (red), *t* = 20 min (blue)and *t* = 30 min (green).

At *t* = 0, the black line, the CTAB solution is positioned above 28 mm and the sodium salicylate is positioned below 25 mm. There is initially a steep transition between these regions, indicating a high concentration gradient. Fick's first law of diffusion, eq 2.1, where J is the flux of matter, D is the diffusion co-efficient, dN is the change in number density of the particles and dz the distance, shows that the rate of diffusion is dependent on the concentration gradient between two points.

$$J = -D\frac{dN}{dz} \qquad 2.1$$

The red line corresponds to the profile through Figure 2.7 (b). There is a significant difference in the slope of this profile and the previous. Initially the concentration gradient at the interface was high, leading to quick diffusion of CTAB and sodium salicylate across the wormlike micelle layer, and so the expansion of the wormlike micelle interface and the reduction of T_2 relaxations in the centre of the image. As the interface develops over time the concentration gradient decreases, the rate of diffusion of reactants falls and so the rate of formation for the wormlike micelle slows. This shows that when carrying out viscous fingering experiments the initial formation of the wormlike micelle interface occurs on contact between CTAB and sodium salicylate, and continues to develop over the period of the experiment. Without the presence of the reaction it would be expected that the rate of diffusion would gradually decrease as the reactants are consumed and the concentration differences decrease. In figure 2.8 it is clear that while the rate of diffusion does decrease as time progresses there is deviation around the central region of the plot from the expected concentration profile. This is due to the development of the wormlike micelle layer between the two original reactants. As the wormlike micelle layer expands, as seen in figure 2.7, a plateau develops in the concentration profile observed. This enables us to see the growth of the wormlike micelle layer, which continues over the period of 30 minutes. From figure 2.8 we are able to see that the wormlike micelle layer is continuously developing through the period of a flow experiment, due to the application of flow but also the diffusion of reactants.

2.2.4 Three dimensional imaging

Measurements showing the variation of T_2 relaxation times demonstrates how MRI can identify the two constituent solutions and in doing so can follow the development of the interface between solutions during flow in a porous media. Unlike previous measurements of viscous fingering carried out in a packed bed reactor[4, 16], no contrast agent needs to be added. While T_2 maps provided precise T_2 relaxation information about the developing system, they are also very time consuming experiments to run and so T_2 weighted, RARE imaging sequence was used. While in a Hele-Shaw cell flow only occurs in a single plane, we cannot make such assumptions for a three dimensional porous media. In order to understand three-dimensional viscous fingering, three dimensional imaging is required. As the additional dimension of the image is acquired via the addition of a second phase gradient there is a significant effect on image acquisition time. Although it took 32 seconds for the three dimensional images to be acquired, the additional information enabled an increased ability to capture instabilities forming but also provide detailed images of the flow in three dimensions.

2.2.4.1 Displacement of CTAB solution through a packed bed by sodium salicylate

The packed bed reactor is filled with a 50 mM CTAB solution, a high signal fluid, and displaced by a 100 mM sodium salicylate solution, a low signal fluid. Flow rates of 1, 2, 3, and 4 ml/hr were investigated with a time series of 3-dimensional MR RARE images acquired for each flow rate. Multiple experiments were carried out for each flow rate. Here we present a representative experiment for each flow rate.

In Figure 2.9 a time series of MR images is shown for the displacement of CTAB by sodium salicylate at 1 ml/hr. In Figure 2.9 (a) the packed bed is filled with the CTAB solution, high signal, and the initial development of a finger is seen at the bottom of the left hand side of the packed bed, indicated by a low signal region.

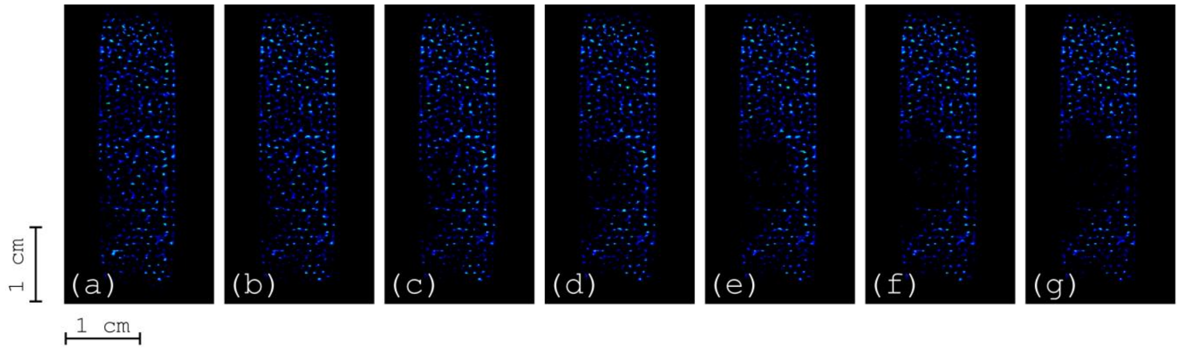

Figure 2.9: A time series of MRI images showing the displacement of 50 mM CTAB solution, through a packed bed by 100 mM sodium salicylate solution at a flow rate of 1 ml/hr. The field of view is 4 cm x 2 cm x 1.2 cm and a pixel array of 256 x 128 x 16 px, with a RARE factor of 128. A vertical cross section of each 3-D image is shown. Images are shown at 2 minute intervals.

In Figure 2.9 (b) the finger on the left hand side has only slightly increased in length, and little change has been seen from the origin image. In Figure 2.9 (c) the finger has begun to spread towards the center of the image. It is not until Figure 2.9 (d) that the structure of the finger becomes clear. The finger has developed along the left hand side of the packed bed reactor and half way along the image begun to spread at the tip. In Figure 2.9 (e to g) the finger continues to increase in width, finally reaching the right hand side of the packed bed.

In Figure 2.10 a time series of MR images is shown for the displacement of CTAB, this time with a flow rate of 2 ml/hr.

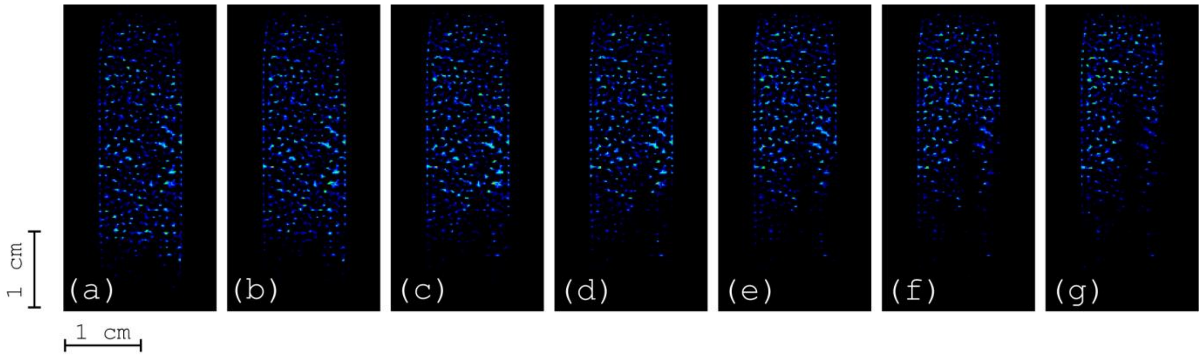

Figure 2.10: A time series of MRI images showing the displacement of 50 mM CTAB solution, through a packed bed by 100 mM sodium salicylate solution at a flow rate of 2 ml/hr. The field of view is 4 cm x 2 cm x 1.2 cm and a pixel array of 256 x 128 x 16 px, with a RARE factor of 128. A vertical cross section of each 3-D image is shown. Images are shown at 2 minute intervals.

In Figure 2.10 (a) the interface between the CTAB and the sodium salicylate is seen at the bottom of the image. While the interface is not perfectly horizontal, no instability development is seen. The case is the same for image (b). In Figure 2.10 (c), however, the onset of an instability is seen slightly to the right of the center of the image. The main interface has also shifted up though the packed bed. The finger becomes more defined in image (d) where a narrow finger can be seen to accelerate through the packed bed. The finger is well defined in images (f and g) and has moved ahead of the bulk interface, which is also moving upwards through the packed bed.

In both the 1 ml/hr and the 2 ml/hr experiments finger formation has been seen. The finger formed in the 2 ml/hr experiment is narrow and fast moving as would be expected in this system at low flow rates. In the case of 1 ml/hr the finger accelerates further ahead of the bulk interface than the finger in the 2 ml/hr experiment, but shows a greater degree of spreading and therefore a broader finger. If slower flow rates were indicative of narrower, faster moving fingers then it would be expected that the 1 ml/hr experiment would produce narrower fingers than the experiment run at 2 ml/hr. The fact that this is not the case can be explained in terms of interface development. The finger does not appear to broaden by a great amount in the first 4 images of Figure 2.9, but then quickly spreads across the width of the packed bed. At lower flow rates the wormlike micelle layer is displaced at a slower rate. As was demonstrated earlier in this chapter, the wormlike micelle layer thickens over time. The longer it has to develop, the thicker it becomes and therefore it can provide greater resistance to flow. The pressure however builds up behind this ‘thick’ interface and eventually any weakness is exploited and the displacing fluid breaks through. This behavior was seen in previous studies carried out in Hele-Shaw cells[8].

By increasing the flow rate to 3 ml/hr we are able to identify possible dependence of finger formation on flow rate. In Figure 2.11 the MR image sequence is shown for a flow rate of 3 ml/hr.

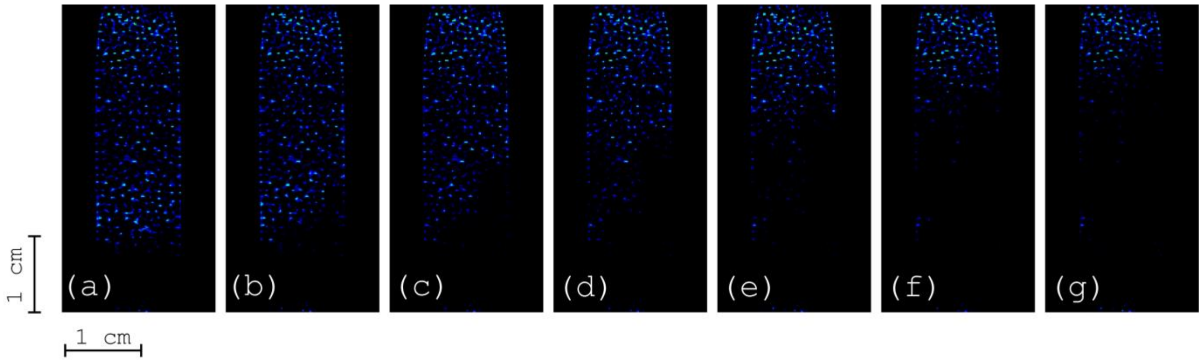

Figure 2.11: A time series of MRI images showing the displacement of 50 mM CTAB solution, through a packed bed by 100 mM sodium salicylate solution at a flow rate of 3 ml/hr. The field of view is 4 cm x 2 cm x 1.2 cm and a pixel array of 256 x 128 x 16 px, with a RARE factor of 128. A vertical cross section of each 3-D image is shown. Images are shown at 2 minute intervals.

In Figure 2.11 (a) a horizontal interface between the CTAB and the sodium salicylate solutions, with no perturbations, is seen at the bottom of the image. In image (b) the interface is shifted upwards on the right hand side of the image as a finger is formed. Figure 2.11 (c) shows the forward motion of this broad finger through the packed bed. In Figure 2.11 (d) the finger can be seen to spread across the width of the packed bed, and by image (e) the lower two thirds of the image are occupied by the finger. Increasing the flow rate clearly affects the formation of viscous fingers in the packed bed, with the fingers formed broad and moving through the packed bed only slightly ahead of the bulk flow.

A final flow rate of 4 ml/hr was studied to analysis the effect of flow rate. In Figure 2.12 the MR image sequence is shown for a flow rate of 4 ml/hr.

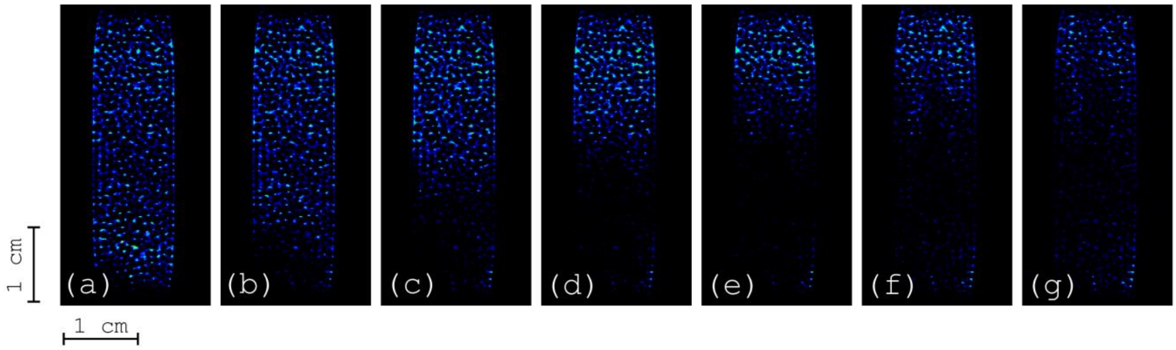

Figure 2.12: A time series of MRI images showing the displacement of 50 mM CTAB solution, through a packed bed by 100 mM sodium salicylate solution at a flow rate of 4 ml/hr. The field of view is 4 cm x 2 cm x 1.2 cm and a pixel array of 256 x 128 x 16 px, with a RARE factor of 128. A vertical cross section of each 3-D image is shown. Images are shown at 2 minute intervals.

In Figure 2.12 (a) the interface can be seen at the very bottom of the image. By Figure 2.12 (b) a broad finger has formed in the bottom left corner of the image. This finger quickly spreads across the width of the packed bed as well as moving upwards, as seen in image (c). The flow at 4 ml/hr is more indicative of the movement of the interface through the packed bed rather than the spread of a broad finger.

The higher flow rates of 3 and 4 ml/hr have shown to produce broad fingers that quickly spread across the packed bed. Again this behaviour can be explained in terms of interface development. At lower flow rates the interface was developed enough to restrict the flow and encourage finger formation. With higher flow rates the reverse is true. The fast moving systems now prevent the wormlike micelle layer from fully developing, therefore removing any resistance against the flow.

The behaviour seen in these results, the broadening of fingers with increased flow rates, aggress with the trends seen by Podgorski *et. al*[8]. While spreading has been seen across all the flow rates, albeit due to different mechanisms, neither the splitting of fingers or the shielding of secondary instabilities has been seen. In the study by Podgorski *et. al* it was shown that reversing the arrangement of fluids can affect finger development. Fingers that developed when CTAB displayed sodium salicylate developed later, and were broader than those with the opposite chemical arrangement. This behaviour was only presented for one flow rate. To see if this behaviour is also present in the 3-dimensional system and to evaluate the effect of flow rate, the arrangement of the reactants was reversed and the flow experiments repeated.

2.2.4.2 Displacement of sodium salicylate solution through a packed bed by CTAB

The displacement of sodium salicylate, low signal, by CTAB, high signal fluid, under flow was imaged every two minutes. For each three-dimensional image a vertical plane can be selected to display a vertical cross sectional view of the system.

In Figure 2.13 a time series of images is shown for the flow of CTAB, high signal, though a packed bed filled with sodium salicylate, low signal, at a flow rate of 1 ml/hr.

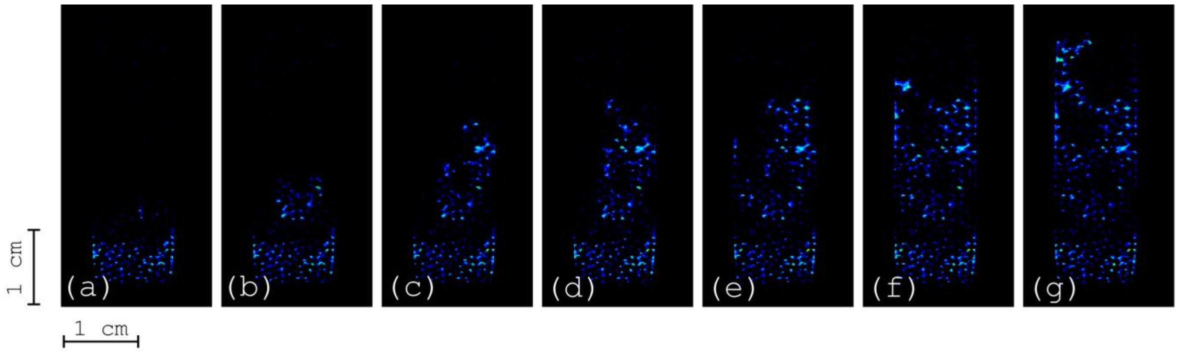

Figure 2.13: A time series of MRI images showing the displacement of 100 mM sodium salicylate solution through a packed bed by 50 mM CTAB solution, at a flow rate of 1 ml/hr. The field of view is 4 cm x 2 cm x 1.2 cm and a pixel array of 256 x 128 x 16 px, with a RARE factor of 128. A vertical cross section of each 3-D image is shown. Images are shown at 2 minute intervals.

Initially in Figure 2.13 (a) the interface between the two fluids is seen in the lower region of the image. Slightly above the interface there is a region of low signal and then a very small area of high signal, that appears to be detached from the bulk of the CTAB solution. In image (b) this ‘detached’ region grows in size and in image (c) develops into a finger that moves up through the packed bed. The finger broadens, and in image (d) a small, narrow finger develops from the tip of the main finger. In image (e) a second finger develops on the left hand side of the packed bed and moves along the packed bed wall eventually meeting with the original finger (image (f)). In the final image of the time series (image (g)), the finger to the left of the packed bed continues to move forward and curves back towards the center of the packed bed before moving out of the observable region of the r.f. coil.

It is clear from the disjoined occurrences of high signal pixels in the images and the patches of disconnected low signal areas that shows a single plane from a 3-dimensional image does not show the full development of the fingers. This is due to their tortuous path through the packed bed. This particular problem will be addressed in the image analysis section of this chapter. Although there is some detail missing there are still several new features seen in these images. Two separate fingers were seen to move through the packed bed, with one taking a tortuous path across the width of the packed bed, within the plane of the image shown. The initial finger is broad but then splitting is seen and over the course of the experiment two fingers are seen to split from the main finger.

When increasing the flow rate to 2 ml/hr, finger development is still clearly seen in time series of vertical images shown in Figure 2.14.

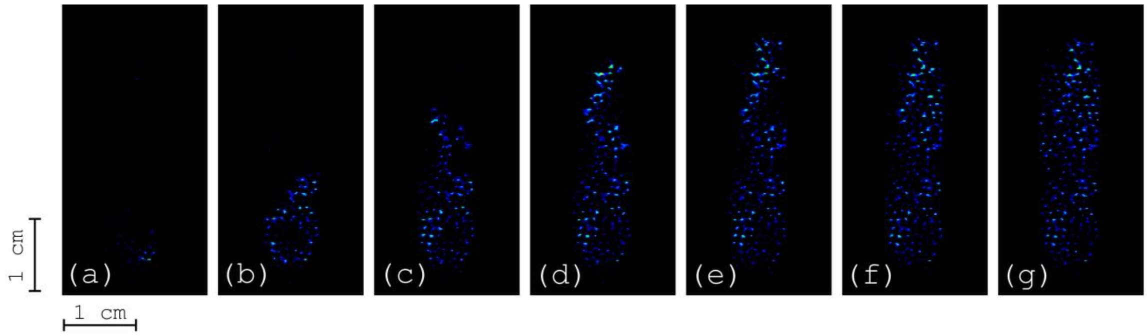

Figure 2.14: A time series of MRI images showing the displacement of 100 mM sodium salicylate solution through a packed bed by 50 mM CTAB solution, at a flow rate of 2 ml/hr. The field of view is 4 cm x 2 cm x 1.2 cm and a pixel array of 256 x 128 x 16 px, with a RARE factor of 128. A vertical cross section of each 3-D image is shown. Images are shown at 2 minute intervals.

In Figure 2.14 (a) the interface between the two fluids is positioned just below the observable region of the coil, but the very tip of an instability can be seen at the lower edge of the image. In Figure 2.14 (b) a finger moves up through the centre of the image. Its width is comparable to that of the main finger seen in Figure 2.13. In Figure 2.14(c) the narrow, central finger accelerates through the packed bed. In image (d) the finger moves further through the packed bed and, while it is not a perfectly straight finger, it also does not follow the tortuous path seen at 1 ml/hr. In image (e) the finger reaches the top edge of the observable region of the coil. The finger is broader at the base than at the tip showing the onset of spreading. In images (f) the finger broadens and by image (g) has spread to occupy the width of the packed bed.

Both 1 ml/hr and 2 ml/hr experiments show the formation of instabilities. At each flow rate one main finger develops through the packed bed and in the case of 1 ml/hr finger splitting and spreading is seen. This splitting behaviour was previously unseen when the arrangement of chemicals was reversed. The finger formed at 2 ml/hr appeared less tortuous in its path through the packed bed and no secondary instability or tip splitting was witnessed.

By increasing the flow rate to 3 ml/hr it is possible to further understand the effect of flow rate on finger development. In Figure 2.15 a time series of MR images show the effect of a flow rate of 3 ml/hr on the displacement of sodium salicylate by CTAB.

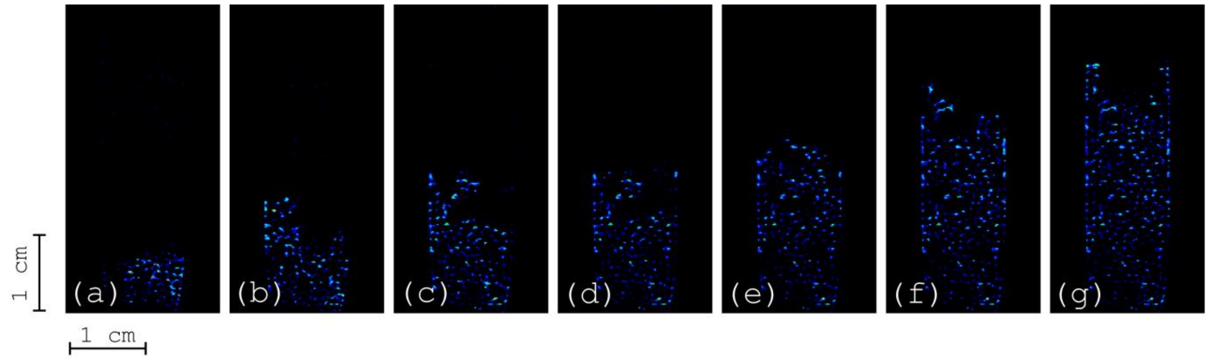

Figure 2.15: A time series of MRI images showing the displacement of 100 mM sodium salicylate solution through a packed bed by 50 mM CTAB solution, at a flow rate of 3 ml/hr. The field of view is 4 cm x 2 cm x 1.2 cm and a pixel array of 256 x 128 x 16 px, with a RARE factor of 128. A vertical cross section of each 3-D image is shown. Images are shown at 1 minute intervals.

In Figure 2.15 (a) the interface between the two solutions is seen at the lower edge of the image. It appears to be slightly uneven with the right hand side being slightly forward compared to the left. In image (b) however it is the left hand side where a finger develops. The finger moves up along the left wall of the packed bed and then in image (c) splits with one finger staying in the same path and the second curving to the right. In image (d) the distribution of CTAB through the packed bed has become more uniform, with the fingers previously seen spreading and the bulk flow from below catching up with any instabilities. Image (e) shows a uniform interface has formed between the two reactant solutions about half way up the packed bed. This stable interface is however short lived with a finger developing along the left hand wall of the packed bed (image (f) and (g)). The instabilities that form do not appear to be broader than those formed at lower flow rates, as was seen when the setup was reversed, however fingers that do form are short lived and do not move very far ahead of the main interface. Any instability formed is quickly over taken by the interface and unable to develop further.

In Figure 2.16 a time series of MR images is shown for the experiment repeated with a flow rate of 4 ml/hr.

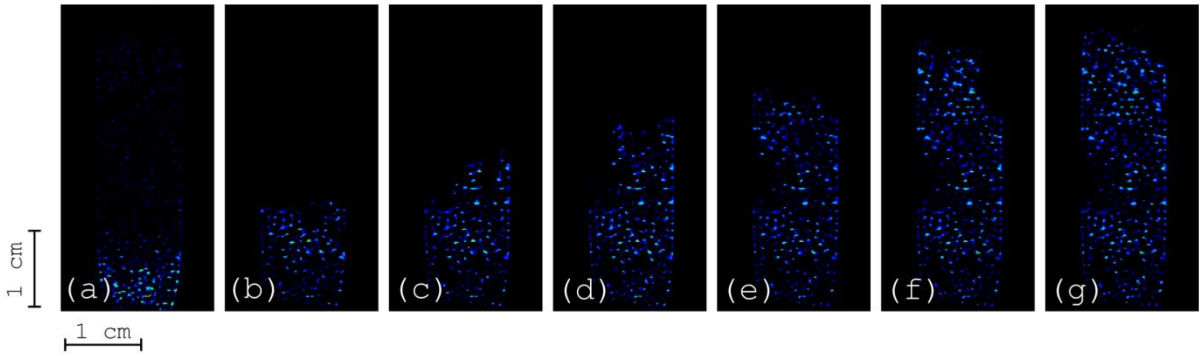

Figure 2.16: A time series of MRI images showing the displacement of 100 mM sodium salicylate solution through a packed bed by 50 mM CTAB solution, at a flow rate of 4 ml/hr. The field of view is 4 cm x 2 cm x 1.2 cm and a pixel array of 256 x 128 x 16 px, with a RARE factor of 128. A vertical cross section of each 3-D image is shown. Images are shown at 1 minute intervals.

In image (a) the interface is seen at the bottom of the image. In image (b) the interface moves up through the packed bed with a small instability starting to develop on the right hand side of the image. In images (c) and

(d) this instability is seen to move ahead of the main interface but also to broaden to over half the width of the packed bed. In image (e) the instability has occupied the full width of the packed bed while a small region of sodium salicylate, of low signal, is left behind as the finger passes. In image (f) the flow is directed through a broad finger on the left of the image that quickly spreads across the whole packed bed.

For both arrangements of chemicals one trend is seen. As the flow rate increases the fingers which formed broaden and do not accelerate ahead of the main interface to any great extent. When sodium salicylate is displaced by CTAB the fingers that form take a more tortuous path through the packed bed than fingers that develop as CTAB is displayed by sodium salicylate. There is also a great degree of finger splitting seen when CTAB is the driving fluid. Although we do see differences in the finger formation dependent on which solution displaces which, our findings do not completely agree with those of Podgorski *et. al*. In this previous study[8] it was found that when CTAB was the driving fluid, broader and later-occurring fingers were seen. Here we have observed no change in the time of finger development but we have seen a difference in the type of fingers formed. When CTAB displaces sodium salicylate, the fingers are no broader than those produced from reversing the chemical arrangement. At the higher flow rates, however, the displacement of sodium salicylate shows the formation of fingers that, while broad, are not as broad as those seen when CTAB is displaced. With the higher flow rates when CTAB is displaced, the behavior more closely associates to plug flow than finger formation. This variation in finger formation between the previous study and our own could be attributed to our use of a non-stoichiometric ratio of reactants, although further investigation would be required to confirm this.

The use of vertical slices to display the behavior within the packed bed is representative when discussing the displacement of CTAB by sodium salicylate. This is because the fingers do not take a tortuous path across the packed bed. Therefore, accurate selection of the vertical slice displayed provides an accurate representation of finger formation. This is not the case when considering the displacement of sodium salicylate by CTAB. The fingers formed in these experiments take more tortuous paths, and the occurrence of finger splitting means that displaying only vertical slices can provide all the information required to analyse finger formation in this system. For this reason, we apply two further analysis techniques to the images acquired of the displacement of sodium salicylate by CTAB.

2.3 Image analyisis

As described in the introduction to this thesis, viscous finger formation and development can be difficult to analyse. To fully display the data from all of the 3-dimensional images acquired as vertical slices would require more space than is available in this thesis. For that reason several analysis techniques have been applied to the 3-dimensionla images. Here we display the results of such analysis for the images previously presented for the displacement of CTAB of sodium salicylate and the displacement of sodium salicylate by CTAB.

2.3.1 Image compression

All MR data was analysed using Prospa NMR analysis software[17]. To complement the vertical images displayed for each flow rate, horizontal images constructed from each 3-dimensional image are shown.

To improve the signal-to-noise ratio in the pixel array along the z axis, images were Fourier transformed and compressed from 256 pixels to 32, so that each pixel along the z axis was integrated over 8 pixels. This increases the signal-to-noise ratio allowing horizontal slices from each 3-D image to be displayed.

2.3.2 Displacement of CTAB solution through a packed bed by a solution of sodium salicylate

In Figure 2.17 a time series of horizontal slices shows the displacement of CTAB by sodium salicylate at 1 ml/hr. In column (a) the packed bed is filled with CTAB solution and in the lower 3 images there is a dark region attributed to the sodium salicylate moving through the packed bed. In column (b) on the left hand side of the lower images the onset of an instability is seen to develop. In columns (c) and (d) this instability initially grows in length and then spreads slightly in width. In column (e) the instability begins to spread quickly across the width of the packed bed without much growth in length. This behavior continues in columns (f) and (g) with the instability finally reaching the full width of the packed bed.

These horizontal plots agree with the instability development which is present in the vertical plots, showing that the finger does initially grow slowly and then quickly spread as the interface breaks under the pressure of the flow.

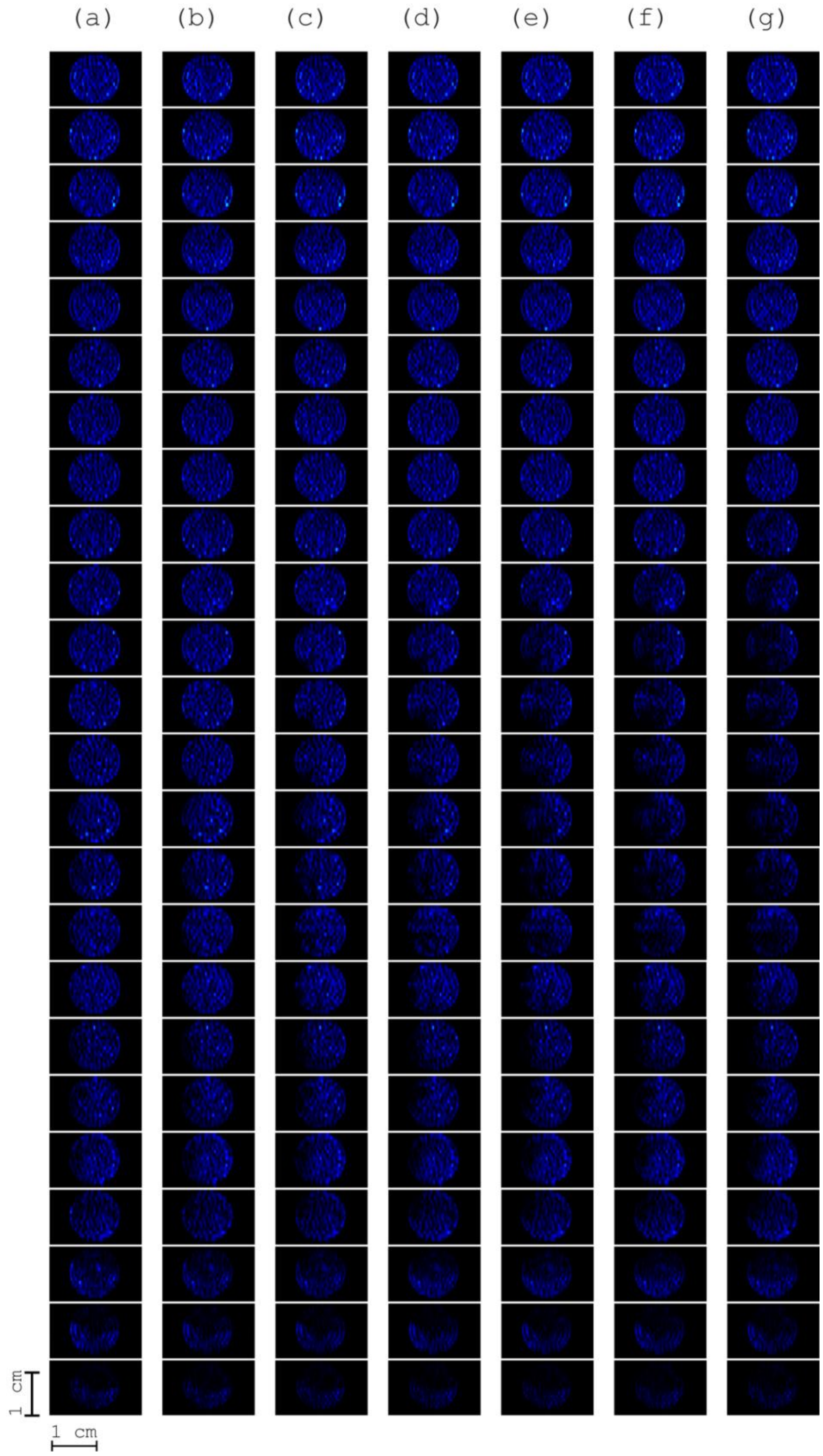

Figure 2.17: A time series of MRI images showing the displacement of 50 mM CTAB solution through a packed bed by 100 mM sodium salicylate solution, at a flow rate of 1 ml/hr. A pixel array of 256 x 128 x 16, has been compressed to 32 x 128 x 16 with the 32 horizontal images for each image being displayed here at 2 minute intervals.

In Figure 2.18 a time series of images for the experiment repeated at 2 ml/hr is shown. In the vertical images shown for this experiment, a single, narrow faster moving finger was seen to develop. The same is seen in the horizontal images shown here. In column (a) the interface between the two solutions is seen in the bottom image. Over the course of this experiment this interface moves progressively up through the packed bed. In Image (c) an instability moves slightly ahead of the main interface, positioned slightly right of centre in the packed bed. This instability continues to move further ahead of the main interface, spreading in width as it progresses. There is no evidence of a secondary finger forming and therefore no splitting or shielding occurring in the system. Again these horizontal images confirm the behaviour seen in the vertical images.

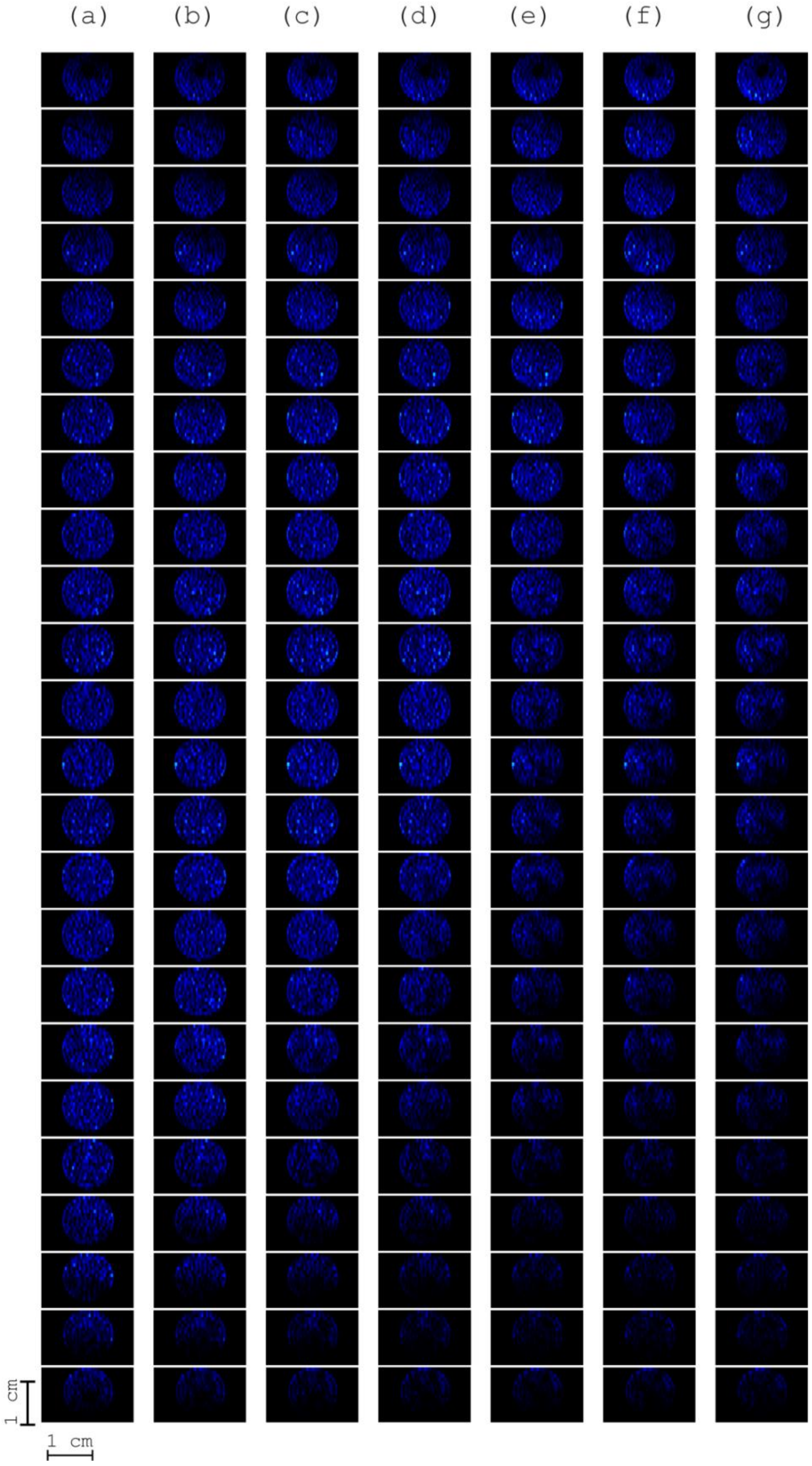

Figure 2.18: A time series of MRI images showing the displacement of 50 mM CTAB solution through a packed bed by 100 mM sodium salicylate solution, at a flow rate of 2 ml/hr. A pixel array of 256 x 128 x 16, has been compressed to 32 x 128 x 16 with the 32 horizontal images for each image being displayed here at 2 minute intervals.

In Figure 2.19 a time series is shown for the displacement of CTAB by sodium salicylate at 3 ml/hr. In columns (b) and (c) there is an instability formed on the right hand side of the packed bed. This finger is broad and slowly spreads further across the width of the packed bed. In image (d) the main interface moves forward but does not completely engulf the broad finger with continues to grow ahead of the main interface for the remaining images.

These horizontal plots show no real deviation in the development and growth of fingers than is shown in the vertical plots. As the flow rates have been increased the fingers have become broader and do not move ahead of the main interface as much as at lower flow rates. This again agrees with the behaviour seen in the vertical plots previously shown.

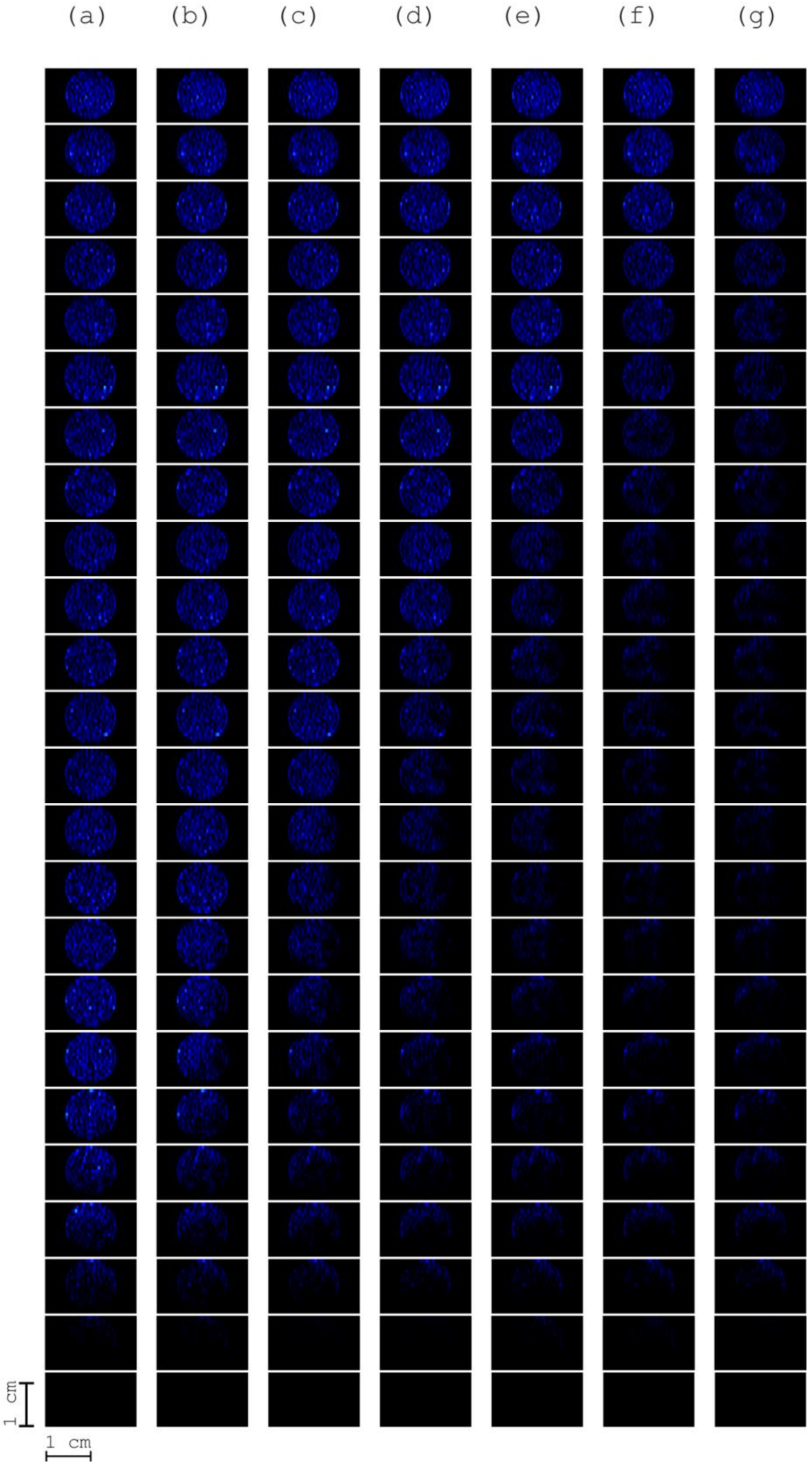

Figure 2.19: A time series of MRI images showing the displacement of 50 mM CTAB solution through a packed bed by 100 mM sodium salicylate solution, at a flow rate of 3 ml/hr. A pixel array of 256 x 128 x 16, has been compressed to 32 x 128 x 16 with the 32 horizontal images for each image being displayed here at 2 minute intervals.

In Figure 2.20 images for the final flow rate, 4 ml/hr are shown. Initially, in column (b), a finger can be seen to develop through the middle of the packed bed. However this is short lived as the main interface moves forward and engulfs the instability. This continues through the time series. In columns (f) and (g) a second instability develops but it is broad and is short lived ahead of the main interface. The flow at this flow rate is much more indicative of plug flow, as would be expected by a higher flow rate. This wormlike micelle layer now has insufficient time to develop to a thickness that will withstand and therefore restrict the flow.

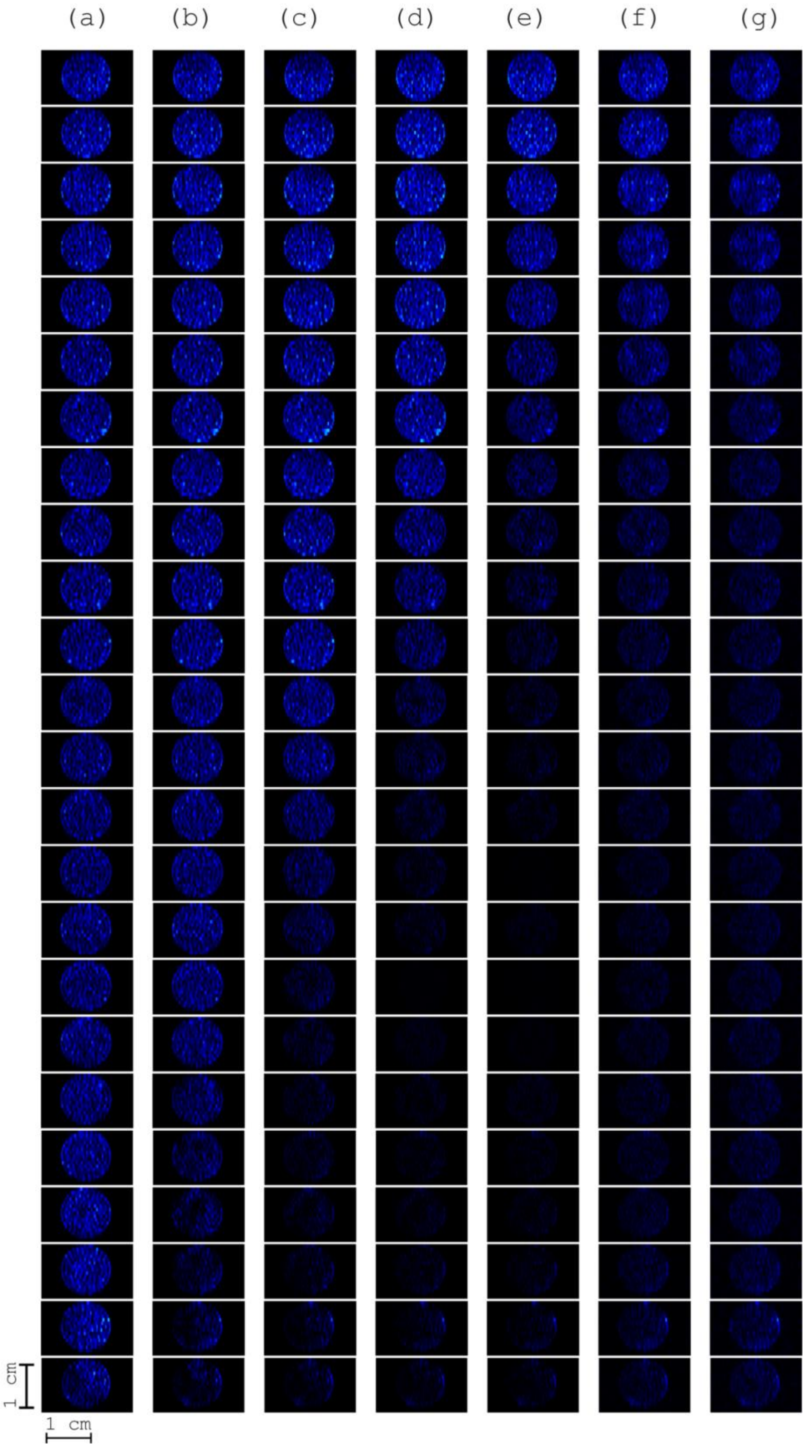

Figure 2.20: A time series of MRI images showing the displacement of 50 mM CTAB solution through a packed bed by 100 mM sodium salicylate solution, at a flow rate of 4 ml/hr. A pixel array of 256 x 128 x 16, has been compressed to 32 x 128 x 16 with the 32 horizontal images for each image being displayed here at 2 minute intervals.

While these horizontal plots enable the exact position and growth of the fingers forming to be characterised, they confirm the behaviour displayed in the vertical images. This is due to the fact that the fingers do not undergo splitting and shielding and do not take a tortuous path through the packed bed.

2.3.3 Displacement of sodium salicylate solution through a packed bed by CTAB

In Figure 2.21 a time series of horizontal images is shown for the displacement of sodium salicylate by CTAB. Each column of images show the horizontal images staggered along the length of the length of the packed bed.

In column (a) the first 4 horizontal images are filled with high signal showing the presence of CTAB. In the fifth image from the bottom, the base of a finger is seen at the top edge of the packed bed. This finger is seen to extend up through the next three images, becoming narrower the further along the packed bed it reaches. In column (b) this finger is seen to extend further into the packed bed, but also broaden, showing finger spreading. In column (c) the finger has not only spread across the top of the packed bed, but has also shifted around to the left hand side. In column (d) this behavior continues and in column (e) the finger occupies the top half of the packed bed until narrowing at the tip. It is in column (f) that we see finger splitting occur. The finger moving through the packed bed is broad and in the top two images of this column, two narrow fingers form on either side of the packed bed, indicated by the two small regions of high signal on the left and right hand side of the images. In the final column of images we see the shielding of one of these instabilities. The instability which formed on the right hand side of the packed bed has not grown in length, whereas the instability formed on the left of the packed bed has accelerated forward through the packed bed, broadening as it grows.

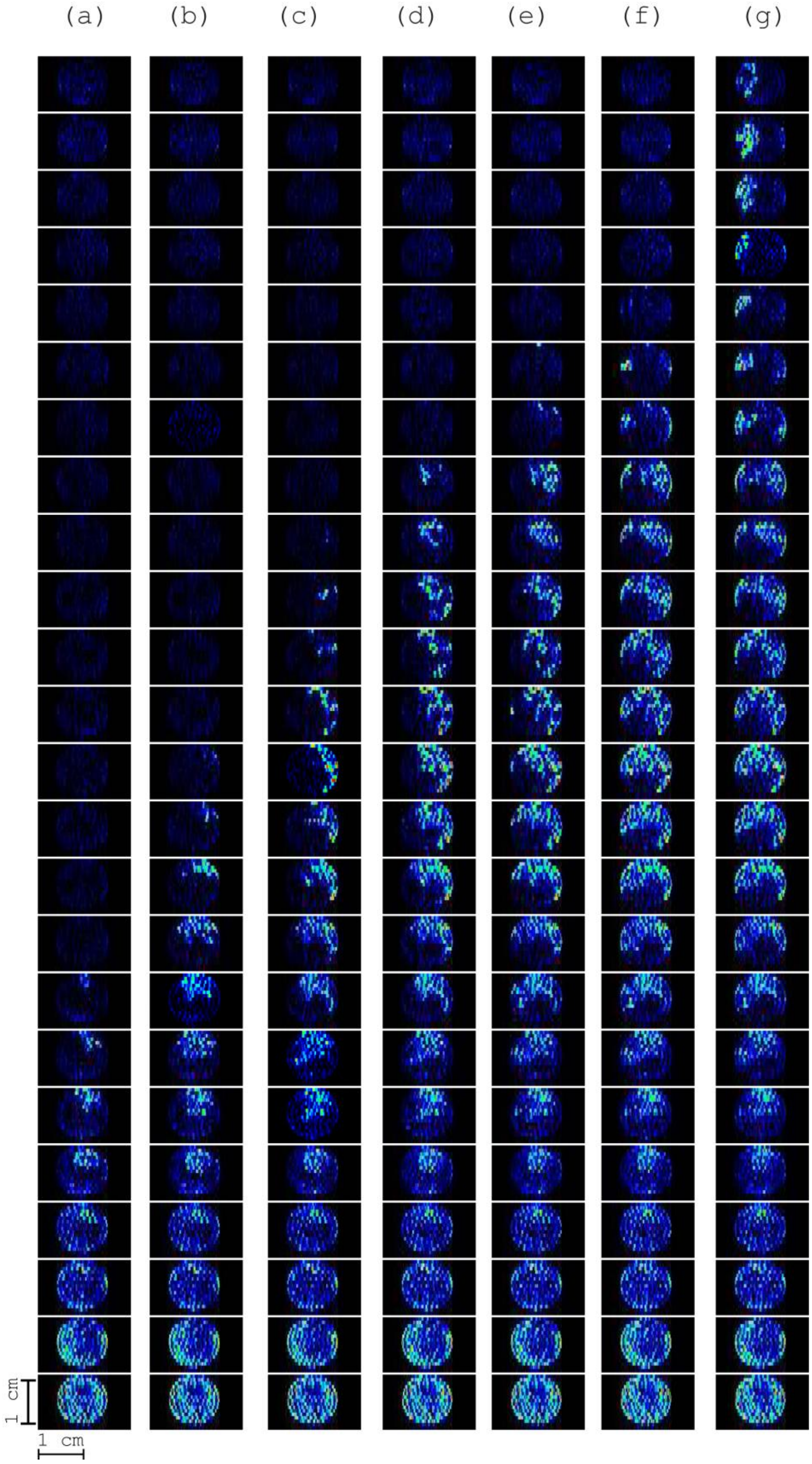

Figure 2.21: A time series of MRI images showing the displacement of 100 mM sodium salicylate solution through a packed bed by 50 mM CTAB solution, at a flow rate of 1 ml/hr. A pixel array of 256 x 128 x 16, has been compressed to 32 x 128 x 16 with the 32 horizontal images for each image being displayed here at 2 minute intervals.

In the vertical images displayed for this experiment, the high signal regions appeared patchy and disconnected and little information could be seen about the broadening nature of the finger. The additional information acquired from the horizontal images shows how the spreading of the finger and its movement through the packed bed results in these difficult to interpret vertical images. The horizontal images show in greater detail the spreading behavior of the finger. It is much clearer to see the splitting and shielding behavior that occurs in these images.

In Figure 2.22 the compressed slices of each 3-D image of the 2 ml/hr time sequence of MR images are shown. The first column shows that the packed bed is filled with CTAB up until the third image. In column (b) the CTAB solution moves up through the packed bed. However, a finger is seen to accelerate above the bulk movement of the fluid. In Image set (c) the finger moves further ahead of the bulk interface. This movement of the finger is seen to continue through the remaining images. Towards the end of the time sequence, the finger is seen to spread, broadening out across the packed bed. It is important to note that in image set (e) a second instability begins to form. However, its growth is quickly shielded by the more established finger. Over the course the finger shifts from be centred to spreading up the right hand side wall of the packed bed. This is the behaviour that means that in the vertical images a straight finger is not seen.

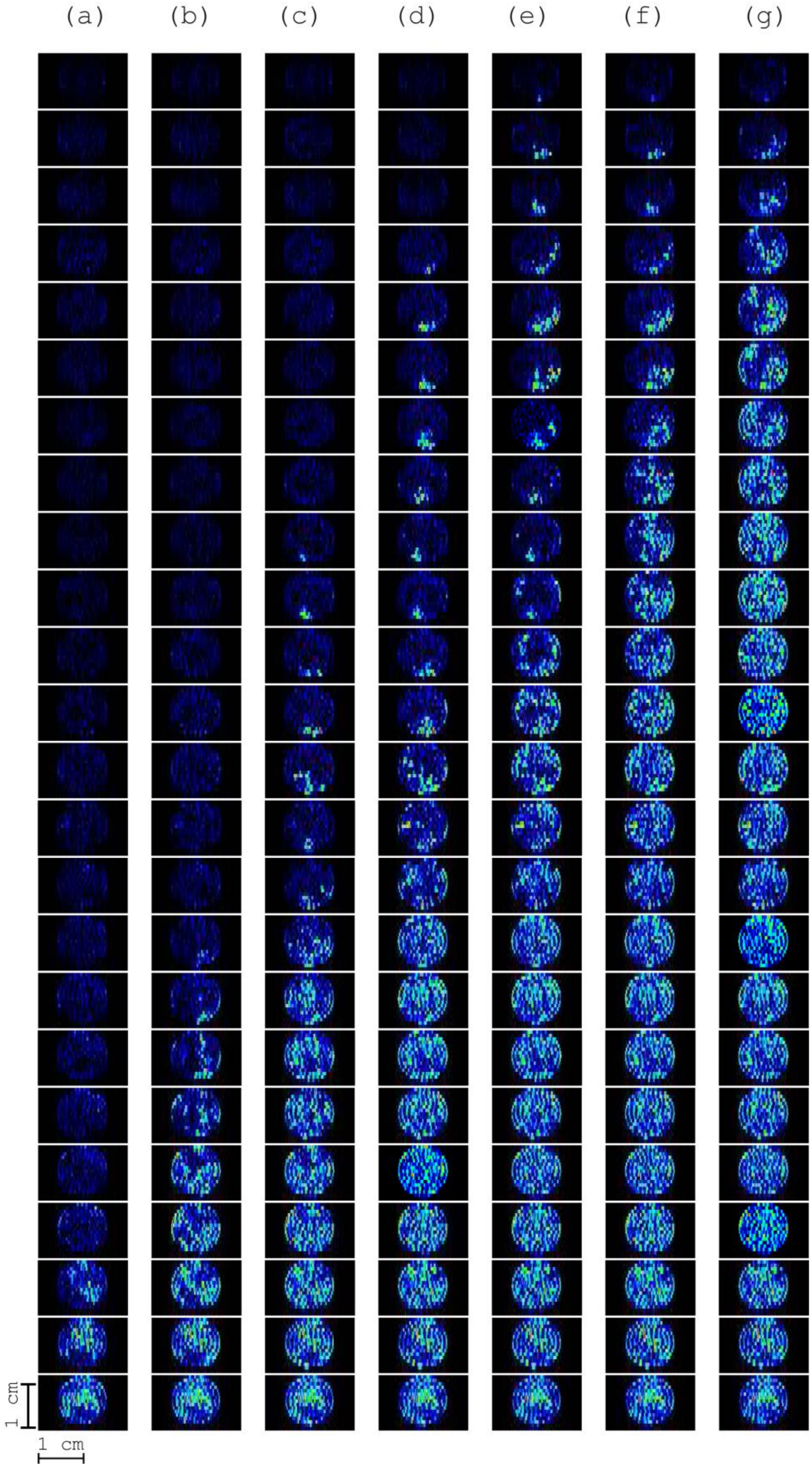

Figure 2.22: A time series of MRI images showing the displacement of 100 mM sodium salicylate solution through a packed bed by 50 mM CTAB solution, at a flow rate of 2 ml/hr. A pixel array of 256 x 128 x 16, has been compressed to 32 x 128 x 16 with the 32 horizontal images for each image being displayed here at 2 minute intervals.

In Figure 2.23 a time series plot of horizontal images for displacement of sodium salicylate by CTAB at a flow rate of 3 ml/hr. In column (a) the CTAB non-uniformly fills the first three images. In column (b) a finger forms on the left hand side of the packed bed moving ahead of the main interface. In column (c) this finger is seen to spread out to occupy the entire left hand side of the packed bed and then at its tip, spread over to the right hand side. In column (d) the bulk movement of fluid has shifted the main interface to almost half way up the packed bed and a small narrow finger now accelerates ahead of this main interface. In column (e) this finger broadens, but no further forward motion of the finger is seen. In the final two columns, we can see small fingers moving ahead of the main interface, but no main finger appears to dominate. This set of horizontal images provides, in much greater detail, the path of the fingers through the packed bed compared to the vertical images. Here the fingers are seen to undergo several stages of spreading and new fingers are formed in several instances. Vertical images show little indication of this behaviour. From this analysis, we can see that the fingers formed in the 3 ml/hr experiment have a much more tortuous path and undergo a greater deal of spreading and splitting than is indicated in the vertical images alone.

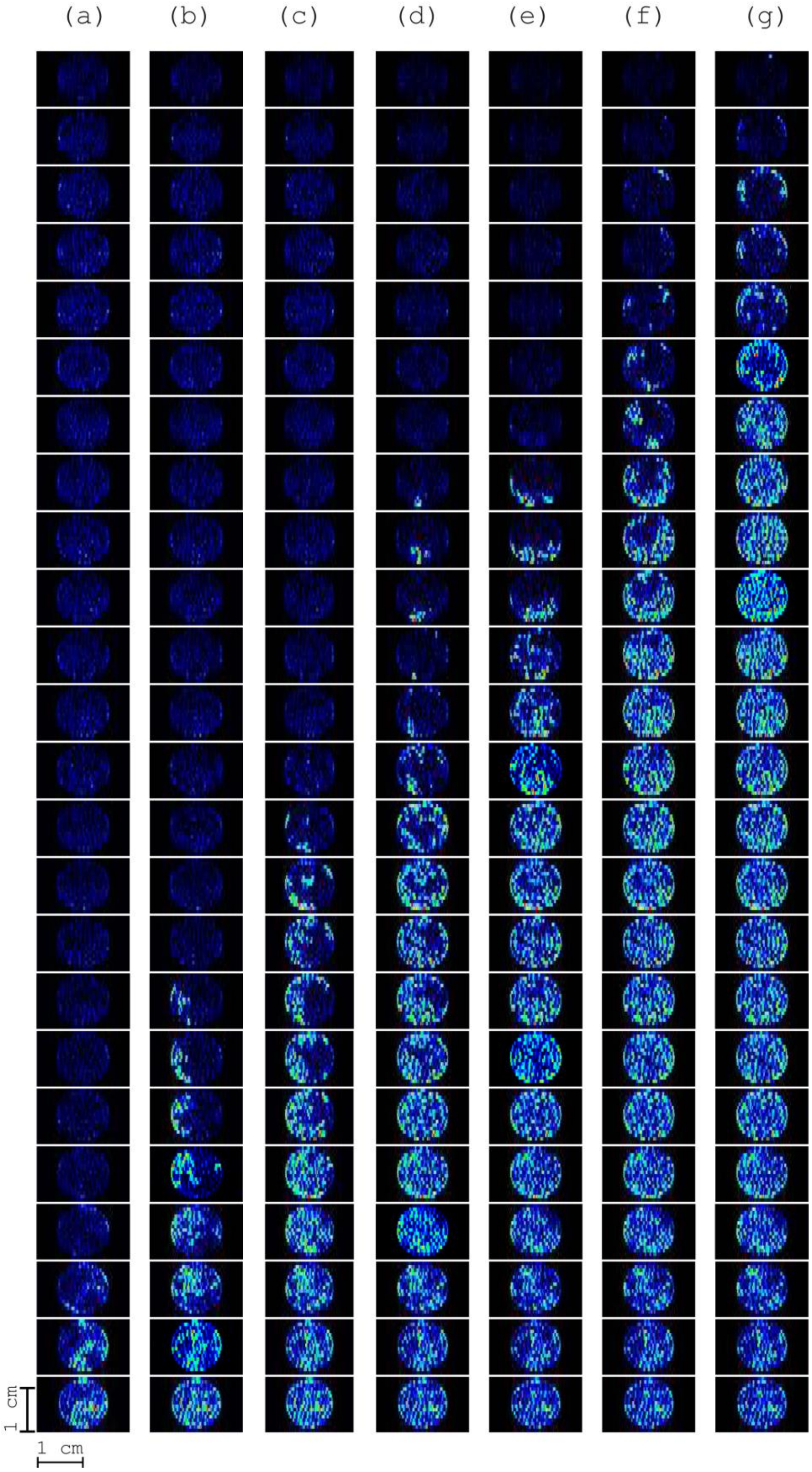

Figure 2.23: A time series of MRI images showing the displacement of 100 mM sodium salicylate solution through a packed bed by 50 mM CTAB solution, at a flow rate of 3 ml/hr. A pixel array of 256 x 128 x 16, has been compressed to 32 x 128 x 16 with the 32 horizontal images for each image being displayed here at 1 minute intervals.

In Figure 2.24 a time series of horizontal images is shown for the experiment repeated at 4 ml/hr. In column (a) we see the interface between the two solutions in the fourth image. In column (b) the formation of two separate fingers is seen. The first finger forms on the left hand side of the packed bed and the second finger forms on the right hand side. The finger on the right hand side of the packed bed moves slightly forward of the finger on the left hand side. In column (c) although the images are not completely filled with high signal CTAB solution a more uniform flow is seen through the packed bed. In column (d) this behaviour is again seen, with a very broad instability forming at the interface. The images in column (e) are much more representative of plug flow moving through the packed bed, with light instability formation only seen right at the interface. In column (f) a finger forms at the very top of the packed bed occupying the left hand side of the images. The finger seen is broad and is quickly consumed by the moving interface (column (g)).

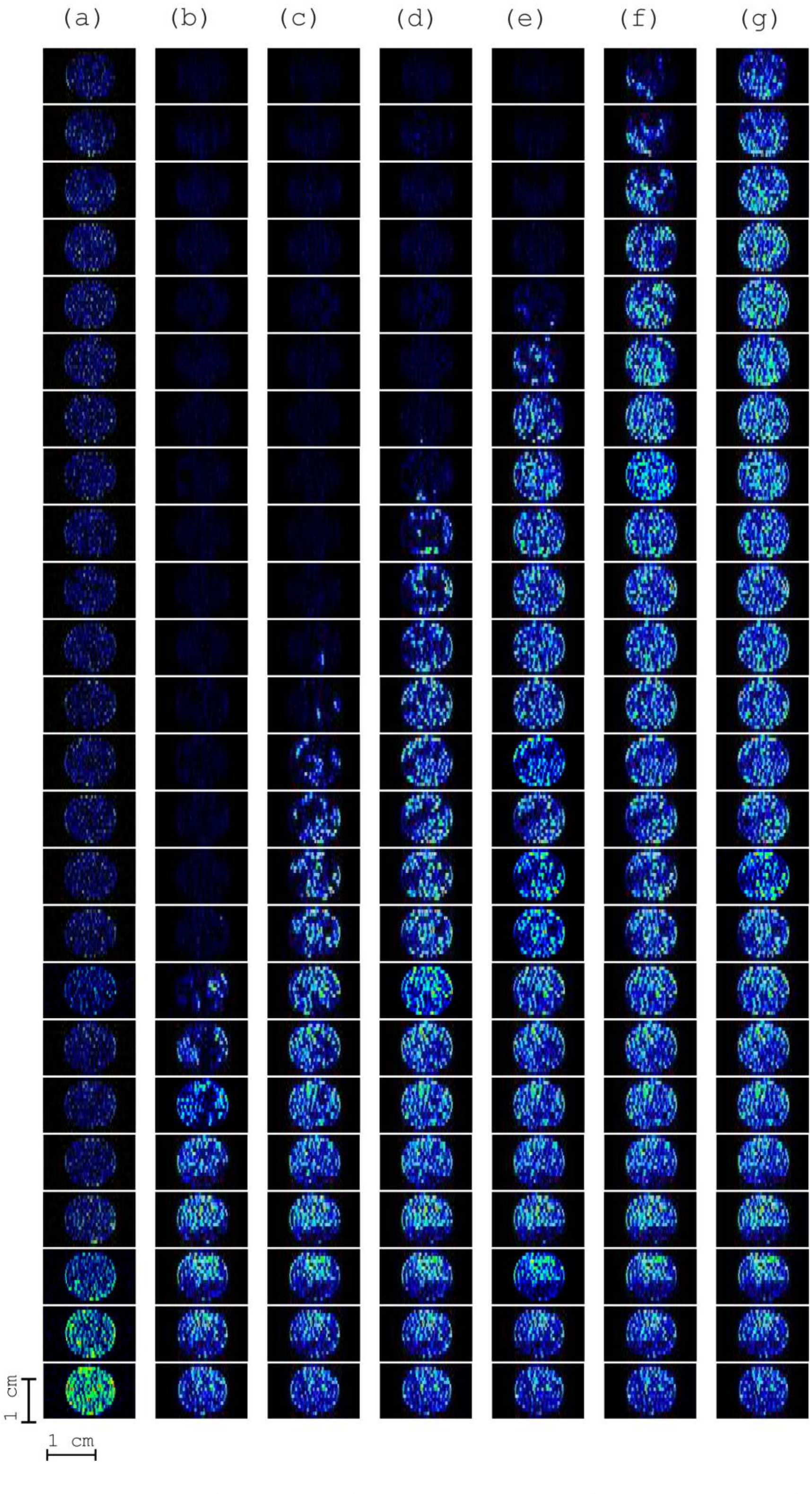

Figure 2.24: A time series of MRI images showing the displacement of 100 mM sodium salicylate solution through a packed bed by 50 mM CTAB solution, at a flow rate of 3 ml/hr. A pixel array of 256 x 128 x 16, has been compressed to 32 x 128 x 16 with the 32 horizontal images for each image being displayed here at 1 minute intervals.

Again the effect of flow rate is seen to agree with the previous findings of Podgorski *et.al*[8]. At lower flow rates narrower fast moving fingers develop through the packed bed and are seen to exhibit spreading, shielding, and splitting behaviour. At higher flow rates, spreading and splitting is still seen but fingers are much more short-lived at these flow rates due to the fast movement of the bulk CTAB through the packed bed.

The horizontal plots have been able to reveal more information on the formation and development of fingers that take a tortuous path and undergo splitting and shielding. By presenting a variety of complimentary images a more complete description of the finger development can be presented.

2.3.4 Root Mean Square Deviation Analysis

While other images shown in this section provide a great deal of information about the formation and development of fingers and its dependence on flow rate, the analysis carried out is qualitative. Many attempts have been made to try and quantitatively analyse the formation of fingers. While the use of finger width[18] and classification of finger shape[8] provide useful data in a Hele-Shaw cell, these analysis techniques are much more difficult to apply in 3-D porous media. For this reason, a new technique specifically designed to monitor the distribution of the high signal fluid, CTAB, throughout the packed bed has been developed. High signal fluid was determined by taking a 1-D profile through a packed bed filled with 50 mM CTAB and identifying the lowest signal intensity which could not be attributed to the packing material. This signal intensity was then used as a threshold value to distinguish between high signal fluid and the rest of the system. A time series of model plug flow was generated for each flow rate and the RMS pixel position, for high signal pixels, was calculated. The method for generating these model plots is explained fully in the next section of this chapter. We then calculated the position of every high signal pixel within each experimental image and recorded how its position deviated from the root mean square (RMS) pixel position of high signal pixels in its corresponding plug flow model. This deviation was plotted on to 3 different histograms. One plot showing the pixel deviation for each plane of the image, the x,y and z directions. It is important to note that a time series of model plots was used for this analysis; therefore the model is effectively a moving frame. This was done to ensure that any spreading out of the pixel distributions seen could be attributed to the development of instabilities rather than a representation of the bulk flow through the packed bed. This enabled the features in the plots to be more representative of the deviations from plug flow rather than a collective representation of the bulk flow as well as the instabilities formed. This analysis has only been carried out on the displacement of sodium salicylate by CTAB as with the reverse arrangement it was not possible to exclude the packing material from the analysis, which resulted is unreadable data. Macros used for developing the model plug flow plots and the RMS deviation plots can be found in appendix 1 of this thesis.

2.3.4.1 Production of models and analysis technique

To carry out this analysis a plug flow model is required so that any deviation from plug flow in each 3-dimensional image can be seen. A 3-dimensional model of a packed bed was constructed using a real 3-D MR image of a packed bed filled with high signal fluid as a template for the distribution of packing. This template was completely emptied of any high signal pixels so that the model could be progressively filled with high signal pixels at a rate determined by the flow rate being investigated. The linear flow rate was calculated from the initial flow rate and the porosity of the model packed bed. The macro used to calculate this linear velocity can be found in appendix 1 of this thesis. A plug flow model time sequence was created for each flow rate, taking into account the initial flow rate, image acquisition time and the delay between the acquisitions of real MR images. The root mean square pixel position of every plug flow model, which indicates the center of pixel distribution throughout the packed bed, is calculated. Then the deviation of every high signal pixel in the real 3-D image from this RMS position is calculated. The deviation from the model RMS in the z, x and y directions was calculated. These deviations were plotted in three separate histograms, each relating to a Cartesian axis. The number of pixels, $N(\boldsymbol{r})$, at each given deviation indicates the distribution of high signal pixels in an image. This in turn can be used to indicate the presence of finger formations.

To fully understand how finger formation would be indicated in the RMS plots, rudimentary models were created of basic finger structures and their growth through a packed bed. A time series of model images were created for each type of finger structures. In Figure 2.25 a schematic of each model produced is seen. The models are (a) plug flow, (b) a single central finger, (c) a single side finger and (d) two side fingers.

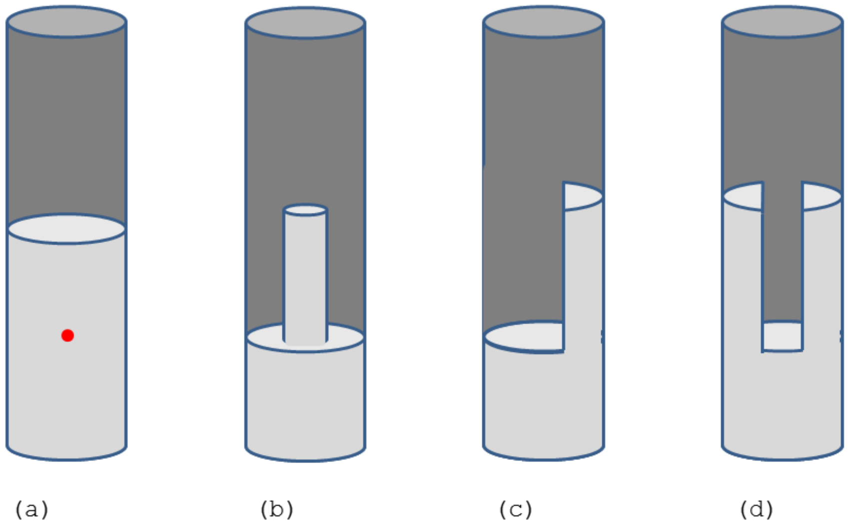

Figure 2.25: A schematic diagram showing the structure of model flow structures where, light grey indicates high signal pixels. The models represent (a) plug flow, (b) a single central finger, (c)a side finger and (d) a double finger. The spot in (a) represent the RMS pixel position.

2.3.4.2 Analysis of models

By carrying out the RMS deviation analysis on each of these models, it was possible to identify the features in the RMS deviation plots that were attributed to each finger structure.

In Figure 2.26 the root mean square deviation plots for the plug flow model are shown.

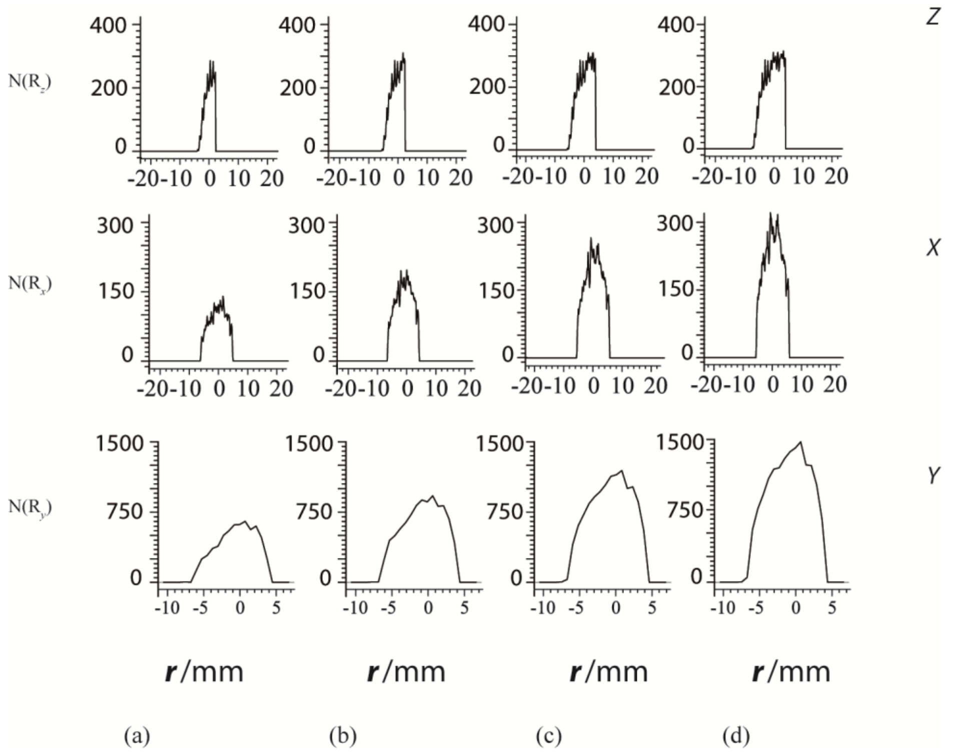

Figure 2.26: RMS deviation plots, for the z,x and y axis for a plug flow model, shown at 2 minute intervals. Where N(r)is the number of pixels at a given deviation.

Deviations along the Z axis, the direction of flow, are evenly distributed around zero. As the model images are filled with high signal pixels the deviation from the model RMS continue to be evenly distributed around zero. As time progresses this peak broadens showing the spread of high signal pixels through the packed bed. The plots for the *x* axis, deviations across the width of the packed bed, show a peak evenly distributed around Zero. As the packed bed is filled, the shape of the peak remains the same, but the height increases as more pixels fill the model. The same is seen for the deviation plots for the Y axis. Again, as more pixels fill the model, the height of the peak is increased. All of the plots in the *z*, *x* and *y* directions show small peaks at the top of each distribution. These are caused by the presence of packing.

In Figure 2.27 the root mean square deviation plots for the single central finger model are shown.

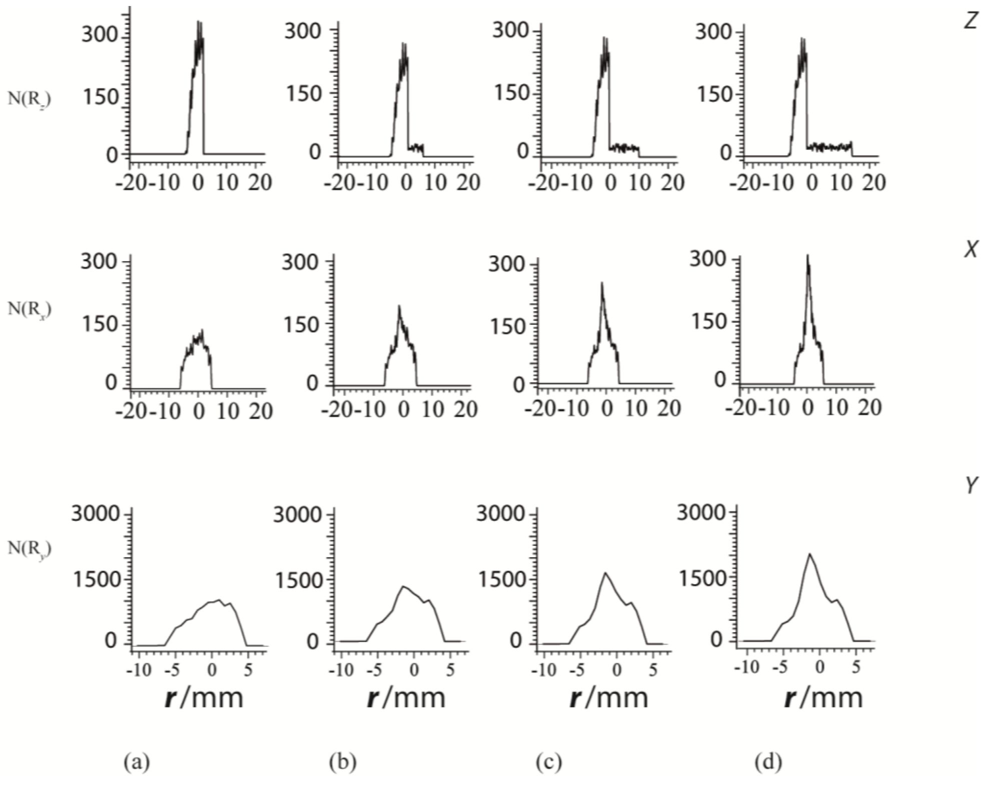

Figure 2.27: RMS deviation plots, for the z,x and y axis for a single, central finger model, shown at 2 minute intervals. Where N(r)is the number of pixels at a given deviation, *r*.

The first of the *z* plots show an evenly distributed peak around zero. This is because no finger has yet formed at the interface of the model. In the second *z* plot, a small number of pixels are seen at a higher deviation. The number of pixels and their positive deviation from the RMS position, increases over time. This is because as a finger develops, the number of pixels positioned ahead of the bulk flow increases. In the *x* plots, we see a peak form in the centre of the distributions which grows in height, as the finger develops. This indicates that a greater number of high signal pixels are occupying the centre of the packed bed. The same is also seen in the *y* plots.

In Figure 2.27 the root mean square deviation plots for the single central finger model are shown.

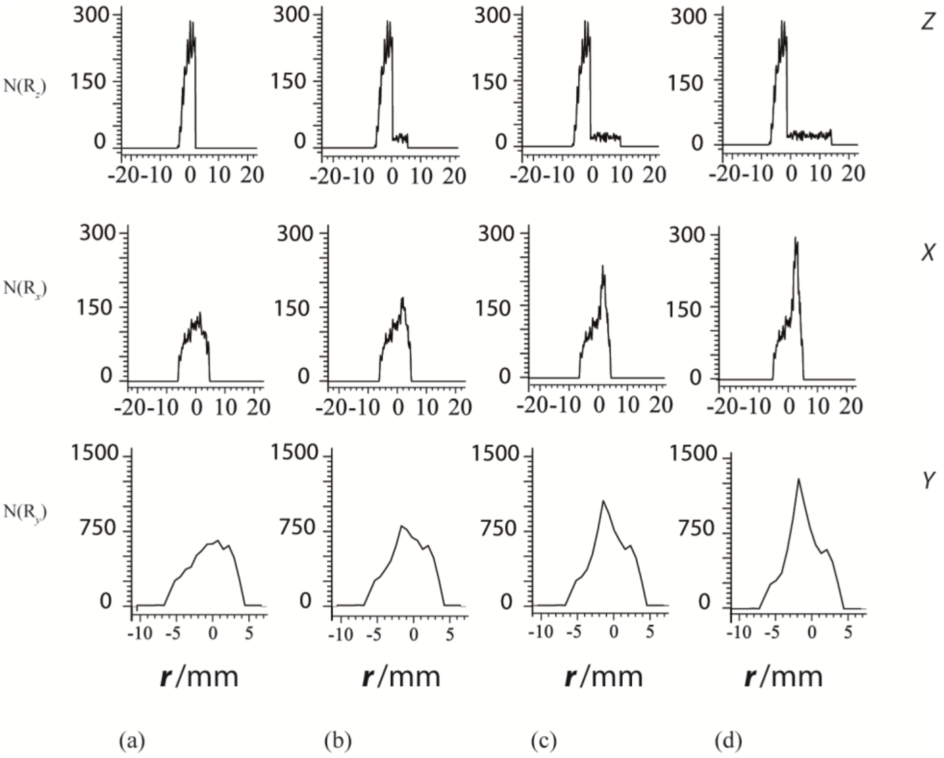

Figure 2.28 RMS deviation plots, for the z,x and y axis for a side finger model, shown at 2 minute intervals. Where N(r)is the number of pixels at a given deviation, *r*.

The deviation plots in the *z* direction show the same features as were seen in the plots for a single central finger. However, in the *x* plots the peak previously seen at the centre of the distributions is now shifted to the right hand side. This indicates finger formation on the right hand side of the model packed bed. As no difference in pixel distribution is seen in the *y* direction between a side finger and a central finger, these plots are very similar.

As finger splitting was a regular occurrence in the flow experiments, it is useful to have a model of a packed bed containing two fingers. In Figure 2.29 the root mean square deviation plots for the formation of two side fingers are shown.

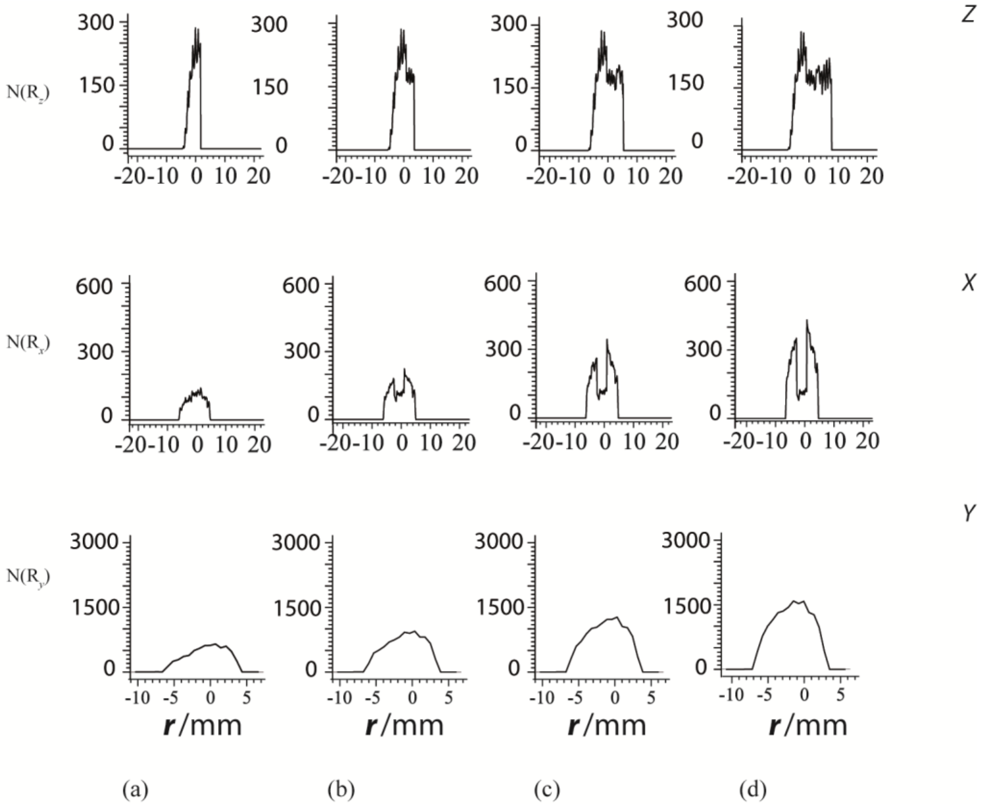

Figure 2.29: RMS deviation plots, for the z,x and y axis for a double finger model, shown at 2 minute intervals. Where N(r)is the number of pixels at a given deviation, *r*.

The z plots again show a shift in pixel deviation towards positive values. However, as two fingers are now forming, a greater number of high signal pixels are positioned forward of the RMS pixel position. This is indicated by a greater number of pixels being shown at higher deviations. The presence of two separate fingers becomes clear when looking at the plots for the *x* axis. Instead of one single peak, as previously seen a peak forms at both positive and negative deviations. This shows that the pixels in the system are distributed away from the RMS pixel position with few, or no high signal pixels being present around the RMS position. Pixels are evenly distributed around the RMS pixel position along the *y* axis. This is seen because the fingers have been plotted along the *x* axis in the model. If the fingers had been plotted along the *y* axis, we would expect to see the same features in the y plots as we did in the *x* plots.

From this analysis of rudimentary models we are able to identify the features in RMS plots that indicate the formation of fingers. We are also able to determine the position at which these fingers form by observing where peaks appear in the *x* and *y* plots. We are now able to able to apply this analysis technique to the 3-dimensional MR images showing the displacement of sodium salicylate by CTAB at 1, 2 3 and 4 ml/hr.

2.3.4.3 RMS analysis of displacement of sodium salicylate by CTAB

In Figure 2.30 the root mean square deviation plots are shown for the displacement of sodium salicylate by CTAB at 1 ml/hr.

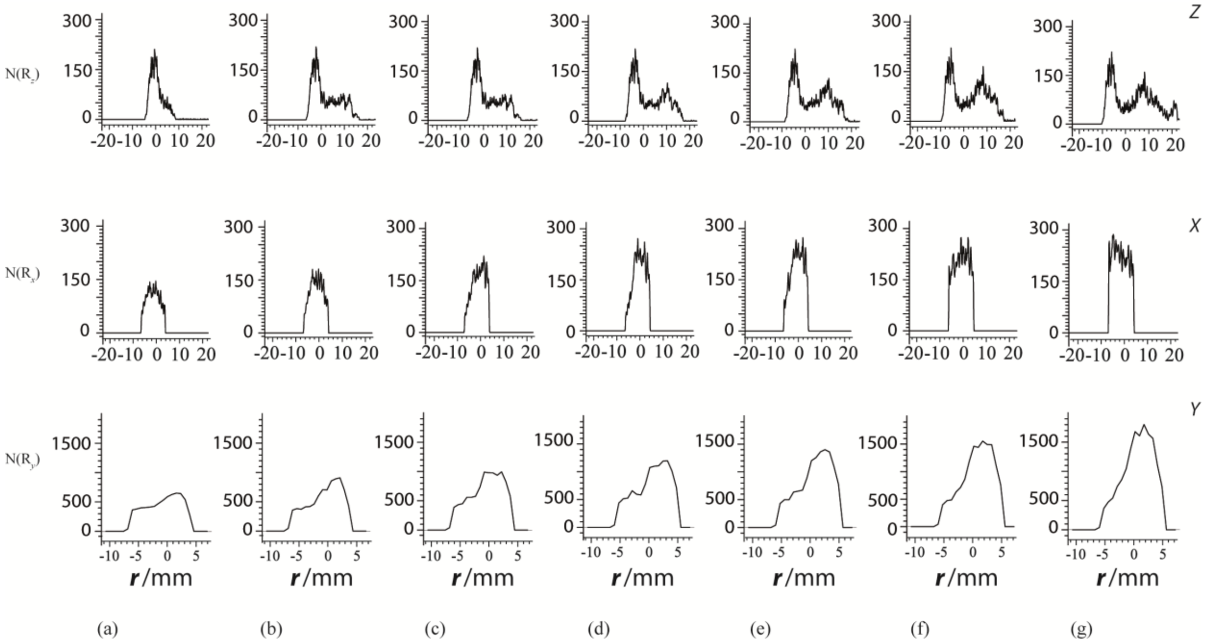

Figure 2.30: RMS deviation plots, for the z,x and y axis for the displacement of 100 mM sodium salicylate by 50 mM CTAB at a flow rate of 1ml/hr.Plots are representative of images taken at 2 minute intervals. Where N(r)is the number of pixels at a given deviation, *r*.

Each set of *z*, *x*, *y* plots corresponds to the images in Figure 2.13. The Z plot in the first set of deviations shows that pixel distribution along the *z* axis is not centred about Zero. The right hand side of the distribution tails off showing the shift of pixels along the *z* axis. From our analysis of rudimentary models it is known that this is an indication of finger formation along the *z* axis. In plots (d) to (g) we see an increase of pixels at higher deviations. This can be contributed to the broadening of a finger in the later stages of the experiment. The deviations along the *x* axis appear to be relatively evenly distributed about the RMS pixel position. This shows there is no finger formation across the width of the packed bed. There is however, a peak formed at higher deviations in the *y* plots. This indicates the formation of the finger occurs to the rear of the packed bed. This observation matches those seen in the horizontal plots previously shown for this experiment.

In Figure 2.31 the root mean square deviation plots are shown for the displacement of sodium salicylate by CTAB at 2 ml/hr. This time, the plots for deviations across the *z* axis show both features indicative of finger formation and plug flow. The broadening distributions show the bulk movement of CTAB through the packed bed. However, the small peaks seen at the highest positive deviations show the development of narrow fingers. In plot (b) of the *x* plots, we see a small peak just above zero. This is attributed to the formation of a finger slightly off centre in the packed bed. No other finger formation is seen in the *x* plots, showing that any fingers that form are either in the centre of the packed bed in regards to *x*, or are too small to have any effect on the plots. The same is seen for the *y* plots. When looking back at the horizontal images for this experiment, it can be seen that a narrow finger forms through the packed bed. This demonstrates a limitation of this technique, when analysing narrow fingers as they do not contain enough high signal pixels to contribute significantly to the RMS distributions.

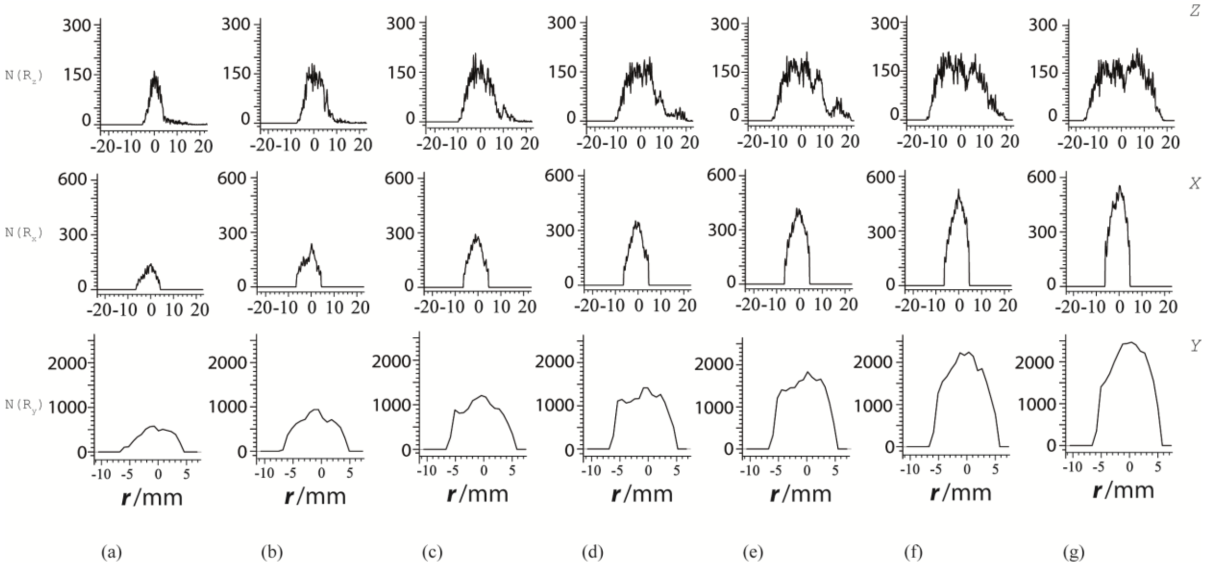

Figure 2.31: RMS deviation plots, for the z,x and y axis for the displacement of 100 mM sodium salicylate by 50 mM CTAB at a flow rate of 2ml/hr. Plots are representative of images taken at 2 minute intervals. Where N(r)is the number of pixels at a given deviation, *r*.

In Figure 2.31 the root mean square deviation plots are shown for the displacement of sodium salicylate by CTAB at 3 ml/hr.

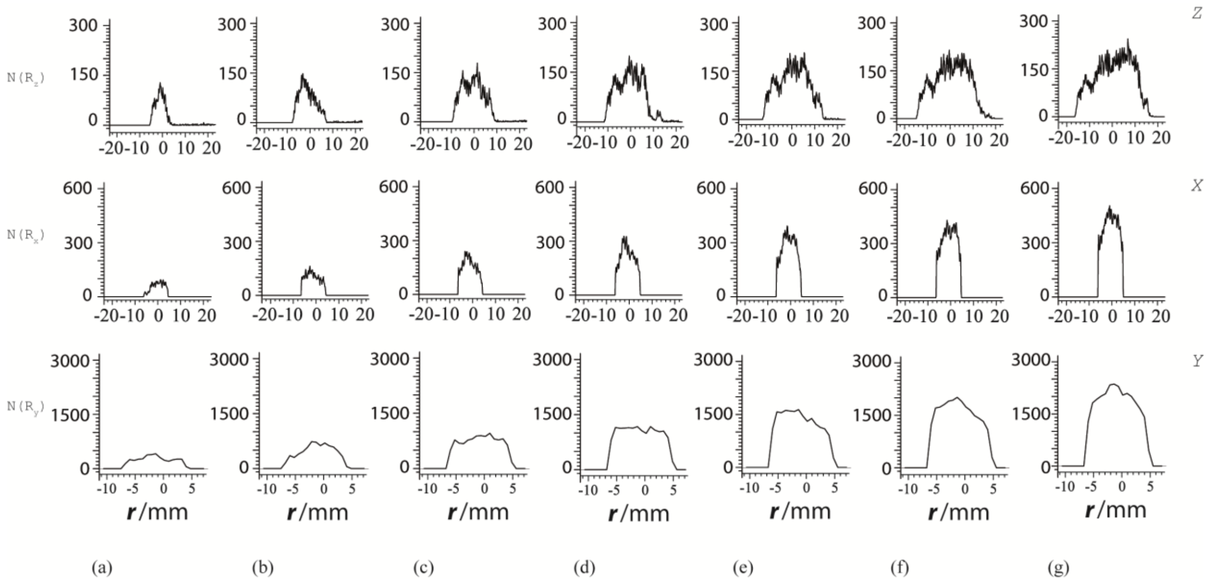

Figure 2.32: RMS deviation plots, for the z,x and y axis for the displacement of 100 mM sodium salicylate by 50 mM CTAB at a flow rate of 3 ml/hr. Plots are representative of images taken at 1 minute intervals. Where N(r)is the number of pixels at a given deviation, *r*.

The plots for the *z* axis again indicate the presence of plug flow through the packed bed. In plot (d) there is indication of a small finger forming at higher deviations, but this feature is soon lost in the broadening of the main peak. The distributions in the first four plots for the *x* axis indicate the formation of a finger on the left hand side of the packed bed. When looking back at the horizontal images for this experiment, this finger can clearly be seen. The plots for the *y* axis show from plot (d) to plot (f) that more high signal pixels are distributed towards the front of the packed bed. This instability at the front of the packed bed is also seen in the horizontal images.

In Figure 2.30 the root mean square deviation plots are shown for the displacement of sodium salicylate by CTAB at 4 ml/hr.

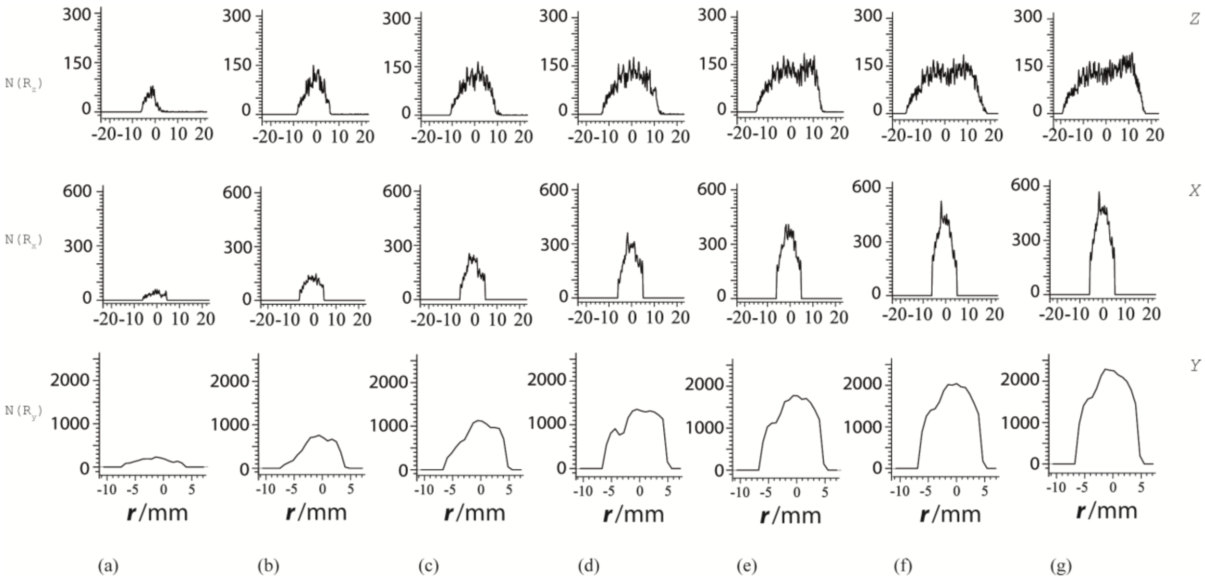

Figure 2.33: RMS deviation plots, for the z,x and y axis for the displacement of 100 mM sodium salicylate by 50 mM CTAB at a flow rate of 4 ml/hr. Plots are representative of images taken at 1 minute intervals. Where N(r)is the number of pixels at a given deviation, *r*.

The z and x plots for this experiment are much more indicative of plug flow. However, there are some small deviations. For the z axis, plot (e) and (f) show a higher distribution of pixels towards a greater positive deviation. This indicates the formation of a short lived instability that is quickly consumed by the bulk movement of the interface. This behavior is seen in the 3-D horizontal images for this experiment, with any instabilities forming only moving slightly ahead of the bulk interface. The plots for the y axis show a higher number of pixels at positive deviations. This indicates that any instability that does form will be towards the rear of the packed bed. This feature however, is not strongly indicated by these plots and is also not clearly seen in the 3-D horizontal images for this experiment.

This RMS deviation analysis enables the identification of finger formation through a packed bed. Details can be extracted from the plots, which indicate the position, length and width of any instabilities formed. The RMS analysis carried out here confirms the trends previously seen in the vertical and horizontal images. This technique, however, works best when combined with the vertical and horizontal images proved by the MR experiments.

2.4 Conclusion

We have investigated the development of viscous fingers in a packed bed when a solution of CTAB is bought into contact with a solution of sodium salicylate under flow, to form a viscous solution of wormlike micelles. Relaxation measurements indicated that MR contrast could be achieved through the use of RARE imaging, without the addition of any contrast agent required. Several imaging T_2-dependent imaging techniques were employed to monitor the formation and development of the wormlike micelle layer. A time series of MR images was acquired for the displacement of CTAB by sodium salicylate and vice versa, for four different flow rates. It was found that as the flow rate was increased, the fingers formed became broader and did not move forward of the main interface, by any great extent. The structure of any fingers formed was found to be dependent on which chemical was being displaced. This could be attributed to using different concentrations of each reactant. However, further studies would be needed to confirm this. Several analysis techniques were applied to the three dimensional images. The compression of the images along the z axis enabled fingers to be seen more clearly. A second, qualitative technique which plotted pixel distribution about a RMS pixel position was able to indicate the presence of fingers, as well as helping to identify the structure of any instability in the packed beds.

2.5 References

1. Nagatsu, Y., et al., *Spiral pattern in a radial displacement involving a reaction-producing gel.* Physical Review E, 2008. **78**(2): p. 026307.
2. Nagatsu, Y., et al., *Experimental study on miscible viscous fingering involving viscosity changes induced by variations in chemical species concentrations due to chemical reactions.* Journal of Fluid Mechanics, 2007. **571**: p. 475-493.
3. Nagatsu, Y., et al., *Experimental evidence of reaction-driven miscible viscous fingering.* Phys. Rev. E, 2012. **85**(1): p. 015304.
4. Plante, L.D., P.M. Romano, and E.J. Fernandez, *Viscous Fingering In Chromatography Visualized Via Magnetic-Resonance-Imaging.* Chemical Engineering Science, 1994. **49**(14): p. 2229-2241.
5. Broyles, B.S., et al., *Visualization of viscous fingering in chromatographic columns.* Journal of Chromatography A, 1998. **822**(2): p. 173-187.
6. Yuan, Q.S., et al., *Flow distribution in chromatographic columns.* Journal of Chromatography A, 1999. **831**(2): p. 149-165.
7. Schubert, B.A., E.W. Kaler, and N.J. Wagner, *The microstructure and rheology of mixed cationic/anionic wormlike micelles.* Langmuir, 2003. **19**(10): p. 4079-4089.
8. Podgorski, T., et al., *Fingering instabilities of a reactive micellar interface.* Physical Review E, 2007. **76**(1): p. 016202.
9. Yang, J., *Viscoelastic wormlike micelles and their applications.* Current Opinion in Colloid & Interface Science, 2002. **7**(5-6): p. 276-281.
10. Nagatsu, Y., et al., *Miscible viscous fingering with a chemical reaction involving precipitation.* Physical Review E, 2008. **77**(6): p. 067302.

11. Carr, H.Y. and E.M. Purcell, *Effects Of Diffusion On Free Precession In Nuclear Magnetic Resonance Experiments.* Physical Review, 1954. **94**(3): p. 630-638.
12. *www.magritek.com*.
13. Hennig, J., A. Nauerth, and H. Friedburg, *Rare Imaging - a Fast Imaging Method for Clinical Mr.* Magnetic Resonance in Medicine, 1986. **3**(6): p. 823-833.
14. *SBDS database: ^{1}H NMR spectrum for lithium salicylate at 400 MHz; http://riodb01.ibase.aist.go.jp/sdbs/ (National Institute of Advanced Industrial Science and Technology, date accessed 25/10/12)*.
15. Britton, M.M., *Measurement of the concentration of Mn2+ and Mn3+ in the manganese-catalyzed 1,4-cyclohexanedione-acid-bromate reaction using redox-triggered magnetic resonance spectroscopy.* Journal of Physical Chemistry A, 2006. **110**(49): p. 13209-13214.
16. Fernandez, E.J., et al., *The Effects Of Permeability Heterogeneity On Miscible Viscous Fingering - A 3-Dimensional Magnetic-Resonance-Imaging Analysis.* Physics Of Fluids, 1995. **7**(3): p. 468-477.
17. Magtritek, *Prospa version 2.1*, http://www.magritek.com/prospa.html.
18. Saffman, P.G. and G. Taylor, *The Penetration of a Fluid into a Porous Medium or Hele-Shaw Cell Containing a More Viscous Liquid.* Proceedings of the Royal Society of London Series a-Mathematical and Physical Sciences, 1958. **245**(1242): p. 312-329.

3 Glycerol

While the focus of much research is now on the reactive systems that produce flow instabilities[1-6], for many years research aimed to understand why these instabilities form and what parameters influence their development and structure[7-12]. The first use of MRI to visualize fingers in a real porous media was carried out by Fernandez *et. al* and investigated the movement of a band of glycerol through size exclusion chromatography columns[13]. Both two and three dimensional imaging sequences were utilized to acquire images of these systems[13, 14] with complimentary numerical simulations[10] also used. Initial flow rate and viscosity were both found to influence finger development, with the increase of both showing narrower, faster moving fingers. This behavior was also seen when carrying out similar investigations with various other fluids[15]. While the investigations using MRI shifted focus to the improvement of chromatography column design[16-18], Hele-Shaw cell investigations have also shown the same trends[7, 9, 19-22]. Even reactive systems with a pre-existing viscosity gradient show similar behavior with regards to flow rate and viscosity[23]. Here we have used MRI to image the flow of various glycerol solutions through a packed bed reactor. Several flow rates and concentrations of glycerol were used for these experiments so that we had representation images for the influence of both flow rate and viscosity. The purpose of this study was to be able to apply the root mean square pixel analysis, described in chapter 2, to a non-reactive system and provide further information regarding any behavior and trends seen.

3.1 Experimental

3.1.1 Experimental Materials

Glass tubes 30 cm in length and 11 mm inner diameter were used to construct all packed bed reactors used. For all experiments sand (BDH) with a particle size ranging from 0.1 - 0.3 mm was used as packing material. Glycerol (Sigma-Aldrich ≥ 99%) and distilled water were used to make all glycerol solutions ranging from 20% to 80% glycerol. The dynamic viscosity of the glycerol solution used are reported as 1.54 mPa S for 20%, 3.18 mPa s for 40%, 8.82 mPa S for 60% and 45.9 mPa S for 80%. $MnSO_4 \cdot 4H_20$ (BDH ≥ 98.5%) made up to a 20 mM solution with distilled water was used to make all solutions for relaxation and flow experiments.

3.1.2 Packed bed reactor setup

The Packed bed reactor was setup as in the previous chapter. Figure 1.1 can be referred to for exact experimental setup. A packed bed comprising a cylindrical glass tube of length 30 cm and internal diameter 11 mm, was packed with sand washed in nitric acid and then distilled water to remove paramagnetic species. The packed bed was held vertically in a 7T magnet. The packed bed reactor was filled from below with 20 mM manganese sulphate and a band of glycerol was created above this in the packed bed. For experiments investigating the effect of flow rate on the formation of viscous fingers the glycerol band was 0.5 ml in volume with a glycerol concentration of 60%. For experiments investigating the effect of glycerol concentration on the formation of instabilities the volume of the glycerol band was increased to a volume of 2 ml and the flow rate was kept at 30 ml hr^{-1}. The glycerol band was formed by pipetting a slurry of sand and the desired glycerol solution into a packed bed half filled with sand and a 20 mM manganese sulphate solution. After the addition of the glycerol band, more sand and 20 mM manganese sulphate was used to fill the packed bed reactor. The packed bed reactor was positioned in the spectrometer so that the interface between the two solutions was visible in the bottom third of the observable region of the 25 mm radiofrequency resonator with an observable region of 2.5 cm x 5 cm. The $MnSO_4$ solution was pumped from below using a syringe pump (Harvard pump 22) at flow rates of 4, 9 and 30 ml hr^{-1} for flow rate investigations.

3.1.3 Nuclear magnetic spectroscopy

All magnetic resonance (MR) experiments were acquired using a Bruker DMX 300 spectrometer, operating at a ^1H resonance frequency of 300.13 MHz. A 25 mm radiofrequency resonator was used for all spectroscopy experiments. Data was acquired using XWIN-NMR 2.6 software. Measurements were carried out in a 5 mm NMR tube. All samples were allowed to equilibrate to the temperature inside the magnet bore, 290.8± 0.4 K, for 30 minutes before any measurements were acquired. T_1 relaxation measurements were made for glycerol solutions ranging from 20% to 80% glycerol using inversion recovery experiments. 16 experiments were performed with IR delays logarithmically spaced between 5 μs and 20 s. 90° and 180° rf pulses were 45.67 and 91.34 μs respectively at an attenuation of 0 db. A spectral width of 10 KHz was used with 4 signal averages, each acquiring 16k complex points. The T_1 relaxation times for 25%, 50%, 75% and 99% glycerol were 689 ± 20 ms, 433 ± 15 ms, 320 ± 12 ms and 280 ± 18 ms respectively. Carr-Purcell-Meiboom-Gill (CPMG) experiments were performed to measure the T_2 values for the solutions, acquiring a maximum of 512 echoes with an echo spacing of 20 ms. The T_2 relaxation times for 25%, 50%, 75% and 99% glycerol were 367 ± 17 ms, 220 ± 15 ms, 90 ± 16 ms and 18 ± 9 ms respectively. All T_1 and T_2 relaxation measurements were acquired through analysis carried out in Prospa NMR analysis software[24].

3.1.4 Magnetic Resonance Imaging

All magnetic resonance imaging was carried out using PARAVISION 2.1.1 software. A 25 mm radiofrequency resonator with an observable region of 2.5 cm x 5 cm was used for all imaging experiments. Two dimensional, vertical slice, images were acquired using the fast spin-echo imaging technique RARE[25], with a field of view ranging from 50 mm × 2.5 mm to 30 mm x 15 mm, depending on the experiment, with a pixel array of 256 (z) × 128 (x), respectively and a slice thickness of 1 mm. The spectral width was 50 KHz and a RARE factor of 8 was used, giving an effective echo time of T_{eff} = 40 ms. This resulted in high signal intensity (SI) for the water in the glycerol solution and low SI for the manganese sulphate. The repetition time was T_R = 250 ms, with a time resolution between images of 60 s. All images were analysed using prospa NMR anaylysis software.

3.1.5 Optical imaging

The experimental setup used in all MRI experiments was used to optically investigate the formation of viscous fingers. A Canon A550 7.1 megapixel camera was used to video flow experiments run at 30 mL hr^{-1} for glycerol concentrations of 20%, 40%, 60% and 80%. In order for there to be optical contrast between the two solutions two drops of blue food coloring were added to the glycerol solutions. A snapshot was selected from the videos at 30 second intervals and presented as a time lapse series of photographs.

3.2 Results and discussion

3.2.1 Optical imaging

Optical imaging is the simplest method for monitoring the growth of flow instabilities, however porous media is not well adapted for optical imaging due to the often opaque nature of the packing material[26]. It is for this reason that Hele-Shaw cells have been so widely employed in order to visualise viscous fingers. While we have attempted to visualise several glycerol systems optically, it was found that only instabilities forming at the outer walls of the pack bed could be seen. For that reason only one optical time lapse series, for 60% glycerol, is shown here to demonstrate the limitations of the technique. In Figure 3.1 a time lapse series of photographs is shown.

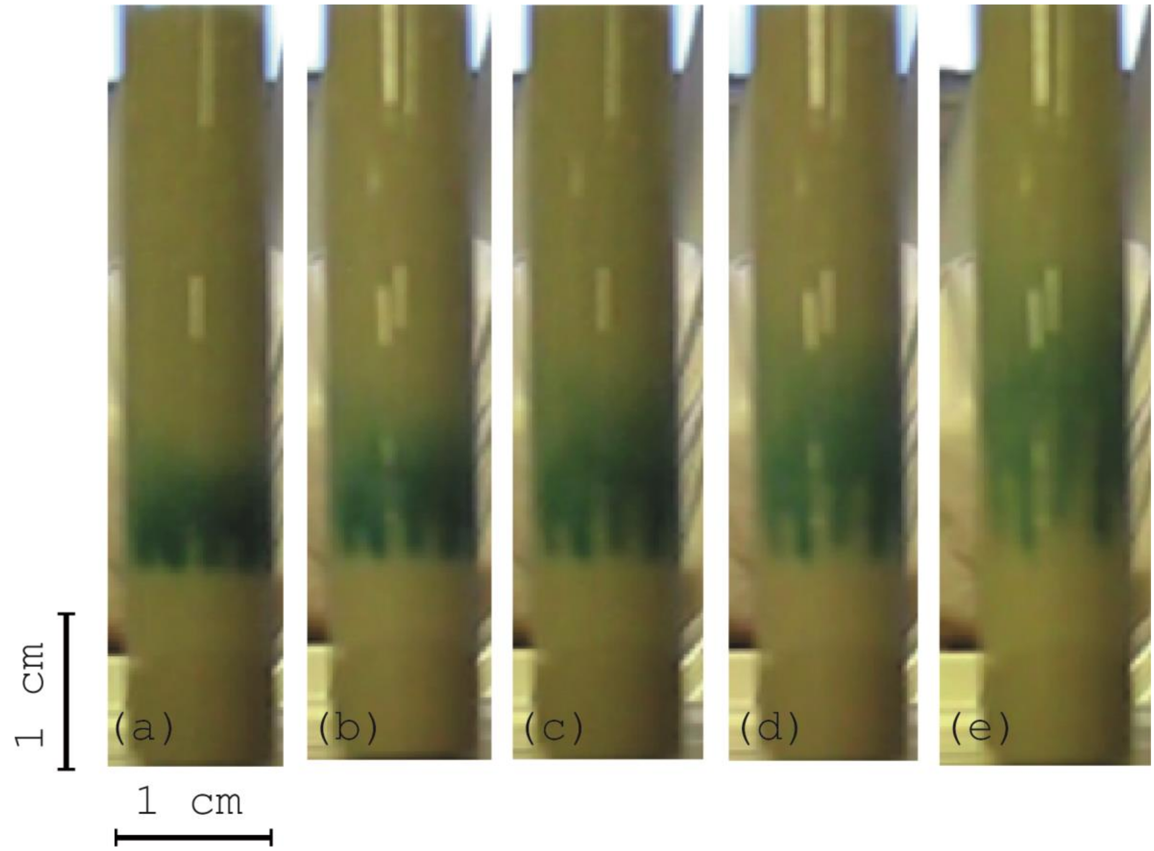

Figure 3.1: A times lapse series of photographs where a band of 60% glycerol is displaced by distilled water at a flow rate of 30 ml/hr through a packed bed reactor filled with sand.(a) = 0 s, (b) = 30 s, (c) = 60 s, (d) = 90 s and (e) = 120 s.

In Figure 3.1(a) the band of 60% glycerol is seen in the bottom third of the image. The glycerol appears blue due to the addition of blue food coloring. At the lower interface of the glycerol band three instabilities are beginning to develop. These instabilities have already started to develop because flow was applied from several seconds before the beginning of optical measurements. In Figure 3.1(b) the instabilities have grown in both length and width with the fingers moving upwards through the pack bed. This behavior is again seen in Figure 3.1(c). While the lower interface of the glycerol band is becoming unstable the upper interface is moving up through the pack bed and appears to have no instabilities forming. In Figure 3.1(d) the central finger accelerates ahead of the other two instabilities while all three instabilities continue to broaden. In Figure 3.1(e) it is now the finger on the right that appears to accelerate beyond the other two instabilities. While the formation of the instabilities at the outer edges of the pack bed can be visualized optically, no information is acquired about the flow behavior within the pack bed itself. It is not possible to say whether instabilities are forming through the center of the pack bed or provide any information regarding the growth structured development of fingers. While previously careful selection of solvents and the inclusion of an outer band of fluid within an appropriate refractive index has made the optical visualization of viscous fingers in a pack bed possible[15], here MRI has been utilized to image finger formation in a packed bed without the need of such complex experimental set-ups.

3.2.2 Gravitational effect

At 20°C glycerol has a density of 1.26 g/mL and water a density of 1 g/mL. This makes glycerol 26% denser than water and subsequently means that we cannot dismiss the effects of density fingering when carrying out viscous fingers experiments with glycerol. When carrying out investigations into viscous fingering between the glycerol and water in a horizontal bore magnet, Fernandez *et. al*[13] found some density effects over the short distance of a 1 cm diameter horizontal column. Regions of glycerol at the upper wall of the column were seen to slowly migrate downwards[13]. As a vertical bore magnet has been used for all these flow experiments it would be expected that density fingering would be more apparent[27]. It is known that a more dense fluid, such as glycerol, placed above a less dense fluid, such as water, under gravity will result in density fingering[12]. The first viable solution to this problem would be to reverse the arrangement of the system with regard to gravity. Placing the manganese sulphate solution above the glycerol and then applying flow from above would remove density issues, but in turn this can create further complications. With this arrangement gravity would be a stabilizing factor and therefore a critical velocity would be needed to bring about the occurrence of instabilities. Preliminary experiments in the lab found that a minimum flow rate of 40 mL/hr was required to produce a viscous fingering with this arrangement. MRI can be limited in its ability to acquire images in fast moving flow systems. Previous experimental investigations found that at higher flow rates the blurring of images affected the ability of MRI to provide fine detail about developing fingers[13]. For this reason it was believed to be rational to stay with the original setup and monitor the extent by which these density instabilities occur and so affect any experiments carried out. This seems preferable to introduce further problems to the system.

To determine the extent of density fingering a packed bed reactor, using sand as packing material, was filled with 20 mM manganese sulphate and a band of sand and 65% glycerol was created above this. As can be seen from

Figure 3.2 (a) the glycerol band, as shown by the high signal region, is a uniformly formed band in the upper region of the pack bed.

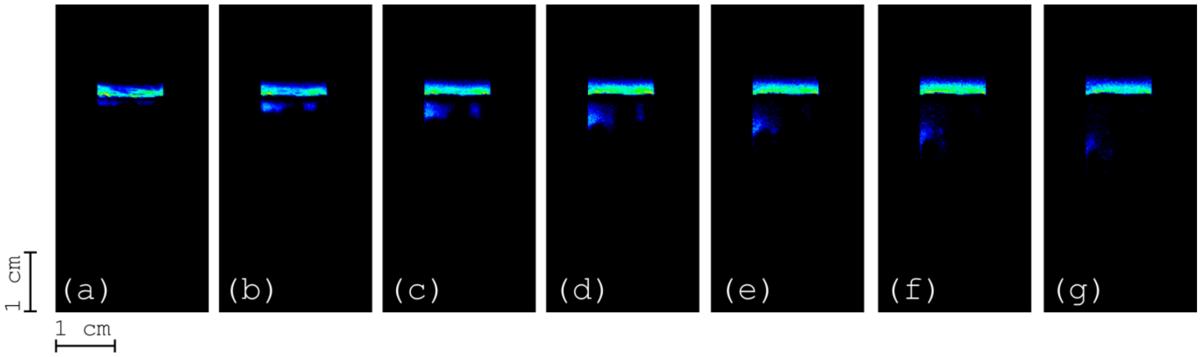

Figure 3.2: A time lapse series of MRI images showing the formation of density fingers with a field of view of 5 cm x 2.5 cm and a pixel array of 256 x 128 px. 60% Glycerol is shown by the high signal pixels and 20 mM manganese sulphate by the low signal pixels. The images are shown at 5 minute intervals.

The onset of density instabilities can be seen at the lower interface. These are able to develop before the first images acquired as it takes approximately 5 minutes to physically set up the apparatus and prepare the imaging sequence. In

Figure 3.2 (b) two density fingers are seen to move down from the initial glycerol band. In Figure 3.2 (c) the larger of the fingers, positioned to the left-hand side of the pack bed accelerates in front of the smaller finger seen on the right. In Figure 3.2 (d) the larger, dominating finger begins to split into two smaller fingers. This behavior continues in Figure 3.2 (e) with the larger, splitting finger now fully suppressing the growth of the smaller finger on the right. The finger on the left-hand side of the pack bed can now be seen to develop downwards through the packing material (Figure 3.2(f)). In Figure 3.2 (g) the band of glycerol still remains in the upper region of the pack bed. As the density finger dissipates through the pack bed the glycerol band appears relatively intact with little loss of volume and with no further instabilities appearing to form. This demonstrates that although density fingering does occur during the flow experiment, it can be considered as playing a secondary role to the dominating viscous fingers that will be presented. That said, this feature could not be dismissed and there should be an appreciation of its presence when assessing all viscous finger formations.

3.2.3 Viscous fingering as a function of flow rate

Numerous studies have demonstrated the influence of flow rate on viscous finger formation, both in Hele-Shaw cells[6, 23] and a real porous media[15, 28]. Broyles *et. al*[15] found, through optical visualization of a non-reactive system in a chromatography column, that as the flow rate was decreased the instabilities at the interface became less abundant and fingers that did develop had a larger wavelength. This behavior was also seen in a reactive system in the Hele-Shaw cell. Nagatsu *et. al* found that when a pre-existing viscosity gradient was present the addition of a chemical reaction at the interface did not alter this behavior[23, 29]. The inclusion of a chemical reaction did alter the structure and direction of the fingers, however with decreased flow rate fingers still became broader.

Using 60% glycerol a band of glycerol was again set up in a packed bed using 20 mM manganese sulphate as the driving fluid. In figure 3.3 a time series of images shows the viscous finger development in the fastest flow rate investigated, 30 ml/hr.

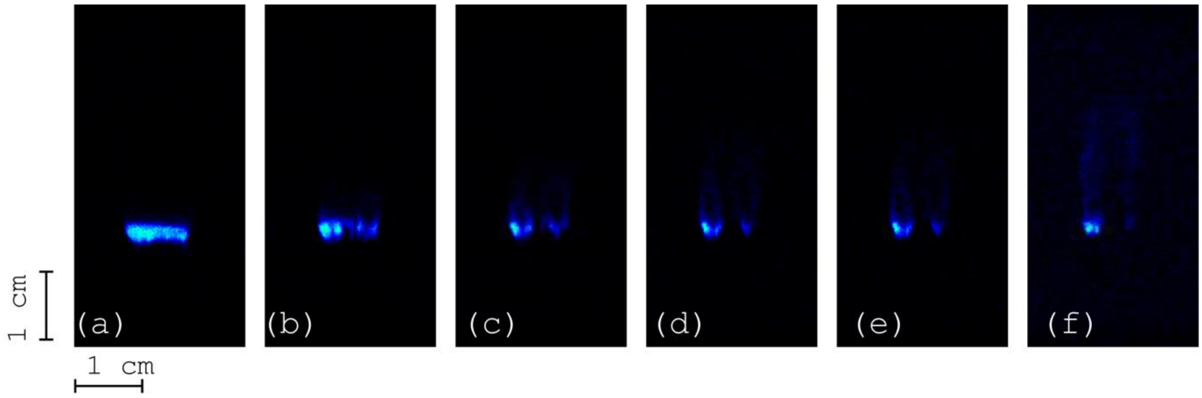

Figure 3.3: A times series of MRI images showing a band of 60% glycerol being driven through a packed bed by 20 mM manganese sulphate at 30 ml/hr. The field of view is 5 cm x 2.5 cm and a pixel array of 256 x 128 px. Images are shown at 1 minute intervals.

In Figure 3.3 (a) the high signal band of glycerol is visible in the bottom third of the image. The band is well formed, although the initial development of density fingers can be seen at the lower interface. In Figure 3.3

(b) the glycerol band begins to shift through the packed bed. Several instabilities are seen to develop at the lower interface. These instabilities do appear in the regions where density fingering was seen in the initial image. As viscous fingers are formed from perturbations in the interface, it would be expected that viscous fingers would form at the positions where density fingers have created perturbations in the interface. It can already be seen that a central finger begins to dominate over the other instabilities. In Figure 3.3 (c) the central finger has developed through the glycerol band reaching the upper interface. The finger then begins to spread, broadening and encompassing the finger to the right of it (Figure 3.3 (d)). In Figure 3.3 (e) this broadening of the central finger continues and the continued dispersion of the glycerol band through the pack bed is clear. In Figure 3.3 (f) the majority of the glycerol band is dispersed throughout the packed bed, however a small region of glycerol remains on the lower left-hand side of the image. This would agree with previous experiments that found, that at high flow rates small regions of the more viscous fluid were left behind as the instabilities formed[13, 14]. By lowering the flow rate it is expected that the fingers will become broader[15, 30]. Figure 3.4 shows a time series of images at a flow rate of 9 ml hr^{-1}.

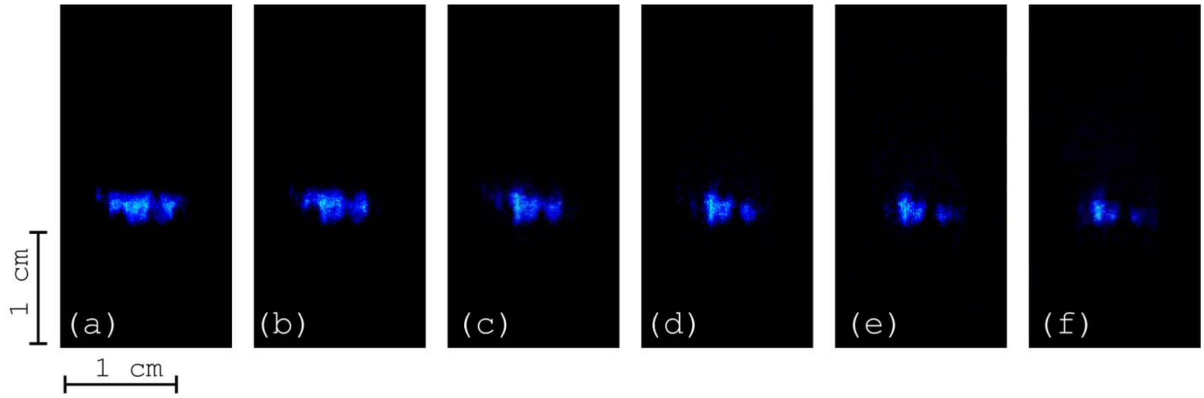

Figure 3.4: A times series of MRI images showing a band of 60% glycerol being driven through a packed bed by 20 mM manganese sulphate at 9 ml/hr. The field of view is 3 cm x 1.5 cm and a pixel array of 256 x 128 px. Images are shown at 1 minute intervals.

In Image 3.4 (a) perturbations are seen in the lower interface of the glycerol band. These can be attributed to the initial onset of flow but also the influence of density fingering in the system. In Figure 3.4(b and c) the finger on the left hand side and central finger develops through the band of glycerol breaching the upper interface. The upper interface of the glycerol band also begins to break as the glycerol disperses through the pack bed. In Figure 3.4(d) both fingers have reached the top interface of the glycerol band and continue to broaden over time: this is more apparent in the central finger seen in Figure 3.4(e and f). In the final image of the time sequence the majority of the glycerol band is dispersed. While it is true that the glycerol band disperses slower in the 9 ml hr^{-1} experiment than the 30 ml hr^{-1} experiment it is difficult to quantify the differences in the instabilities. The 9 ml hr^{-1} images show fewer, broader instabilities in the initial stages of the experiment, however apart from a greater proportion of the glycerol remaining in the final stages of the experiments is difficult to confirm any trend in finger development. To do this a third, slower flow rate was investigated. Figure 3.5 shows a time series of MRI images for a flow rate of 4 mL hr^{-1}. As with previous experiments the glycerol band can be seen in the bottom third of each image.

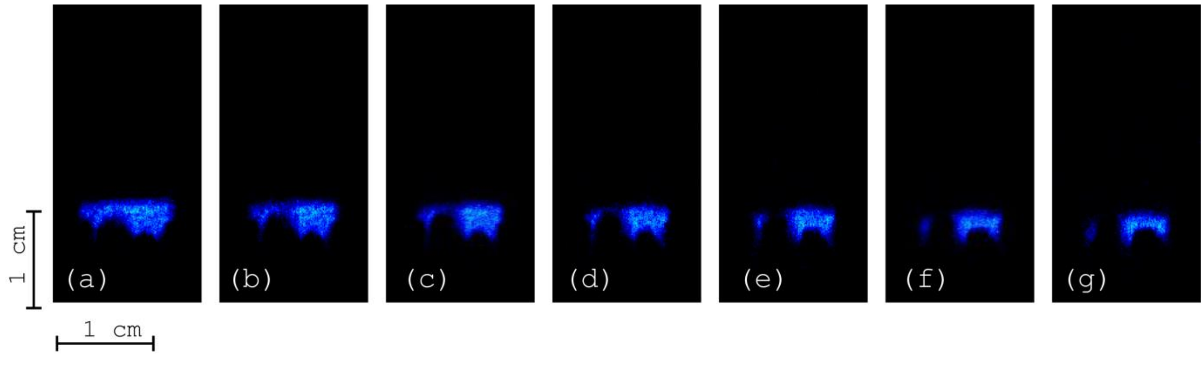

Figure 3.5: A times series of MRI images showing a band of 60% glycerol being driven through a packed bed by 20 mM manganese sulphate at 4 ml/hr. The field of view is 3 cm x 1.5 cm and a pixel array of 256 x 128 px. Images are shown at 1 minute intervals.

In these images it can be seen that the fingers that develop are much broader and only two distinct instabilities are seen to form. In Figure 3.5 (c) the finger developing on the left of the pack bed moves ahead of the second instability seen to the right-hand side. In Figure 3.5(d) the left, dominating finger moves further through the pack bed toward the upper interface while there is little progression of the second finger. This shows that the finger positioned on the left is shielding the second, smaller finger from developing. In Figure 3.5(e) the dominating finger has moved completely through the glycerol band and has shielded any forward movement of the second instability although some broadening of the finger is still seen. In images f and g no forward motion of the secondary finger is seen while the dominating finger continues to move through the glycerol band and spread. It is unclear whether the dominating finger undergoes any splitting due to the loss of contrast past the glycerol band. When analyzing all three flow rates together the data shows the reproduction of trends previously seen in the literature[10, 13, 28]. Decreasing the flow rate broadens the fingers that develop. Darcy's law shows that by lowering the flow rates the pressure gradient within the system reduces[26]. The lower the pressure gradient the fewer occurrences of instabilities there are. The reduced flow rates result in this drop in the pressure gradient and explain the decrease in finger formation and development. This dependence on flow rate has been found both here and in previous studies to be less pronounced as the flow rate increases[15]. This would explain why only small differences were seen between the 30 mL per hour and 9 mL per hour experiments while the instability development varied greatly between the 4 mL per hour and 9 mL per hour experiments.

While flow rate has been shown to be a controlling factor in the formation and development of viscous fingers it is not the only defining parameter. We have also investigated the influence of glycerol concentration and so viscosity on the development of instabilities.

3.2.4 Viscous fingering as a function of glycerol concentration

The viscosity of a fluid is defined as the fluid’s ability to resist flow[31]. As glycerol is diluted with water it becomes less viscous and the viscosity gradient within the system drops. Both experimental and theoretical studies have shown that as the viscosity of the displaced fluid increases the growth rate of fingers increases and fingers formed become narrower[8, 13, 14, 28, 32]. Therefore as the viscosity of the glycerol increases, fingers would be expected to develop from broad, slow-moving instabilities to well-defined fast-moving narrow fingers.

In Figure 3.6 a time series of images for 20% glycerol in water is shown. Several instabilities can be seen to form at the walls of the pack bed. This behavior was also seen by Fernandez *et. al* and attributed to slower flow at the walls which allows broader fingers to develop[14].

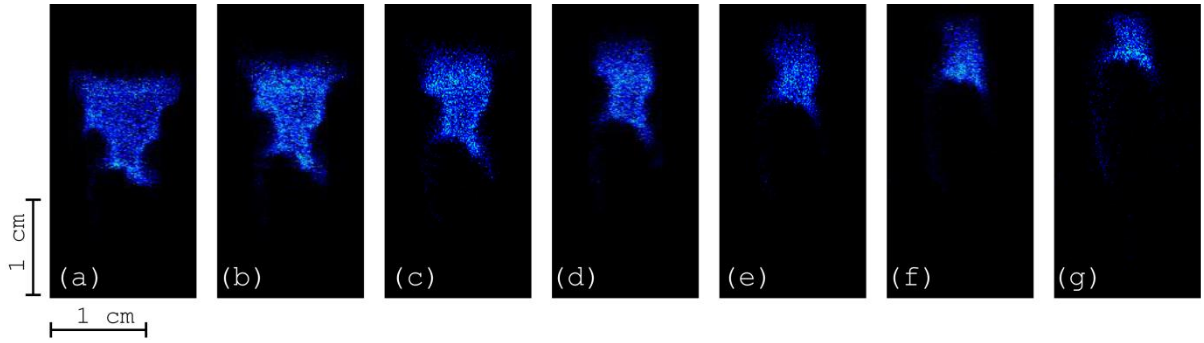

Figure 3.6: A times series of MRI images showing a band of 20% glycerol being driven through a packed bed by 20 mM manganese sulphate at 30 ml/hr. The field of view of 5 cm x 2.5 cm and a pixel array of 256 x 128 px. Images are shown at 1 minute intervals.

In Figure 3.6(b) the top of the glycerol band has moved forward through the pack bed. The fingers on the left and the right hand side of the image have broadened occupying a greater volume. In image (c) a central finger can be seen to develop. This finger is broad, almost spanning the width of the pack bed. The top interface of the glycerol band moves out of the visible region of the coil in figure 3.6 (d) while both the central and side fingers also move forward. Due to the broad nature of the fingers no finger splitting is seen. The fingers continue to broaden and show no splitting or shielding behavior until in Figure 3.6(e) where the glycerol band has almost been fully removed from the visible region. This occurrence of broad fingers with no splitting confirms what was previously seen with a low viscosity gradient. The pressure force is now too low to promote the development of well-formed fingers.

By increasing the concentration of the glycerol to 40% in water the viscosity is increased. In Figure 3.7 a time series of images for 40% glycerol is shown.

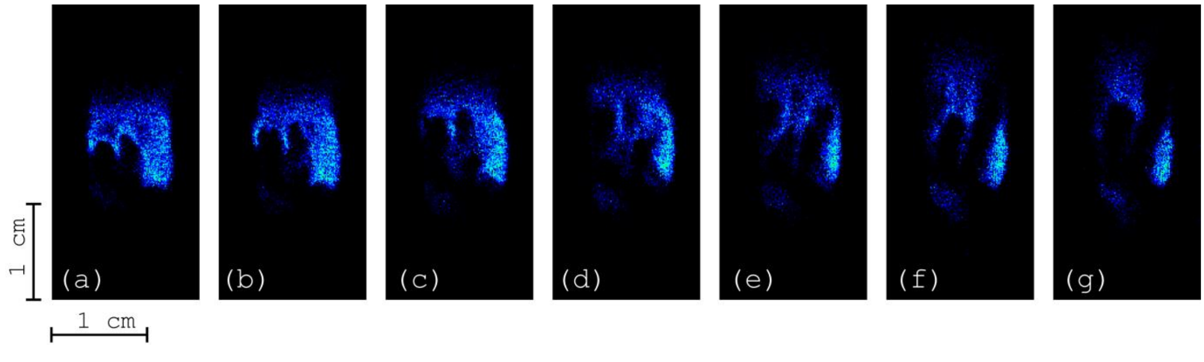

Figure 3.7: A times series of MRI images showing a band of 40% glycerol being driven through a packed bed by 20 mM manganese sulphate at 30 ml/hr. The third of 6 vertical slices is shown here. The field of view of 3 cm x 1.5 cm and a pixel array of 256 x 128 px. Images are shown at 1 minute intervals.

Two fingers form on the left hand side of the image in Figure 3.7(a). These fingers become more defined and progress towards the top of the glycerol band in Figure 3.7 (b). In image (c) several regions of low signal are seen with no obvious fingering structure connecting them to the original fingers. This alludes to the possible tortuous nature of fingers as they move through the pack bed. In Hele-Shaw cell experiments of both reactive and non-reactive systems viscous fingers showed torticity within the plane of the cell. In the environment of a real porous media the flow is not restricted to one-dimension, therefore the fingers are able to develop in all directions and can easily move between the image slices. In Figure 3.7(e) one dominating finger forms diagonally from the centre of the pack bed up towards the right-hand side of the image. This finger accelerates through the glycerol band with a second finger developing to the left of it (image f). In the final image of the time series (Figure 3.7(g)) the finger positioned on the left has moved through the glycerol band past the upper interface. Several regions of glycerol remain after the fingers have passed by. This low level displacement of the glycerol band is indicative of high amounts of fingering.

In Figure 3.8 a time series of both vertical and multiple horizontal slices are shown for 60% glycerol in glycerol.

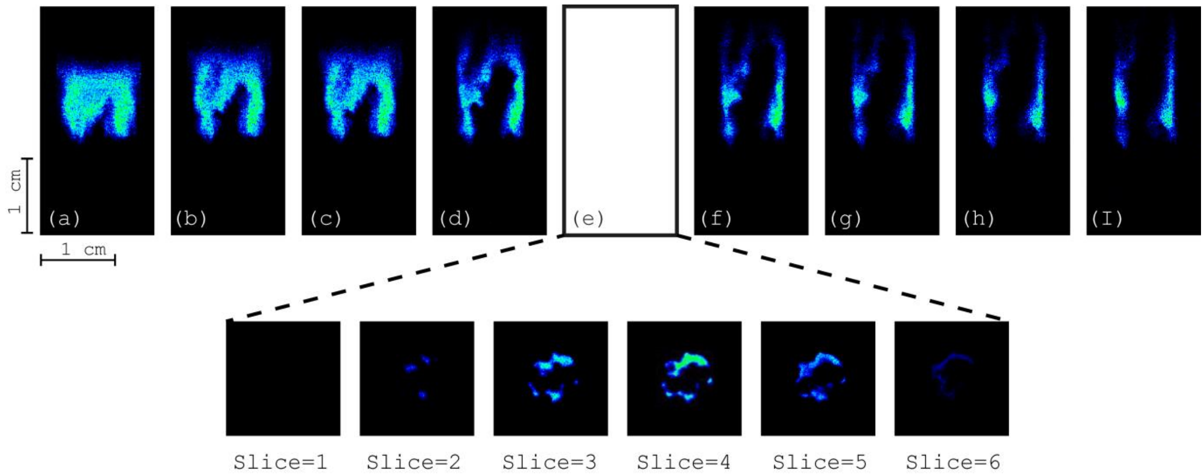

Slice=1 Slice=2 Slice=3 Slice=4 Slice=5 Slice=6

Figure 3.8: : A times series of MRI images showing a band of 60% glycerol being driven through a packed bed by 20 mM manganese sulphate at 30 ml/hr. The fifth of 6 vertical slices is shown here. The field of view of 3 cm x 1.5 cm and a pixel array of 256 x 128 px. Images are shown at 1 minute intervals. Image (e) is made up of 6 horizontal slices with a field of view of 1.5 x 1.5 cm and a pixel array of 128 x 128 px. The slices were separated by 1.5 mm.

In Figure 3.8(a) a finger is seen to develop in the centre of the glycerol band. This development of a finger is seen so early because the flow was applied fractionally before the first image was acquired. This finger begins to disperse, with a smaller finger developing from the left interface of the existing finger (Figure 3.8(b)). One well-defined finger dominates the system. Through images c to d smaller fingers are seen to develop from the left-hand side of the large finger. However all these smaller instabilities are shielded and shown no further growth. In Figure 3.8 the leading edge of the glycerol band breaks down with a density finger developing to the left of the image. This development of more defined density fingers is to be expected due to the increased concentration, and therefore density of the glycerol band. In Figure 3.8(e) six horizontal slices show the progression of the finger through the pack bed. Slice one shows no high signal regions owing to the complete displacement of glycerol by manganese sulphate solution. In slice two three small areas of high signal, from glycerol, are seen. As the finger has move through the center of the pack bed these regions of glycerol remain behind due to the non-uniform flow. The finger becomes narrower due to the reduced splitting and spreading towards the top of the finger. In slice 5 the finger continues to move through the packed bed, with the signal dying away in the final slice. In Figure 3.8(f) it can be seen that the signal is lost in the final of the horizontal slices because the finger has reached the upper interface of the glycerol band. Also the density finger has developed further down through the packed bed. In Figure 3.8(g) and (h) the finger spreads and the glycerol at the walls of the packed bed dissipate as the flow is focused through the finger. The increase in viscosity has resulted in a faster moving, narrower single finger that develops through the system.

In Figure 3.9 a time lapse series of images for 80% glycerol in water is seen. In Image (a) the glycerol band is well formed with the onset of an instability at the lower interface, to the right of the image.

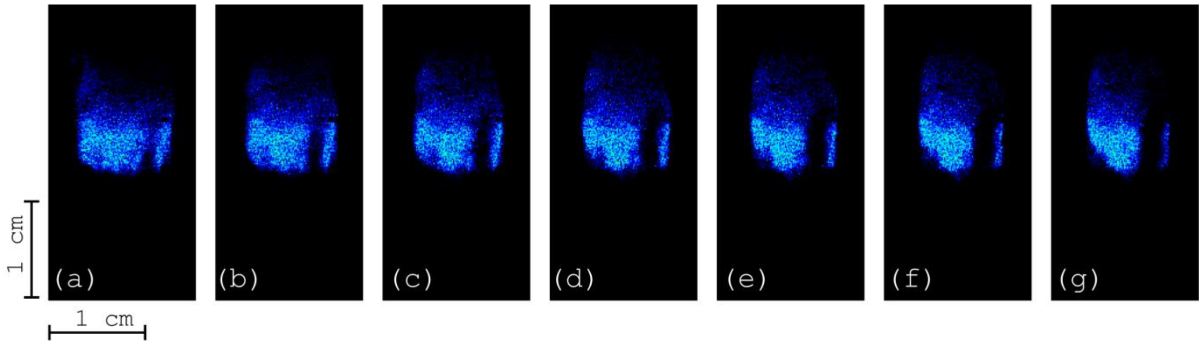

Figure 3.9: A times series of MRI images showing a band of 80% glycerol being driven through a packed bed by 20 mM manganese sulphate at 30 ml/hr. The third of 6 vertical slices is shown here. The field of view of 3 cm x 1.5 cm and a pixel array of 256 x 128 px. Images are shown at 1 minute intervals.

In image (b) the finger has moved forward through the glycerol band but shows little broadening as would be expected from a system with a high viscosity gradient. The finger is seen to broaden slightly in image (c) but not to the extent that has been seen in previous experiments. In Figure 3.9 (d) the finger reaches the leading edge of the glycerol band, but up until this point no splitting or shielding has been seen. In Figure 3.9(e) the initial development of a second finger is seen in the lower left of the glycerol band. This instability begins to broaden in image (f) but no splitting is seen from either of the instabilities and the width of both fingers is relatively short compared to the fingers seen in previous experiments. The finger can be said to be in a steady state, a type of finger previously studied by Saffman and Taylor, due to its consistent width and the lack of splitting that occurs[22].

By increasing the concentration and so the viscosity of glycerol we have seen the progression from broad slow moving fingers to narrow fingers that accelerate ahead of the flow of the bulk fluid. It has been found that the lower the viscosity the greater the degree of splitting and spreading seen within a system. As the pressure force increases, with increased viscosity it would be expected that a single finger dominates. This behaviour has been observed both here and in previous studies. This dominating finger supresses the growth of any other instabilities and leads to the steady state behaviour we have seen at higher glycerol concentrations.

We have been able to reproduce behaviour previously seen in porous media and Hele-Shaw cells with regards to the influence of flow rate and viscosity on instability formation. However, in several experiments we have seen image features that allude to the tortuous nature of the fingers when moving through a three dimensional porous media. In order to effectively analyse the images presented here the root mean square analysis technique introduced in the previous chapter is applied to this set of data.

3.2.5 Root mean square analysis of viscous fingering in glycerol

Experiments visualizing the effect of flow and viscosity on the development of viscous fingers through porous media were presented in the previous section of this chapter. Although attempts can be made to describe the instabilities that form, this analysis is mostly qualitative in nature and gives little concise structural information. Previous studies have used various techniques to classify results. Most commonly the width and length of the fingers have been reported, with their dependence on viscosity and initial flow rates studied[21, 33-35]. This presents a viable method for classifying instability formation when a finger is in steady state or a single finger formed in a Hele-Shaw cell. This method becomes difficult to apply when fingers move through a porous three dimensional medium. Other studies have attempted to plot the finger shape, such as tendril, fan and mushroom against a defining parameter, such as flow rate[6].

Here we apply the root mean square (RMS) analysis method used in chapter 2 of this thesis with several small alterations. All experiments were imaged in single or multiple two-dimensional slices, and we present only the RMS deviations of high signal pixels in the z and x direction. Over the course of the experiments it was found that there was no uniform bulk movement of the glycerol band through the packed bed, due to the occurrence of fingers in each experiment. For this reason a model glycerol band was constructed for each experiment using the dimensions of the experimental glycerol band. Each model was populated with Gaussian noise to simulate the noise created by the packing material in the experimental images. The RMS pixel position of each model was used for each corresponding experimental data set. Only pixels over a given intensity threshold, and classed as high signal pixels were plotted. The position of the pixels, classified as having high signal intensities, over a given intensity threshold is plotted as a deviation from the models RMS pixel position in mm. A reduction in signal within an image, due to the dispersion of glycerol or the development of fingers, appears in the RMS deviation plots as a reduced number of pixels at a specific distance. These troughs can therefore correspond to the formation of fingers.

3.2.5.1 Viscous fingering as a function of flow

In Figure 3.10 we present the RMS analysis for the displacement of glycerol at 30 ml/hr in the *z* and *x* direction.

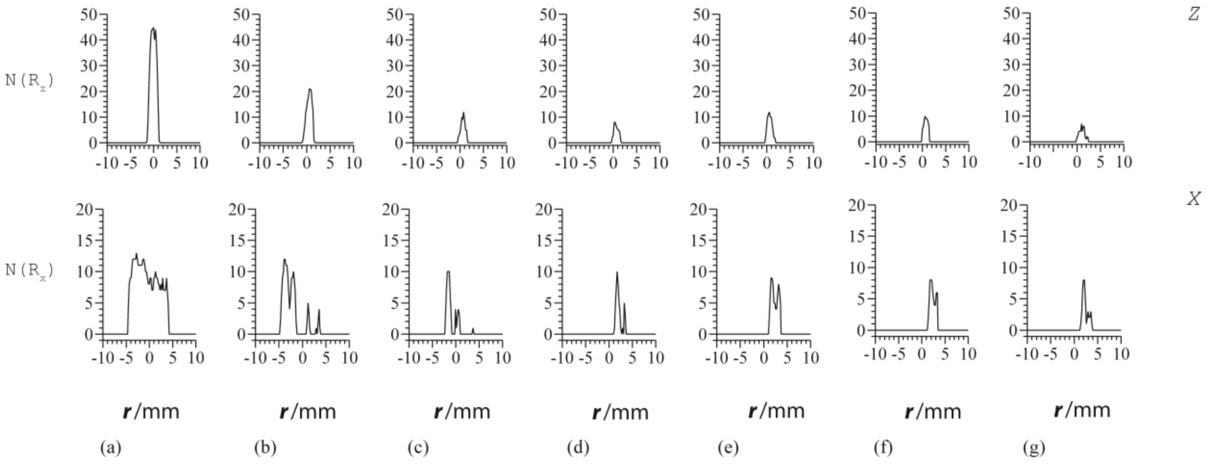

Figure 3.10: A Plot of Root Mean Square pixel deviations, r/mm, against the number of pixels, N(R), of a time lapse series of MR images of 60% glycerol being displaced at 30 ml/hr. Plots a to g are spaced 60 seconds apart. The time line of plots is for deviations along the z axais and the bottom line, deviations along the x axis.

In (a) the pixel deviations in the *z* direction, the direction of applied flow, show formation of a uniform band distributed around the model RMS pixel position, while the deviation along the *x* axis shows the slight loss of high intensity signals to the right of the image. This indicates the formation of a finger to the right hand side of the image. In (b) the overall number of pixels in both plots has decreased owing to the dispersion of glycerol through the packed bed. The z distribution is still relatively uniform. However it is slightly shifted towards a positive deviation, showing the forward motion of glycerol through the image. The *x* distribution, however, shows several troughs developing, with the main one being in the center of the deviation. From this it can be seen that a finger has formed through the center of the glycerol band. A narrower, second finger is formed to the right of this, and the onset of another instability to the left is indicated by the drop in the number of pixels at ~ -3 mm. The remaining plots for the *z* axis show little more than the reduction of signal intensity over the course of the experiment and the gradual shift of the glycerol band in the direction of flow. This indicates that there is no finger formation extending out through the packed bed. However it is important to note that with a glycerol band of volume 0.5 ml the distribution of pixels would only be expected over a small region in the *z* direction. The plots for the x direction, however, do provide further information on the development of fingers. In plot (c) the troughs have broadened and we can see that the two fingers seen on the right have almost completed merged indicating spreading of the fingers. The small instability previously seen on the left has now developed, indicated by the increased reduction of pixel numbers at a deviation of -1 mm. In plots (d to g) all pixels to the right have now disappeared showing that the initial fingers have spread. When referring back to Figure 3.3, the images provided are difficult to analysis without this method due to the high number of instabilities forming in a small area and the fast removal of glycerol, due to the high flow rate. The RMS analysis, however, has provided a clearer view of the system and enabled the evolution of fingers to be followed.

In

Figure 3.11 Figure 3.11 the same analysis has been carried out for images acquired at a flow rate of 9 ml/hr.

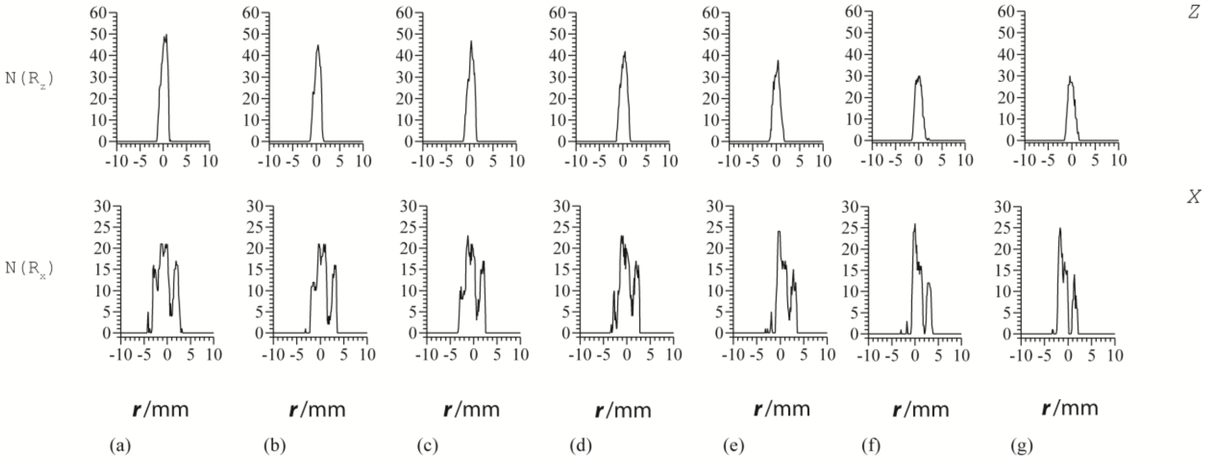

Figure 3.11: A Plot of Root Mean Square pixel deviations, r/mm, against the number of pixels, N(R), of a time lapse series of MR images of 60% glycerol being displaced at 9 ml/hr. Plots a to g are spaced 60 seconds apart. The time line of plots is for deviations along the z axis and the bottom line, deviations along the x axis.

In the *z* direction the deviations plotted do not show any defining feature that would allude to a high level of fingering. As with the previous experiment the number of pixels reduces over the course of the experiment as the glycerol disperses. Also there is a very small shift of the distribution to positive deviations, indicated by the small shift to the right of the top of each deviation plot. This indicated a small shift of the glycerol band, with the flow but no great amount of bulk movement is seen. The *x* deviation plots, however, do provide further information about the developing system. In plot (a) the distribution has several troughs, showing that several instabilities have initially formed. In Figure 3.4, several instabilities are seen at the lower interface of the glycerol band. In Figure 3.11 (b and c) the troughs at – 3 and + 2 mm become deeper, showing that the instabilities at these positions have grown in length. The continued loss of pixels at the – 3 mm position through the remaining plots shows the continued loss of signal from this region, and so the further growth of a finger at this position. As the reduction in pixel numbers is greatest at this point in plots e through to f it can be said that it is the dominate finger forming at – 3 mm. There is also continued development of the finger at + 2 mm, although no broadening of the trough is observed and so no spreading of the finger is witnessed.

In Figure 3.12 the RMS deviation plots for the flow experiment run at 4 ml/hr are shown.

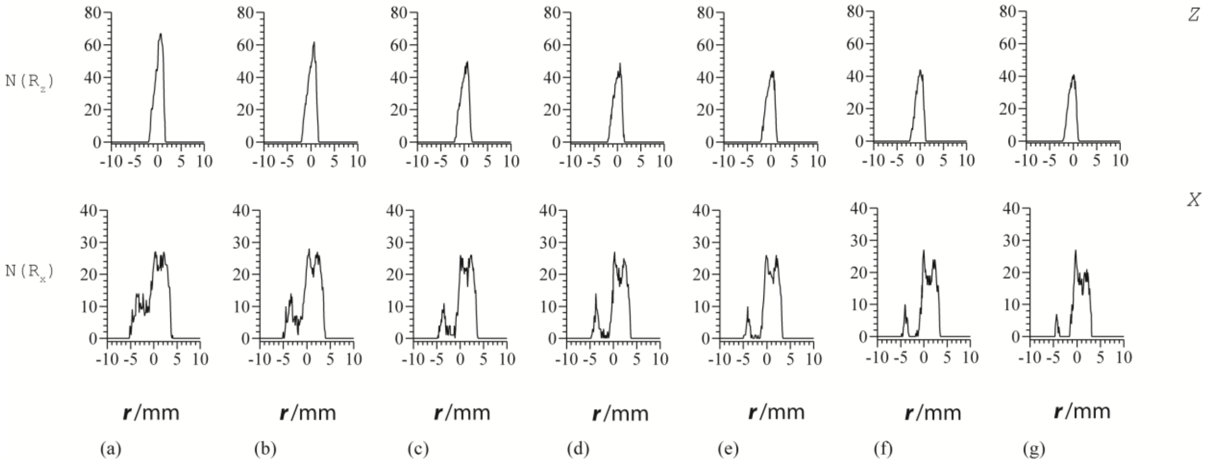

Figure 3.12: A Plot of Root Mean Square pixel deviations, r/ mm, against the number of pixels, N(R), of a time lapse series of MR images of 60% glycerol being displaced at 4 ml/hr. Plots a to g are spaced 60 seconds apart. The time line of plots is for deviations along the z axais and the bottom line, deviations along the x axis.

Again no distinct features, with regard to finger formation can be seen in the *z* plots, however a feature that has not previously been seen is apparent. Flow is applied in the +*z* direction and any shift in pixel distribution would be expected to be positive. In this case the pixel distributions along the *z* axis do not centre around 0 but are shifted slightly towards the negative deviations. This could indicate a small movement of the glycerol band downwards through the packed bed due to the effects of gravity and the inability of a slow flow rate to counteract this. The plots in the x direction provide a more detailed picture of the flow occurring in the system. In plot (a) the reduction in pixel numbers, between -5 and -1 mm, shows the development of a broad finger. A second trough is seen at +1 to +2 mm. This trough is not as wide at the one on the left of the plot, indicating a small, narrower finger. In plot (b) both of these troughs deepen and broaden. This shows the growth in length and the spreading of the fingers. This trend continues through the remaining *x* plots, however it is important to note that the instability at +2 mm does not broaden or grow in length by a great amount compared to the other finger. This shows that through the RMS deviation plots, it is possible to determine the presence of a dominating finger and whether it is influencing the growth a second instability through shielding.

These three set of RMS deviation plots have shown the distribution of high signal pixels in MR images as a function of flow rate. It has been previously stated that as the flow rate is increased, narrower and longer fingers develop[12, 33]. We are able to confirm this by analysing the position and width of troughs in the RMS deviation plots. As with the images, whilst it is difficult to differentiate greatly between the two faster flow rates, we are now able to show that more instability formation does occur at the highest flow rate and confirm that instabilities broaden as the flow rate is decreased.

3.2.5.2 Viscous fingering as a function of glycerol concentration

The RMS analysis technique is now applied to the MR images acquired when investigating the viscous fingering as the concentration and so the viscosity of glycerol is increased. To prevent repetition only the RMS plots for 40% and 80% glycerol in water are shown. These two experiments have been chosen because they show good representation of the features seen at higher and lower concentrations.

In Figure 3.13 the RMS deviation plots are shown for a flow experiment run at 30 ml/hr with a glycerol concentration of 40%.

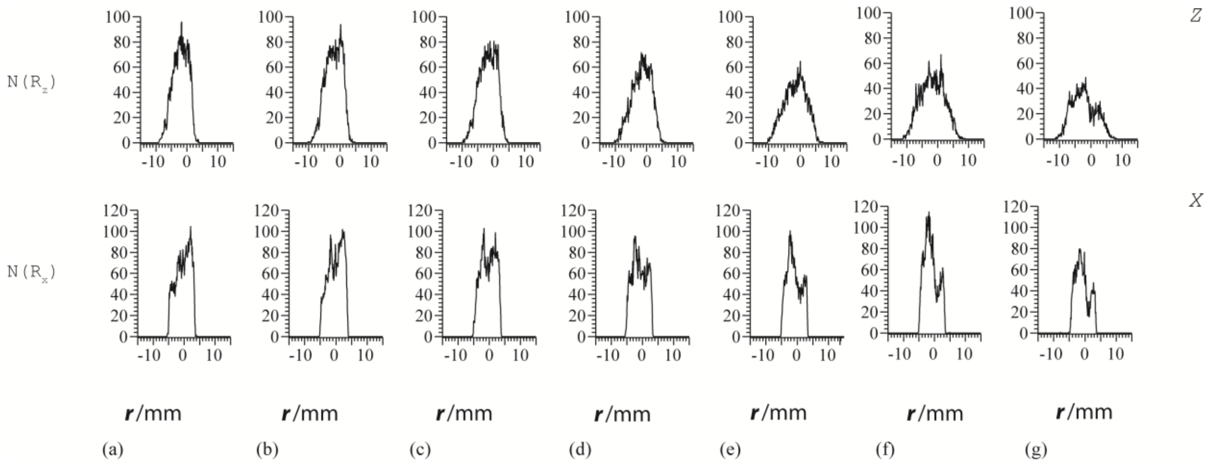

Figure 3.13: A Plot of Root Mean Square pixel deviations, r/mm, against the number of pixels, N(R), of a time lapse series of MR images of 40% glycerol being displaced at 30 ml/hr. Plots a to g are spaced 60 seconds apart. The time line of plots is for deviations along the z axis and the bottom line, deviations along the x axis.

All of the distributions are broader in the *z* direction because a wider band of glycerol was used in these experiments, and again a reduction in the number of pixels is seen over time. The right hand side of the z distribution in plot (a) drops off towards zero abruptly, indicating that the upper interface of the glycerol band is flat. This side begins to slope in plot (d) and the gradient of this slope increases in the following plots. This indicates the breakdown of the upper glycerol interface over the period of the experiment. What causes this interface breakdown can be seen in the *x* plots for this experiment. In plot (a) the *x* plot indicates the presence of instability formation from -5 to +2 mm deviation. When referring to Figure 3.7 a broad finger that has begun to undergo splitting is seen on the left of the image. The RMS plot shows the presence of this finger, but the splitting is not yet defined enough to appear in the RMS plot. In plot (c) the development of two troughs at -3 and +1 mm deviations indicates the splitting of the initial instability and the development of two separate fingers. These troughs are seen to broaden and deepen as the experiment continues, plots (d to g) showing the broadening and increase in length of the fingers.

In Figure 3.14 the RMS deviation plots are shown for a flow experiment run at 30 ml/hr with a glycerol concentration of 80%.

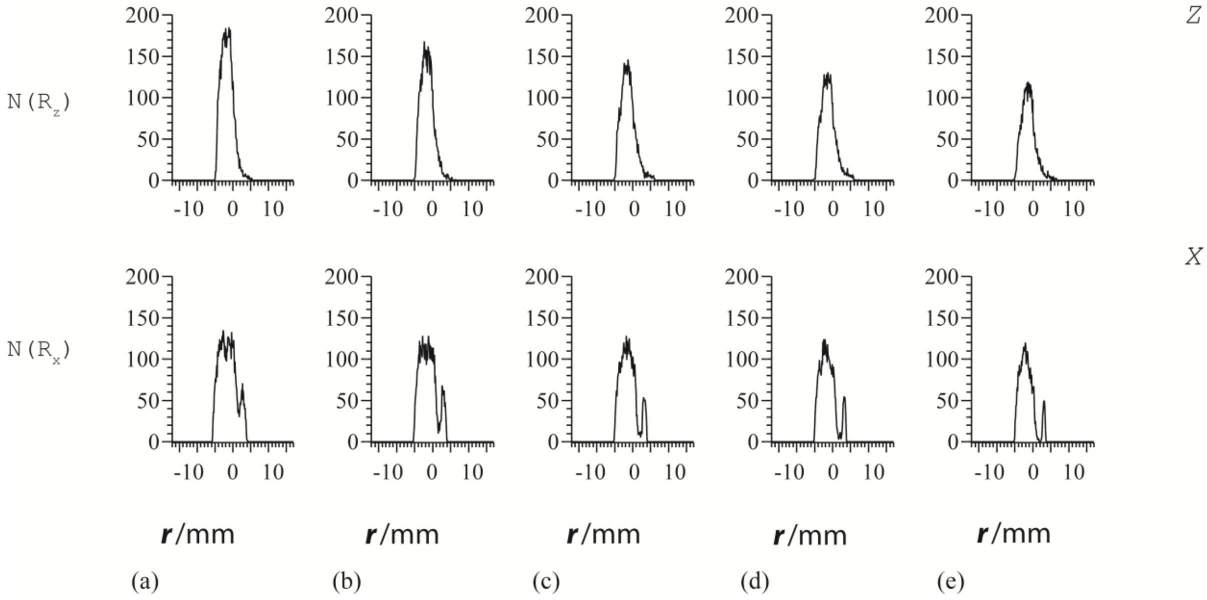

Figure 3.14: A Plot of Root Mean Square pixel deviations, r/mm, against the number of pixels, N(R), of a time lapse series of MR images of 80% glycerol being displaced at 30 ml/hr. Plots a to g are spaced 60 seconds apart. The time line of plots is for deviations along the z axis and the bottom line, deviations along the x axis.

At a higher glycerol concentration and so a higher viscosity, stable and narrow, longer fingers would be expected. The *z* deviation plots again show the reduction in glycerol over time. The distributions tail off on the right hand side due to the non-uniform structure of the top of the glycerol band shown in Figure 3.9. The upper interface of the glycerol band does not form a flat interface due to the increased density caused by a 80% glycerol solution. It is these perturbations in the upper region of the glycerol band that create these trailing edges in the z RMS deviation plots. The RMS deviation plots for the *x* direction clearly show the formation and development of a single, steady state finger. The trough which develops in plot (a) at +2 mm deepens through the course of the experiment, with a slight broadening seen. In plot (a) small perturbations are seen at -3 mm but by plot (c) these have been smoothed out. This can be attributed to shielding of any small fingers due to the presence of the larger dominating finger.

In the lower viscosity system features such as splitting and spreading are all seen. These features however do not dominate in the high viscosity system, where a steady state finger develops and dominates the flow through the packed bed.

The previous study carried out by Bacri *et al.* discussed the formation of fingers between water and glycerol solutions through a variety of porous media[36]. Acoustic techniques were used to obtain concentration profiles throughout the porous media and identify the formation of fingers. This study identified the formation of fingers which developed linearly with time, enabling calculation of a linear velocity, for each instability formed. In the original studies by Saffman and Taylor[33] this linear relationship was also described and referred to the instability reaching a steady state. We have seen that the fingers do not necessarily develop linearly with time. In figure 3.7 the fingers can be seen to move in and out of the horizontal slice displayed. This demonstrates that the fingers can take a more tortuous path through packed bed. Any linear velocity calculated for instabilities which develop would be not fully account for these tortuous pathways and lead to possible misinterpretation of the finger formation. It is important to note however that the conditions under which our experiments were carried out vary greatly from those in the study by Bacri *et al.* Porosity, flow rates and viscosity of the fluids used all varied between the two studies, and as was seen in the introduction to this thesis all these factors greatly affect the formation of instabilities and the way in which they develop. By adjusting the experimental setup in future experiments it would be possible to reproduce the experiments carried out by Bacri *et al.* while using MRI as the imaging technique. This could well lead to greater understanding as to how this linear relationship between finger development and time can be used to interpret finger formation as well as understand in more detail how finger velocities can be used to identify fingers when they are or are not in the steady state.

3.3 Conclusion

We have used MR imaging to investigate the relationships between finger formation and viscosity and flow rate. We were able to confirm the trends previously seen in the literature with either increased flow rate or viscosity, both producing narrower, faster moving fingers that were less prone to splitting[13, 23]. The use of the RMS deviation analysis has provided further insight into the development of these instabilities and has been used to define features seen in the image sequences.

3.4 References

1. Almarcha, C., et al., *Convective Mixing Induced by Acid-Base Reactions.* Journal of Physical Chemistry B. **115**(32): p. 9739-9744.
2. Almarcha, C., et al., *Active Role of a Color Indicator in Buoyancy-Driven Instabilities of Chemical Fronts.* Journal of Physical Chemistry Letters. **1**(4): p. 752-757.
3. Gerard, T. and A. De Wit, *Miscible viscous fingering induced by a simple A plus B -> C chemical reaction.* Physical Review E, 2009. **79**(1): p. 10.
4. Hejazi, S.H., et al., *Viscous fingering of a miscible reactive A plus B -> C interface: a linear stability analysis.* Journal of Fluid Mechanics, 2010. **652**: p. 501-528.
5. Nagatsu, Y. and A. De Wit, *Viscous fingering of a miscible reactive A+B -> C interface for an infinitely fast chemical reaction: Nonlinear simulations.* Physics of Fluids. **23**(4): p. 13.
6. Podgorski, T., et al., *Fingering instabilities of a reactive micellar interface.* Physical Review E, 2007. **76**(1): p. 016202.
7. Casademunt, J. and F.X. Magdaleno, *Dynamics and selection of fingering patterns. Recent developments in the Saffman-Taylor problem.* Physics Reports-Review Section of Physics Letters, 2000. **337**(1-2): p. 1-35.

8. De Wit, A., Y. Bertho, and M. Martin, *Viscous fingering of miscible slices.* Physics of Fluids, 2005. **17**(5): p. 054114.
9. Holloway, K.E. and J.R. de Bruyn, *Numerical simulations of a viscous-fingering instability in a fluid with a temperature-dependent viscosity.* Canadian Journal of Physics, 2006. **84**(4): p. 273-287.
10. Norton, T.T. and E.J. Fernandez, *Viscous fingering in size exclusion chromatography: Insights from numerical simulation.* Industrial & Engineering Chemistry Research, 1996. **35**(7): p. 2460-2468.
11. Shalliker, R.A., V. Wong, and G. Guiochon, *Reproducibility of the finger pattern in viscous fingering.* Journal of Chromatography A, 2007. **1161**(1-2): p. 121-131.
12. Hill, S., *CHANNELLING IN PACKED COLUMNS.* Chemical Engineering Science, 1952. **1**(6): p. 247-253.
13. Plante, L.D., P.M. Romano, and E.J. Fernandez, *Viscous Fingering In Chromatography Visualized Via Magnetic-Resonance-Imaging.* Chemical Engineering Science, 1994. **49**(14): p. 2229-2241.
14. Fernandez, E.J., et al., *The Effects Of Permeability Heterogeneity On Miscible Viscous Fingering - A 3-Dimensional Magnetic-Resonance-Imaging Analysis.* Physics Of Fluids, 1995. **7**(3): p. 468-477.
15. Broyles, B.S., et al., *Visualization of viscous fingering in chromatographic columns.* Journal of Chromatography A, 1998. **822**(2): p. 173-187.
16. Fernandez, E.J., et al., *A column design for reducing viscous fingering in size exclusion chromatography.* Biotechnology Progress, 1996. **12**(4): p. 480-487.
17. Yuan, Q.S., et al., *Flow distribution in chromatographic columns.* Journal of Chromatography A, 1999. **831**(2): p. 149-165.
18. Shalliker, R.A., B.S. Broyles, and G. Guiochon, *Visualization of viscous fingering in high-performance liquid chromatographic columns - Influence of the header design.* Journal of Chromatography A, 1999. **865**(1-2): p. 73-82.
19. Alvarez-Lacalle, E., J. Ortin, and J. Casademunt, *Low viscosity contrast fingering in a rotating Hele-Shaw cell.* Physics of Fluids, 2004. **16**(4): p. 908-924.
20. Degregoria, A.J. and L.W. Schwartz, *A Boundary-integral Method For 2-phase Displacement In Hele-shaw Cells.* Journal of Fluid Mechanics, 1986. **164**: p. 383-400.
21. Maxworthy, T., *Experimental study of interface instability in a Hele-Shaw cell.* Physical Review A, 1989. **39**(11): p. 5863-5866.

22. Saffman, P.G. and G. Taylor, *The Penetration of a Fluid into a Porous Medium or Hele-Shaw Cell Containing a More Viscous Liquid.* Proceedings of the Royal Society of London Series a-Mathematical and Physical Sciences, 1958. **245**(1242): p. 312-329.
23. Nagatsu, Y., et al., *Miscible viscous fingering with a chemical reaction involving precipitation.* Physical Review E, 2008. **77**(6): p. 067302.
24. *www.magritek.com*.
25. Hennig, J., A. Nauerth, and H. Friedburg, *Rare Imaging - a Fast Imaging Method for Clinical Mr.* Magnetic Resonance in Medicine, 1986. **3**(6): p. 823-833.
26. Homsy, G.M., *Viscous Fingering in Porous Media.* Annual Review of Fluid Mechanics, 1987. **19**(1): p. 271-311.
27. Read, K.I., *Experimental investigation of turbulent mixing by Rayleigh-Taylor instability.* Physica D: Nonlinear Phenomena, 1984. **12**(1–3): p. 45-58.
28. Dickson, M.L., T.T. Norton, and E.J. Fernandez, *Chemical imaging of multicomponent viscous fingering in chromatography.* Aiche Journal, 1997. **43**(2): p. 409-418.
29. Nagatsu, Y., et al., *Experimental evidence of reaction-driven miscible viscous fingering.* Phys. Rev. E, 2012. **85**(1): p. 015304.
30. Arneodo, A., et al., *UNCOVERING THE ANALYTICAL SAFFMAN-TAYLOR FINGER IN UNSTABLE VISCOUS FINGERING AND DIFFUSION-LIMITED AGGREGATION.* Physical Review Letters, 1989. **63**(9): p. 984-987.
31. Jim W Goodwin, R.W.H., *Rheology for chemists* 2008: The royal society of chemists.
32. De Wit, A., *Fingering of chemical fronts in porous media.* Physical Review Letters, 2001. **87**(5): p. 4.
33. Saffman, P.G. and G. Taylor, *The Penetration of a Fluid into a Porous Medium or Hele-Shaw Cell Containing a More Viscous Liquid.* Proceedings of the Royal Society of London. Series A, Mathematical and Physical Sciences, 1958. **245**(1242): p. 312-329.
34. De Wit, A., *Miscible density fingering of chemical fronts in porous media: Nonlinear simulations.* Physics of Fluids, 2004. **16**(1): p. 163-175.
35. Hooper, A.P. and W.G.C. Boyd, *Shear-flow instability at the interface between two viscous fluids.* Journal of Fluid Mechanics, 1983. **128**: p. 507-528.
36. Bacri, J.C., D. Salin, and R. Woumeni, *3-Dimensional Miscible Viscous Fingering in Porous-Media.* Physical Review Letters, 1991. **67**(15): p. 2005-2008.

4 Precipitate Forming Reactive Interface

All previous work in this thesis has focused on the effect of viscosity within a flow system. The viscosity gradient has either already been present in the system[1] or created by the addition of a chemical reaction at the interface between two solutions[2]. Here we investigate a reactive system with a pre-existing viscosity gradient, which remains unchanged throughout the experiment. Nagatsu *et. al* previously investigated the effect of precipitate deposition at the interface between two fluids in a Hele-shaw cell[3]. The chemical reaction shown in eq 4.1 was included in the displacement of glycerol by water.

$$Fe^{3+}(NO_3)_3 + K_4[Fe^{2+}(CN)_6] \rightarrow KFe^{3+}[Fe^{2+}(CN)_6] + 3KNO_3 \qquad 4.1$$

The development of fingers was found to alter with the inclusion of this precipitate forming reaction, however, previous studies have found that it is not the chemical reaction which influences finger formation but the formation of the precipitate in the porous media[4, 5]. Fingers that developed when a precipitate was formed had a more jagged structure, with fingers quickly changing their direction of growth due to a build-up of precipitate preventing flow in a specific direction. It was found that there was a dependence of finger structure on flow rate as well as initial reactant concentration. Unlike the reaction studied by Podgorski *et. al*, which created a viscosity change at the interface[2], the reaction did not change the growth behavior of the fingers with regards to flow rate[3]. As the flow rate was increased the fingers became narrower and faster moving. This agrees with previous work in non-reactive systems[1, 6, 7] and agrees with Darcy’s law, which states that an increased flow rate contributes positively towards the pressure force of the system[8]. An increased pressure force encourages the growth of long, narrow fingers. The deposition of precipitate decreases the permeability of the system, whether it be a Hele-Shaw cell or a 3-dimensional porous media.

By using eq 4.2[9] the effect of decreased permeability can be calculated, where the change in pressure, δp, is dependent on velocity, U, the viscosity of the fluids, μ, the permeability of the medium, k, the density of fluid, ρ, and gravity, $\mathbf{g}$. p_1 is the pressure of the displaced fluid and p_2 the pressure of the driving fluid.

$$\boldsymbol{\delta p = p_2 - p_1 = \left[\frac{(\mu_1-\mu_2)U}{K} + (\rho_2-\rho_1)g\right]\delta x} \qquad 4.2$$

Decreasing the permeability of the system increases the impact of a destabilizing viscosity gradient and therefore contributes to a greater pressure. As a positive pressure results in any perturbation at the interface developing into a finger[10], decreasing the permeability of the system increases the occurrence of fingers.

In this chapter we present optical and MR images that investigate the effect of flow rate on this reactive system in a packed bed reactor. We also demonstrate the possible difficulties that manifest when investigating this reactive interface using MRI.

4.1 Experimental procedure

4.1.1 Materials

A glass tube 80 cm in length with a 11 mm inner diameter where used to construct all packed bed reactors. For all flow experiments borosilicate glass beads (Sigma) of diameter 1 mm were used as the packing material. The packing material was rinsed with concentrated nitric acid and then distilled water to remove any paramagnetic species. All packing was dried in an oven at 80°C and then allowed to cool to room temperature before use. Iron (III) nitrate (Sigma-Aldrich ≥ 98%), 0.001 M - 0.01 M, and potassium hexacyanoferrate(II) (Sigma-Aldrich ≥ 99%) 0.01 to 0.09 M, in 50% glycerol (Sigma-Aldrich ≥ 99%) were prepared using deionized water. These solutions were used for both relaxation measurements and imaging experiments.

4.1.2 Optical imaging

The experimental setup used in all MRI experiments was used to optically investigate the formation of viscous fingers. A Canon A550 7.1 megapixel camera was used to acquire digital photographs of flow experiments run at a variety of flow rates.

4.1.3 Packed bed setup

Optical measurements were performed using a packed bed filled with 1 mm borosilicate glass beads, of length 30cms and inner diameter of 11 mm where flow was applied from above using a syringe pump (Harvard pump 22). MRI measurements were performed using a packed bed reactor, (Figure 4.1) 55 cm in length, with and inner diameter of 11 mm, filled with 1 mm borosilicate glass beads. Instead of being connected to a pump, a Teflon tap was connected to the outlet at the bottom. Flow was applied by opening the tap and allowing the fluid to flow under gravity. For both these experimental set-ups the more viscous fluid was placed at the bottom of the pack bed with a less viscous fluid positioned above.

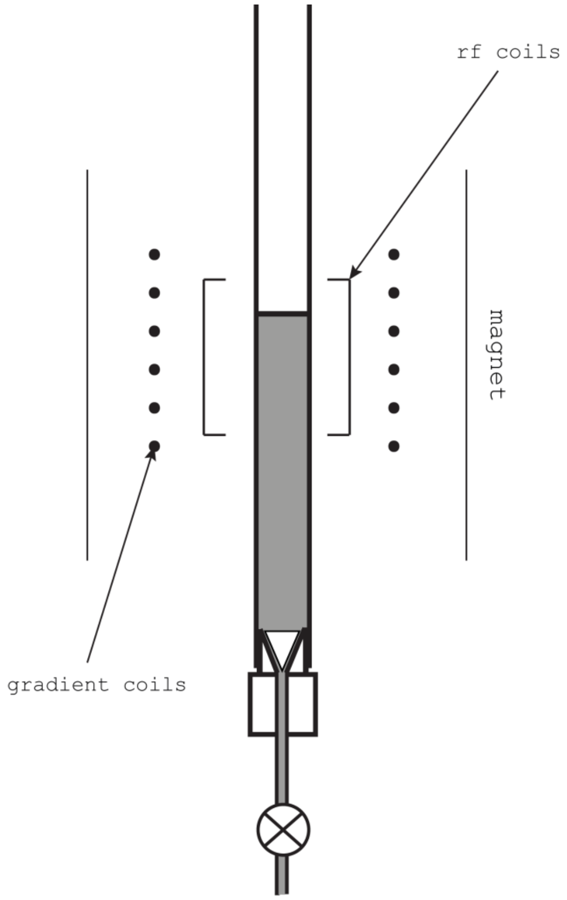

Figure 4.1: A schematic showing the experimental setup of a packed bed reactor with respect to the magnet. The interface between the two solutions is positioned in the bottom third of the rf coil.

4.1.3.1 Optical imaging

All optical images were taken using A Canon A550 7.1 megapixel camera. A Time series of photographs were recorded at a 10 sec interval. All optical images underwent post treatment in adobe Photoshop CS4. Images were converted to black and white and a red filter applied to improve image contrast. All images were cropped to remove all areas apart from the packed bed.

4.1.4 Nuclear magnetic spectroscopy

All magnetic resonance (MR) experiments were acquired using a Bruker DMX 300 spectrometer, operating at a ^{1}H resonance frequency of 300.13 MHz. A 25 mm radiofrequency resonator was used for all spectroscopy experiments. Data was acquired using XWIN-NMR 2.6 software. Measurements were carried out in a 5 mm NMR tube. All samples were allowed to equilibrate to the temperature inside the magnet bore, 290.8 ± 0.4 K, for 30 minutes before any measurements were acquired. T_1 relaxation measurements were made for Iron (III) nitrate solutions ranging in concentration from 0.001 to 0.01 M and potassium hexacyanoferrate(II), ranging in concentration from 0.01 to 0.09 M, in 50% glycerol solutions. This was done using inversion recovery experiments to measure the spin-lattice, T_1, using 16 experiments with IR delays logarithmically spaced between 5 μs and 15 s. 90° and 180° rf pulses were 45.5 and 91 μs respectively at an attenuation of 0 db. A spectral width of 10 KHz was used with 4 signal averages, each acquiring 16k complex points. Carr-Purcell-Meiboom-Gill (CPMG)[11] experiments were performed to measure the T_2 time for the solutions, acquiring a maximum of 512 echoes with an echo spacing of 10 ms. All T_1 and T_2 relaxation measurements were acquired through analysis carried out in Prospa NMR analysis software[12].

4.1.5 Magnetic resonance imaging

All magnetic resonance imaging was carried out using PARAVISION 2.1.1 software. A 25 mm radiofrequency resonator with an observable region of 2.5 cm x 4 cm was used for all imaging experiments. Two dimensional, multiple slice, horizontal images were acquired using the fast spin-echo imaging technique RARE[13], with a field of view of 20 mm × 20 mm and a pixel array of 128 (y) ×128 (x), respectively with 6 slices along the length of the packed bed. Slices were 1mm thick with an inter-slice distance of 4 mm. The spectral width was 50 KHz and a RARE factor of 64 was used, with T_R = 1101 s, giving an effective echo time of T_{eff} = 165 ms. This resulted in high signal intensity (SI) for the water peak in the potassium hexacyanoferrate(II) and 50% glycerol solution and low SI for the water peak iron(III) nitrate. The time resolution between images was 10 s. All images were analysed using prospa NMR anaylysis software.

4.2 Results and discussion

4.2.1 Optical Imaging

4.2.1.1 Gravitational fingering

Numerous studies have shown that when a more dense fluid is placed above a less dense fluid, density fingers develop[1, 14, 15]. Through MR imaging we demonstrated the development of such fingers in a packed bed reactor when 60% glycerol is placed above a 20 mM manganese sulphate solution. With the formation of precipitate at the interface and so the decreasing in porosity, gravitational finger would be expected to occur to a greater extent[14].

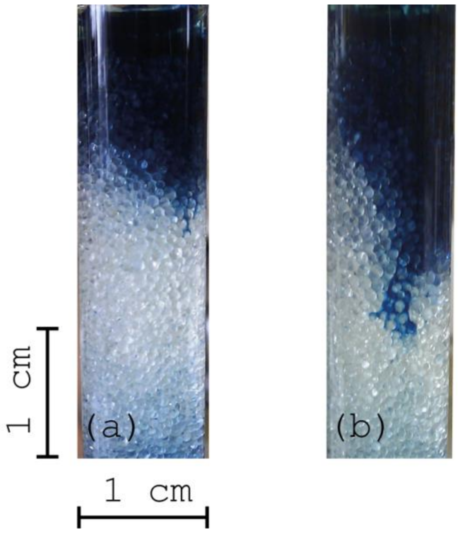

Figure 4.2: optical images of gravitational fingering between 0.03 M of potassium hexacyanoferrate in a 25% glycerol solution and 0.03 M solution of iron nitrate.

To investigate the effect this may have on experiments carried out under flow, a packed bed in which a 0.03 M solution of potassium hexacyanoferrate and 25% glycerol was pipetted on top of a 0.03 M solution of iron nitrate. In this experiment no flow was applied. Figure 4.2 shows two photographs of this packed bed, separated by a one minute interval. There is no colour contrast between the reactants but the precipitate formed is a dark blue colour, so the interface can be seen. The interface destabilizes to form a finger that moves down through the packed bed. The production of precipitate in the system has increased the rate at which these density instabilities form due to the decrease in porosity. When considering that it takes several minutes to set up an experiment for imaging in the spectrometer, and that an increased concentration of glycerol would increase the occurrence of these instabilities[10], an alternative method is required for the flow experiments. Therefore all experiments were carried out with the more viscous fluid now being the lower fluid and flow is applied from the top of the packed bed. Gravity is now a stabilizing factor[10]. Therefore the velocity required for instabilities to form is increased (eq 4.2).

4.2.2 Influence of flow rate

In Figure 4.3 a time series of photographs shows the displacement of 0.03 M of potassium hexacyanoferrate in a 50% glycerol solution by 0.03 M solution of iron nitrate. The flow rate is set to 1ml/hr and applied in the direction of gravity. The dark regions indicate the formation of precipitate. Initially a band of precipitate is formed at the interface between the two reactants (image (a)).

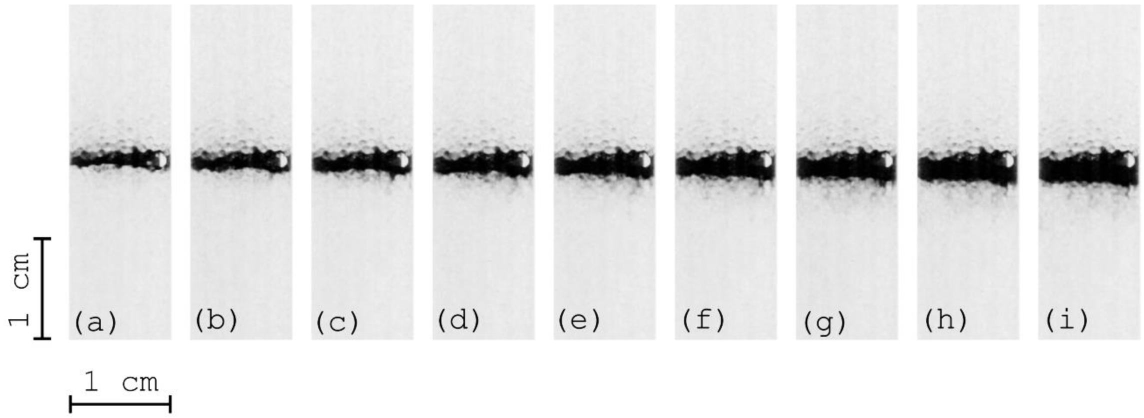

Figure 4.3: A time series of photographs displayed at 1 minute intervals, for the displacement of 0.03 M of potassium hexacyanoferrate in a 50% glycerol solution by 0.03 M solution of iron nitrate with gravity, at a flow rate of 1 ml/hr. The dark band in the photographs is formed by the formation of precipitate at the reactive interface.

Over the course of the experiment the band of precipitate moves down through the packed bed, expanding in width. More precipitate forms as the experiment continues, due to the flow bringing more reactants into contact with each other. No instabilities are seen to form indicating that a flow rate of 1 ml/hr is not sufficient to counteract the stabilizing influence of gravity.

In Figure 4.4 the experiment is repeated, with the flow rate increased to 9 ml/hr.

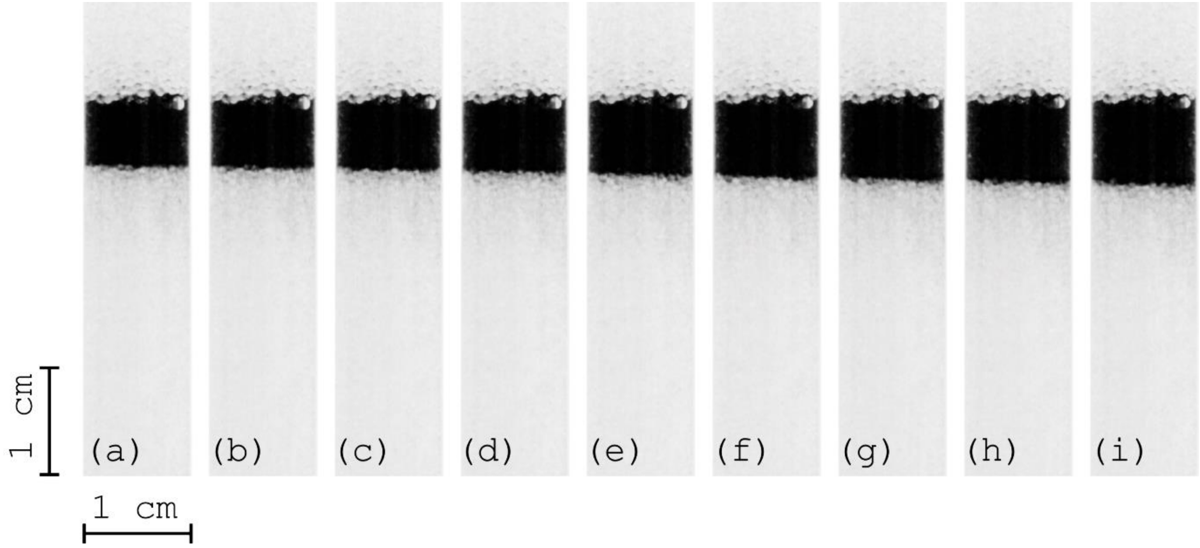

Figure 4.4: A time series of photographs displayed at 1 minute intervals, for the displacement of 0.03 M of potassium hexacyanoferrate in a 50% glycerol solution by 0.03 M solution of iron nitrate with gravity, at a flow rate of 9 ml/hr. The dark band in the photographs is formed by the formation of precipitate at the reactive interface.

Again no instabilities develop, however the band of precipitate is again seen to shift down through the packed bed and expand in width over the course of the experiment, this time at a greater rate. What can be seen below the band of precipitate are regions that appear slightly darker than the reactant solution. Little detail can be extracted with such low contrast, but it could be attributed to a very small deposition of precipitate. This would imply that there is a reactive interface moving beyond the main band of precipitate seen in the images.

By increasing the flow rate to 30 ml/hr a distinct change is seen in the flow through the packed bed. In

Figure 4.5 a times series of photographs are shown for the experiment run at 30 ml/hr. In Figure 4.5 (a) a band of precipitate forms in the top third of the image.

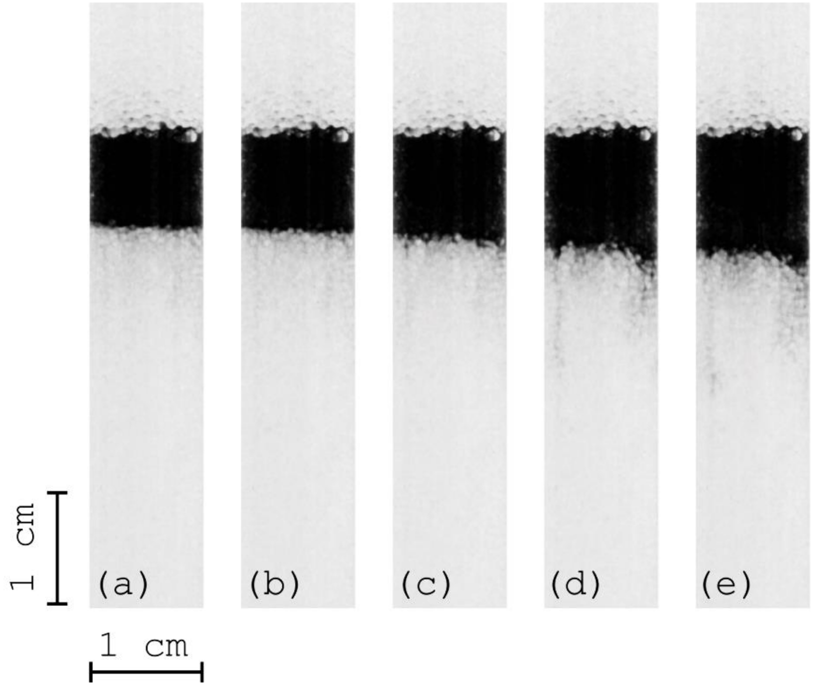

Figure 4.5: A time series of photographs displayed at 1 minute intervals, for the displacement of 0.03 M of potassium hexacyanoferrate in a 50% glycerol solution by 0.03 M solution of iron nitrate with gravity, at a flow rate of 30 ml/hr. The dark band in the photographs is formed by the formation of precipitate at the reactive interface. Instabilities are seen below the band of precipitate.

Just below the lower interface slightly darker regions are seen in the packed bed. In image (b) the precipitate band moves down only slightly but still there is little indication of instability formation. Some structure, however, is seen to be developing in image (c). On the left hand side of the packed bed there is a darker region that forms below the precipitate layer. Down the wall of the packed bed the same formation is seen to the right hand side of the image. In image (d) the fingers forming in the packed bed become clearer. A narrow finger, accelerating ahead of the precipitate band is seen on the left hand side of the image. A broader, slower moving finger develops down the right hand side of the packed bed. In the final image of the time series, these instabilities have progressed further through the packed bed reactor and become darker in colour. This indicates a greater amount of precipitate has been formed, creating better contrast but also emphasising the development of instabilities.

Previous studies showed how the presence of the precipitate leads to a finer, branched structure than glycerol alone[3]. The clear effect on the nature of the instabilities cannot be fully evaluated in optical images for several reasons. Firstly, although at the interface optical contrast is very good, contrast where instabilities begin to form and only small amounts of precipitate are deposited is extremely bad. A large amount of image processing is required to see any instability that may form. Secondly, optical images only show any behaviour on the outer edges of the packed bed reactor. From the previous investigations carried out, the possible tortuous nature of fingers formed means that only limited information can be obtained from these optical images. In an attempt to gather more information on the effect of precipitate-forming reactions on finger formation, magnetic resonance studies were carried out.

4.2.3 Relaxation measurements

In order to image this system some form of MR contrast is needed. We investigated the relaxation times of each reactant in order to find a means of creating contrast for MR images.

Figure 4.6 shows the dependence of T_1 relaxations on the concentration of iron(III)nitrate and potassium hexacyanoferrate(II) in a solution of 50% glycerol. The potassium hexacyanoferrate(II) solution does not show a T_1 dependence with concentration. The iron(III)nitrate solution contains the paramagnetic Fe^{3+} and it can be seen that there is a concentration dependence of the T_1 relaxation time, as expected with the presence of a paramagnetic species. The T_1 time for 0.03 M Iron (III) nitrate was 0.1 ± 0.002 s, for 0.03 M potassium hexacyanoferrate(II) in 50% glycerol 0.37 ± 0.05 s. It is important to note that the paramagnetic nature of the Iron (III) nitrate results in T_1 and T_2 times which are extremely short and difficult to measure when using the concentrations required for the flow experiments. For this reason less concentrated solutions of iron (III) nitrate were used to obtain a series relaxation measurements that could be used to calculated the relaxation times for 0.03 M iron (III) nitrate.

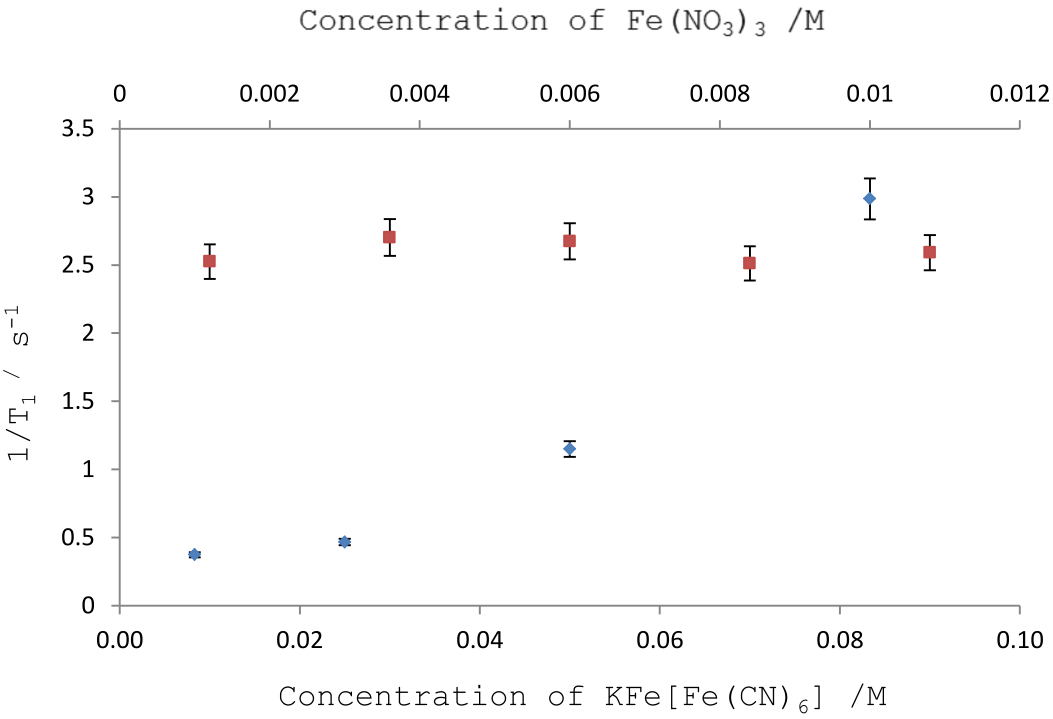

Figure 4.6: shows a plot of $1/T_1$ relaxation rates for water in potassium hexacyanoferrate(II), 🟥, and iron(III)nitrate, ◆, solutions.

Figure 4.7 displays the dependence of T_2 times for the two reactant solutions. Again no dependences is seen in the potassium hexacyanoferrate(II) solution but the T_2 relaxation of the water peak in the iron nitrate solution is reduced to 6 ms. The T_2 time for 0.03 M Iron (III) nitrate was 0.03 ± 0.001 s and for 0.03 M potassium hexacyanoferrate(II) in 50% glycerol 0.222 ± 0.002 s. A stoichiometric mixture of the two reactants gives a precipitate containing solution with a T_1 of 0.119 ± 0.01

s and T_2 of 0.09 ± 0.004 s showing that Iron (III) nitrate dominates the relaxation of the products.

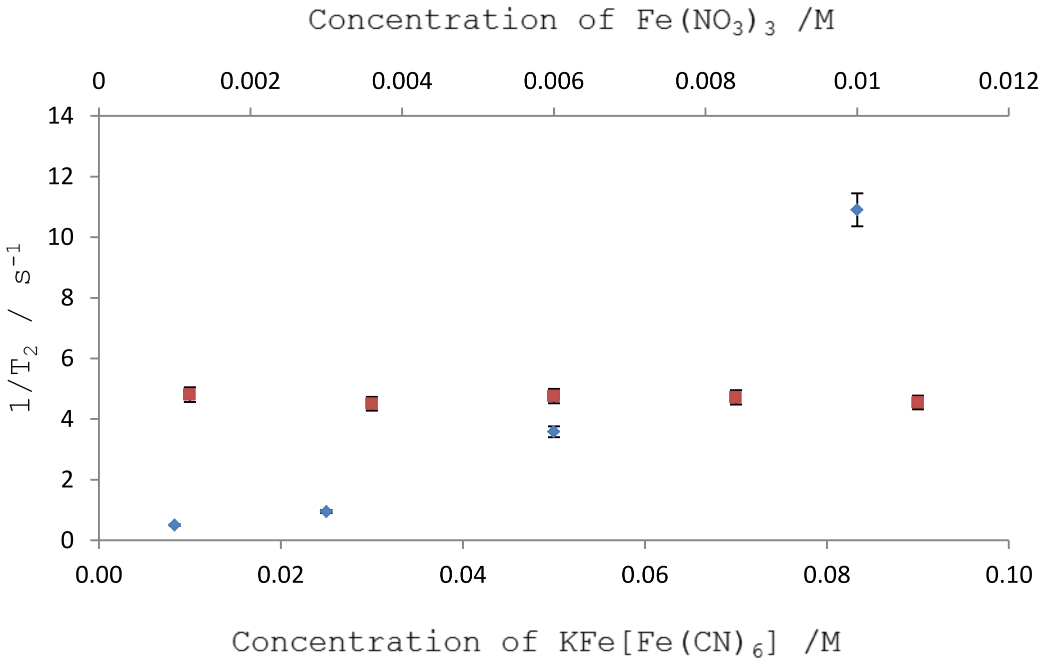

Figure 4.7: Shows a plot of $1/T_2$ relaxation rates for water in potassium hexacyanoferrate(II),🟥, and iron(III)nitrate, ◆, solutions.

From the relaxation points in Figure 4.6 and Figure 4.7 it can be seen that there is T_2 contrast between potassium hexacyanoferrate(II) and iron(III)nitrate, which can be used to provide image contrast. This enables the use of RARE[13] imaging, which uses differences in T_2 to create image contrast, and also reduces the overall experimental time.

4.2.4 Magnetic resonance Imaging

When initially carrying out MR imaging it became clear that the previously used setup was not well adapted to such experiments. It has previously been shown that the formation of precipitate can be considered instantaneous[3] upon mixing of the reactants. Therefore any movement of the interface will result in the broadening of the precipitate band, and with regards to T_2 weighted MR images, loss of signal. Due to the requirement to set up the interface prior to positioning in the spectrometer, due to being unable to add the packing material insitu and the amount of movement required to position the initial interface, it was found that the precipitate layer was expanded during the setup process. As the T_2 relaxation time for the products is short any region where the precipitate forms will have low signal. Therefore the spread of this region through the packed bed makes it unlikely that any MR contrast would be obtainable. For this reason a different packed bed was used, with a Teflon tap controlling the flow of the system. By closing the tap the interface was isolated from any external pressures that could alter the position of the interface. While this method prevented accurate selection of the flow rate, it was possible to accurately determine the flow rates after the experiments were carried out.

A packed bed was therefore setup with 1 mm borosilicate glass beads as packing, where 0.03 M solution of potassium hexacyanoferrate in 50% glycerol, high signal, filled the bottom half of the tube and a solution of 0.03 M solution of iron nitrate, low signal, was placed above this.

In Figure 4.8 a time series of images are shown, where each column of images are horizontal slices taken along the packed bed. Image (a) shows the packed bed initially filled with potassium hexacyanoferrate. In slices 4 and 5 of image (b) there are still high signal regions present but two instabilities are seen. The first in the top region of slice 5 where a broad area of low signal is seen. This finger can also be seen in slice 4 and 3 showing that the finger has developed down through the packed bed. The second finger is on the lower wall of the packed bed in slice 5 of image (b). This finger is not as broad as the first and when looking at slice 4 it can be seen that this instability is narrower and does not move down into slice 3. Due to the fast flow rate, any signal in the imaginable region of the r.f. coil is short lived meaning we can obtain little detail about how the fingers develop. In Figure 4.8 (e) a single optical image acquired immediately after the packed bed was removed from the spectrometer is shown. A darker region, indicating the formation of precipitate, is seen down the right side of the packed bed. A smaller finger is seen on the left side of the packed bed, although it appears that by this point in the experiment it has been shielded by the dominant finger and has almost been completely stabilised. A single finger has clearly dominated the flow and accelerated ahead through the packed bed. It is also clear that in the short period of the experiment the finger has travelled quickly down the packed bed. This single experiment shows clearly how a fast flow rate and the restricted observable region of the rf coil make acquiring any more than a snap shot of an instability extremely difficult.

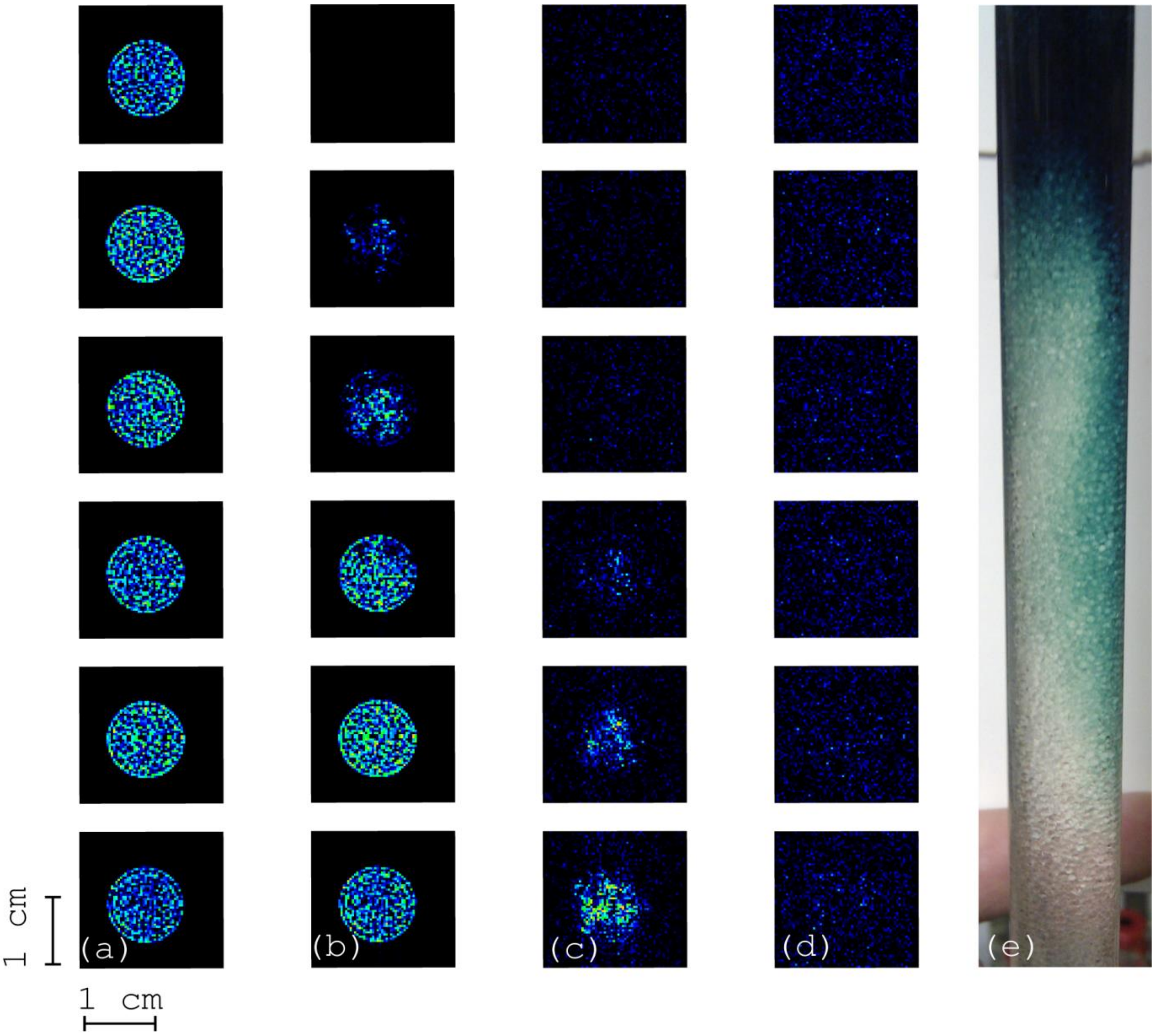

Figure 4.8:(a) to (d) show a time series of multiple horizontal MR images where of 0.03 M of potassium hexacyanoferrate in a 50% glycerol solution, high signal, is displaced by 0.03 M solution of iron (III) nitrate, low signal. Images are shown at 15 second intervals. The flow rate for this experiment was ~ 1.2 ml/min Image (e) shows a photograph of the packed bed reactor immediately after it was removed from the spectrometer.

To greater increase the possibility of capturing an instability forming the images were acquired at 10 second intervals. The experimental setup was kept the same, except the concentration of both reactants was increased to 0.05 M. This was done to increase the amount of precipitate formed, therefore increasing the influence on instability formation and so increasing the likelihood of fingers forming. In Figure 4.9 a time series of horizontal MR images is shown.

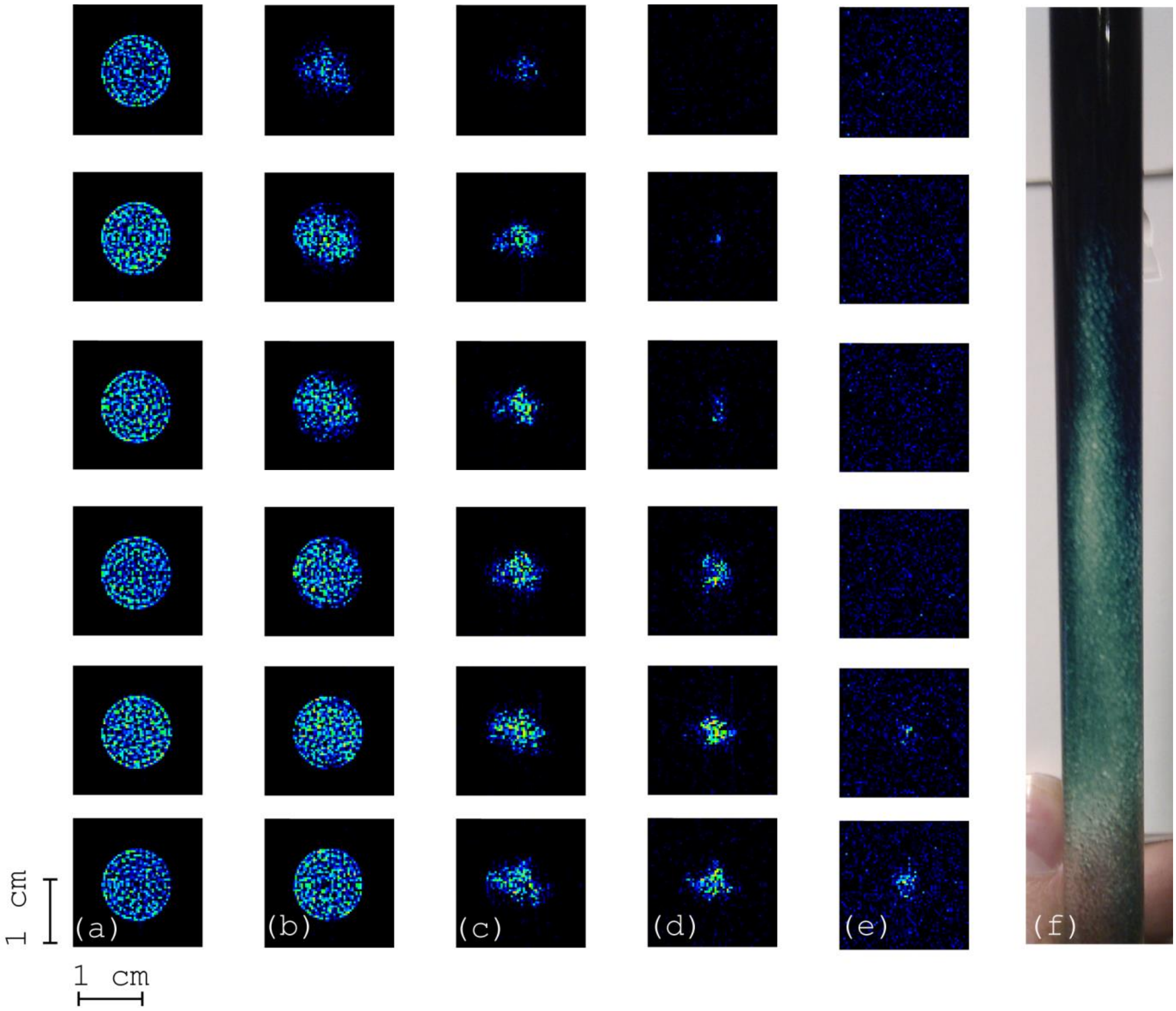

Figure 4.9 :(a) to (d) show a time series of multiple horizontal MR images where of 0.05 M of potassium hexacyanoferrate in a 50% glycerol solution, high signal, is displaced by 0.05 M solution of iron (III) nitrate, low signal. Images are shown at 10 second intervals. The flow rate for this experiment was ~ 1.7 ml/min Image (e) shows a photograph of the packed bed reactor immediately after it was removed from the spectrometer.

In the images shown in Figure 4.9, as can been seen from the optical snap shot shown in image (f), two distinct fingers develop down the sides of the packed bed. These fingers appear to have broadened over time and this can be seen in the MR images. In the center of the slices in images (c) and (d), an area of high signal is seen which shows a central region of glycerol and potassium hexacyanoferrate that is not being displaced but is gradually narrowing as the experiment continues. The higher concentration should produce more precipitate, reducing the porosity of the packed bed and result in more finger formation.

While it is possible to image this reactive system using MRI, it is not a simple undertaking and several problems hinder the capability of the technique to acquire useful information. The critical flow rate for finger formation was found, through optical imaging, to be 0.5 ml/min. Experiments carried out at this critical flow rate developed a dense band of precipitate, as seen in the optical images presented in this chapter. When carrying out MR imaging experiments the presence of a large band of precipitate caused image distortions that made it impossible to acquire any data from the MR images. These image distortions are caused by differences in the magnetic susceptibilities of the solutions and the solid precipitate. Through further MR experiments it was found that a minimum flow rate of 1 ml/min was needed to induce instability formation but also to disperse the precipitate through the packed bed reactor, reducing image artifacts. This fast movement through the observable region of the r.f. coil meant that any signal from the potassium hexacyanoferrate and glycerol solutions were short lived. Therefore only brief snapshots could be acquired of any instability formation. This creates a situation where precise control of the flow in the system is required. The flow rate must not be so low to enable a wide band of precipitate to form, but not be so fast that any signal from the potassium hexacyanoferrate solutions moves too quickly out of the observable region of the r.f. coil. This could be achieved with the use of a reverse syringe pump, which was unavailable through the course of these experiments. By using the syringe pump to draw the solutions from the bottom of the packed bed the same result would be achieved as when the tap was used, only with more controllability. The syringes in this type of pump are also locked in position, preventing the unwanted movement of fluid caused during the experiment setup to occur that would expand the width of the precipitate layer.

This said, some comparisons can be draw between this system and those previously studied in this thesis. Using an arrangement where gravity is now a stabilizing factor has shown that much higher velocities were needed to produce instabilities than when solutions of glycerol or CTAB and sodium salicylate are displaced against gravity. We have found through optical imaging that a critical flow rate of 30 ml/hr was required for any observable instabilities to form. This flow rate, however, was not viable for experiments carried out for MR imaging as an expanding band of precipitate formed during the experiments. The fingers seen to form in Figure 4.8 and Figure 4.9 show that by increasing the concentration of potassium hexacyanoferrate and iron nitrate from 0.03 M to 0.05 M the finger formation is altered. At the higher concentration of reactants, the formation of a second finger was more obvious with both fingers developing down through the packed bed. Whereas at the lower concentration of reactants, the presence of one dominating finger is seen in both the MR and optical images. Nagatsu *et. al* found that with an increased reactant concentration the fingers formed became more jagged, quickly changing direction due to the restrictive nature of the precipitate[3]. Here while we do see the increase in finger formation as concentration is increased we do not see such influence on finger structure. This is because much faster flow rates are used in this study. For the precipitate to alter the direction of flow the concentrations would need to be much higher, and the flow rates considerably lower.

While it is shown in this chapter that MR images of this system can be obtained, it is a difficult process that requires more controllable flow but also consideration to the differences in magnetic susceptibility between the packing, reactants and products.

4.3 Conclusion

We have used optical imaging to visualize the development of flow instabilities in a reactive system that resulted in the depositation of a precipitate at the interface between a more viscous and less viscous solution. It was found that viscous fingers only formed when a flow rate of 30 ml/hr or more was used due to the stabilizing effect of gravity.

MR images were acquired for the displacement of potassium hexacyanoferrate(II) in a solution of 50% glycerol by iron(III) nitrate. Due to the high flow rates required to produce instabilities, only a short time series of images could be acquired for each experiment. By increasing the concentration of reactants we were able to influence the formation of fingers, with higher reactant concentration leading to a higher number of instabilities being formed. To further investigate the effect of reactive concentration and flow rate on this system, an alternative experimental set up is needed.

4.4 References

1. Plante, L.D., P.M. Romano, and E.J. Fernandez, *Viscous Fingering In Chromatography Visualized Via Magnetic-Resonance-Imaging.* Chemical Engineering Science, 1994. **49**(14): p. 2229-2241.
2. Podgorski, T., et al., *Fingering instabilities of a reactive micellar interface.* Physical Review E, 2007. **76**(1): p. 016202.
3. Nagatsu, Y., et al., *Miscible viscous fingering with a chemical reaction involving precipitation.* Physical Review E, 2008. **77**(6): p. 067302.
4. Nagatsu, Y. and T. Ueda, *Effects of reactant concentrations on reactive miscible viscous fingering; Part 2, analytical study.* 6th World Multiconference on Systemics, Cybernetics and Informatics, Vol Xvii, Proceedings, 2002: p. 365-370.
5. Nagatsu, Y. and T. Ueda, *Effects of reactant concentrations on reactive miscible viscous fingering; Part 1, experimental study.* 6th World Multiconference on Systemics, Cybernetics and Informatics, Vol Xvii, Proceedings, 2002: p. 360-364.
6. Yuan, Q.S., et al., *Flow distribution in chromatographic columns.* Journal of Chromatography A, 1999. **831**(2): p. 149-165.
7. Broyles, B.S., et al., *Visualization of viscous fingering in chromatographic columns.* Journal of Chromatography A, 1998. **822**(2): p. 173-187.
8. Homsy, G.M., *Viscous Fingering in Porous Media.* Annual Review of Fluid Mechanics, 1987. **19**(1): p. 271-311.
9. Saffman, P.G. and G. Taylor, *The Penetration of a Fluid into a Porous Medium or Hele-Shaw Cell Containing a More*

Viscous Liquid. Proceedings of the Royal Society of London. Series A, Mathematical and Physical Sciences, 1958. **245**(1242): p. 312-329.

10. Saffman, P.G. and G. Taylor, *The Penetration of a Fluid into a Porous Medium or Hele-Shaw Cell Containing a More Viscous Liquid.* Proceedings of the Royal Society of London Series a-Mathematical and Physical Sciences, 1958. **245**(1242): p. 312-329.
11. Carr, H.Y. and E.M. Purcell, *Effects Of Diffusion On Free Precession In Nuclear Magnetic Resonance Experiments.* Physical Review, 1954. **94**(3): p. 630-638.
12. *www.magritek.com*.
13. Hennig, J., A. Nauerth, and H. Friedburg, *Rare Imaging - a Fast Imaging Method for Clinical Mr.* Magnetic Resonance in Medicine, 1986. **3**(6): p. 823-833.
14. Read, K.I., *Experimental investigation of turbulent mixing by Rayleigh-Taylor instability.* Physica D: Nonlinear Phenomena, 1984. **12**(1–3): p. 45-58.
15. Hill, S., *CHANNELLING IN PACKED COLUMNS.* Chemical Engineering Science, 1952. **1**(6): p. 247-253.

5 Bioconvection

The previous chapters of this thesis have focused on the coupling between flow and chemistry. In these systems it was found that chemistry could influence the flow and vice versa. Coupling however can also be observed between flow and biological systems, such as the behaviour of swimming microorganisms in flow. There has been much discussion of the effect of the swimming behaviour of these microbes[1-3] in their natural environment such as oceans, with much focus on the pure mechanics of their swimming motion[4-6]. Industrially, the behaviour and presence of this biomass shows importance, with hydrogen production[7]and biodiesel[8] both being potential future biofuels.

5.1 Algae

5.1.1 Taxis

While there are many types of microorganisms, motile cell have the ability to swim and can be influenced by external stimuli. The responses of microorganisms to these external stimuli are known as taxis. There are many types of taxis where responses to stimuli such as light and concentration gradients bias the swimming nature of the cells in order for them to occupy a more favorable environment[9]. While there are many different types of microorganisms and taxis, we look specifically at a species of algae known as *Chlamydomonas Augustae* which displays gyrotaxis.

5.1.1.1 Gyrotaxis

Gyrotaxis is the propulsion of a cell which is affected by gravitational and viscous torques[10]. It combines gravitaxis, where the trajectory of a swimming cell is determined by gravity, with rheotaxis, the orientation of a cell due to velocity gradients present in the environmental fluid[11].

5.1.2 ***Chlamydomonas Augustae***

Chlamydomonas Augustae (*c.Augustae*), shown in

Figure 5.1, is used as a model swimming organism[12]. This organism undergoes gyrotaxis due to its physical attributes.

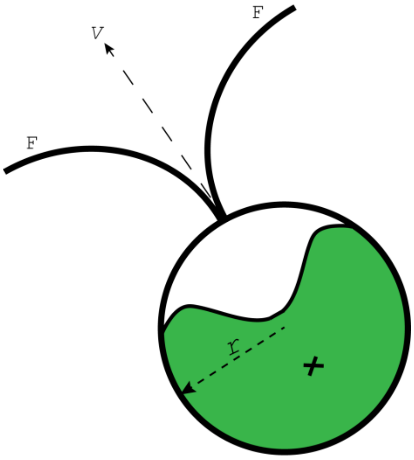

Figure 5.1: A schematic diagram showing the structure of a *Chlamydomonas Augustae* cell. The centre of gravity, x, is shift to the rear of the cell. The cell is propelled forward through its fluid environment by the beating of flagella, F.

The cells have a radius of 3-5 μm and are ~ 10% denser than the fluid which they occupy[13]. The heavy components of the cell, such as the chloroplast, are located at the posterior of the cell leading to the center of gravity, **x**, being shifted to the rear of the cell[13]. This makes the cell bottom heavy and orientates the flagella, **F**, which beat to provide propulsion, upwards. This enables the cells to swim upwards in the fluid. Any velocity in the fluid applies a torque on the cells and re-orientates the forward velocity of the cell. This enables the cells to move towards down-welling flow and away from up-welling flows.

5.1.2.1 Pattern formation

Chlamydomonas also display negative phototaxis[14] whereby they swim away from strong light and towards weak light. It is this behavior that results in the pattern formations as shown in Figure 5.2, as the cells gather together to avoid strong light.[9]

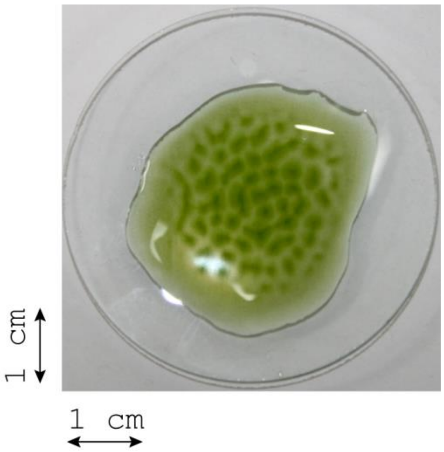

Figure 5.2: A cell suspension of *c.Augustae* at a concentration of 7 × 10^5 cells/ml when left unstirred in a thin layer formed bioconvection patterns.

This behaviour, known as bioconvection[14, 15], can occur in thin fluid layers as previously shown, but also in fluid systems not containing flow. In Figure 5.3 a time series of photographs show the development of bio-convection patterns. A well-mixed suspension of *Chlamydomonas Augustae* left unstirred over time begins to show pattern formation. As cells accumulate to avoid strong light, bioconvection patterns begin to form in the fluid. This behaviour occurs in conjunction with the upward swimming motion of the cells. As the cells self-concentrate they begin to create down-welling regions due to being denser than that fluid of the suspension[16].

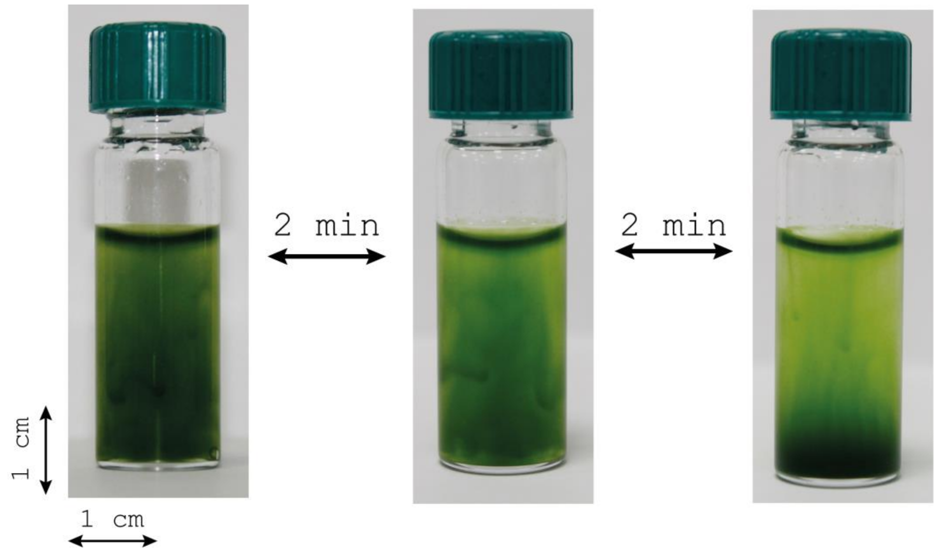

Figure 5.3: A cell suspension of *c.Augustae* at a concentration of 7 × 10^5 cells/ml when left unstirred in a 5 ml vial formed bioconvection patterns over time. Plumes were seen to form in the solution as the motile cells accumulated in down welling regions of fluid.

These down-welling regions create the velocity gradients required for gyrotaxis, therefore the cells continue to concentrate and the process of pattern formation continues.

5.1.2.2 Pattern formation under flow

Interest, however, is not purely into small scale occurrences of these patterns on the laboratory bench. Work has begun to use algae in industrial processes [7, 8]. For this the cell cultures are flowed through several pipe structures. As with all industrial processes it is important that all steps are as efficient as possible. Understanding how cell suspensions behave in flow environments aids in the improvement of these methods.

When placed in a vertical tube, where a down-welling flow is present, *Chlamydomonas Augustae* focus into a central beam along the vertical axis of the tube[13]. The specific flow in the tubes is poiseuille where the fluid at the center of the tube flows at a faster rate than the fluid at the tube walls. As the *C.Augustae* swim upward and cross the stream lines of the flow field they experience a torque (Figure 5.4 (a)). This re-orientates the cells so that they swim towards region of maximum velocity, the center of the tube, where they concentrate (Figure 5.4(b). As the cells are denser than the surround fluid the concentrated cells fall down through the pipe in a central beam (Figure 5.4 (c)).

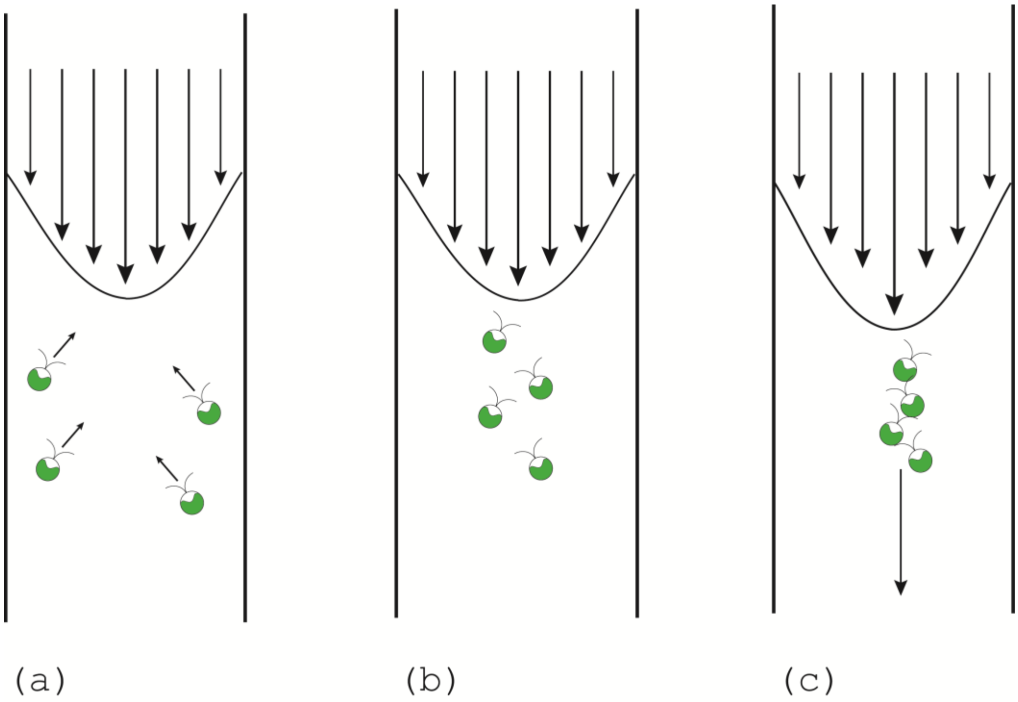

Figure 5.4: A schematic diagram showing the effect of poiseuille flow on the swimming motion of *c.Augustae.* Due to the downward poiseuille flow the cells experience a torque which changes the direction in which they swim. This results in the self-concentration of the cell at the centre of the pipe and the formation of bioconvection plumes.

The effect on the velocity within the system has been speculated on for some time now. Several methods have been employed to understand this system. Several theoretical methods have been used to model such systems[9, 16, 17]. Recently new theoretical methods have been used to model this flow[18, 19]. Although there is much modelling of the system there is still limited experimental work to support any of the suggested flow models. Experimentally, tracer particles have been used to monitor the velocities in such a system[20] with optical images used to monitor changes in the system.

Here we employ magnetic resonance velocimetry (MRV) in an attempt to provide precise velocity information with regards to the effect of the cells on the system. MRV has been applied to many areas such as engineering and medical imaging[21], and is able to provide detailed velocity information for systems ranging from the flow of fluid through a packed bed to the flow of blood through blood vessels. Most recently MRV was employed to image the flow of cytoplasm through a single plant cell[22].

Here we present the results from initial studies investigating the viability of using MRV to image flow deviation created by the motile cells.

5.2 Experimental procedure

5.2.1 Materials

5.2.1.1 Cell growth and concentration

Batches of *C.Augustae* (CCAP 11/51B) were grown by collaborators at Glasgow University using triple nitrogen Bold’s medium (3N-BBM)[23], a solution containing the nutrients required by the algae, and a 12/12 hour light/dark cycle. Cells were concentrated by placing loosely packed cotton wool in the top of the suspensions which trapped motile cells as they swam upwards. This process was allowed to continue for two days and then the cell containing cotton wool was transferred to plastic beakers and transported to Birmingham. The 12/12 light/dark cycle was maintained through all stages to prevent the cells becoming overtly sticky with regards to the experimental equipment[24]. Cells were further concentrated on the morning of the flow experiments by extracting the concentrated regions of cells from the cotton wool (Figure 5.5).

Figure 5.5: A photograph showing the accumulation of motile algae cells in cotton wool

On harvesting ~ 20 ml of solution the cell concentration was determined using a spectrophotometer (WPA CO7500) by recording the suspensions absorption at 590 nm. The cell concentration was found to be ~10^7 cells/ml. This was diluted using 3N-BBM, and a solution of concentration 7 × 10^5 cells/ml was made.

5.2.1.2 Experimental difficulties

Several problems were encountered when carrying out these experiments. Firstly the transportation of the algae from Glasgow to Birmingham was undesirable. The journey resulted in the algae experiencing a variety of temperature changes as well as a degree of mixing which would not be experienced in the laboratory. For easy transportation the cells were concentrated, which increased competition for nutrients and light within the system. This transportation also involved breaking the strict 12/12 light/dark cycle in which the cells were grown. All these variants resulted in a loss of motile cells before any flow experiments began. On average it could be said that ~ 20 % of the cells were lost through transportation. In addition to this the constant application of flow during the experiments also reduced the number of motile cells within the solution due to the delicate nature of the cells structure. It is clear that after running, on average, 4 flow experiments that little or no motile cells remained in the suspensions and fresh samples were required. If these experiments were to be continued or repeated in the future it would be advantageous to grow the cell cultures on site at Birmingham. This would reduce the ‘trauma’ experienced by the cells and enable experiments to begin with a more favorable cell population.

5.2.2 Experimental setup

Figure 5.6 shows the experimental setup for the flow experiments. A Perspex tube, 80 cm in length and with an i.d of 7 mm was used for all flow experiments. This tube was connected to two 100 ml glass syringes using PTFE tubing, with a dampener connected between the inlet and the driving syringe to eliminate pulsatile flow. The driving syringe was attached to a syringe pump (Harvard pump 22) to enable flow rates of 100, 200, 300 and 400 ml/hr to be applied to the system. To fill the tube the system was inverted and the syringe at the outlet used to fill the entire set up with the cell suspension. If the cells were seen to create plumes during this stage the cells were considered motile and the tube was placed in a Bruker DMX 300 spectrometer, operating at a ^{1}H resonance frequency of 300.13 MHz. After each flow experiment was run, the syringe connected to the outlet was used to mix/

refill the experimental setup without the need to remove the tubing from the spectrometer.

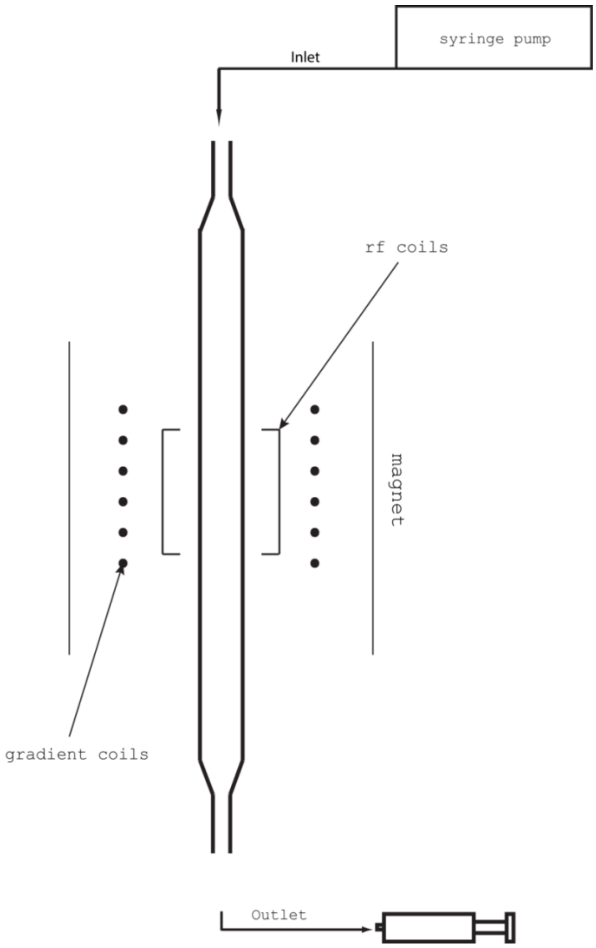

Figure 5.6: A schematic showing the experimental setup of bioconvection tube with respect to the magnet. The flow was applied from above using a Harvard apparatus(pump 22) syringe pump.

5.2.2.1 Magnetic resonance velocimetry

Horizontal velocity images were acquired using a VISEHS (**V**elocity **I**maging **S**pin **E**cho **H**ard **S**oft) in a 25 mm radiofrequency resonator pulse sequence, with a field of view of 12 mm × 12 mm, a pixel array of 64 × 64 and gaussian pulse was used to select a slice thickness of 2 mm. The 90° and 180° pulses were 42.88 and 85.76 μs respectively. 4 q slices were used in each experiment with the following parameter ranges **G** = 0.2 – 0.5 T m^{-1}, Δ = 10 – 24 ms and δ = 2 ms. The recovery time between each excitations was 1 s with 2 signal averages. The data acquired from each horizontal velocity image was azimuthally averaged to produce a single flow profile for each flow rate.

5.3 Results and discussion

5.3.1 Experimental considerations

There were several initial problems with imaging this system using MRV. The volume of cell culture required to continuous pump fluid during the duration of an MRV experiment was on the limits of what could be produced. This meant that velocity images need to be acquired in the shortest possible time. By reducing the number of acquisitions made during the experiment it was possible to run the experiments with the volume of cell culture available. However the velocity images acquired had a reduced signal-to-noise ratio and further analysis was required to enable interpretation of the data.

5.3.1.1 Azimuthally averages

To acquire data form the velocity images azimuthally averages were taken of each image. This was done by taking a profile from the center to the outer edge of a horizontal image and then repeating this process, moving around the central point of the image. These profiles were then averaged to improve the signal-to-noise ratio and enable features in the velocity profiles to be seen.

5.3.2 Velocity profiles

Initially, the experiments were carried out without the presence of the cells. The BBM medium was used to run the experiments in order to confirm that there were no deviations from poiseuille flow. In Figure 5.7 the azimuthally averaged velocity profiles for the control experiments at 200, 300 and 400 ml/hr are shown.

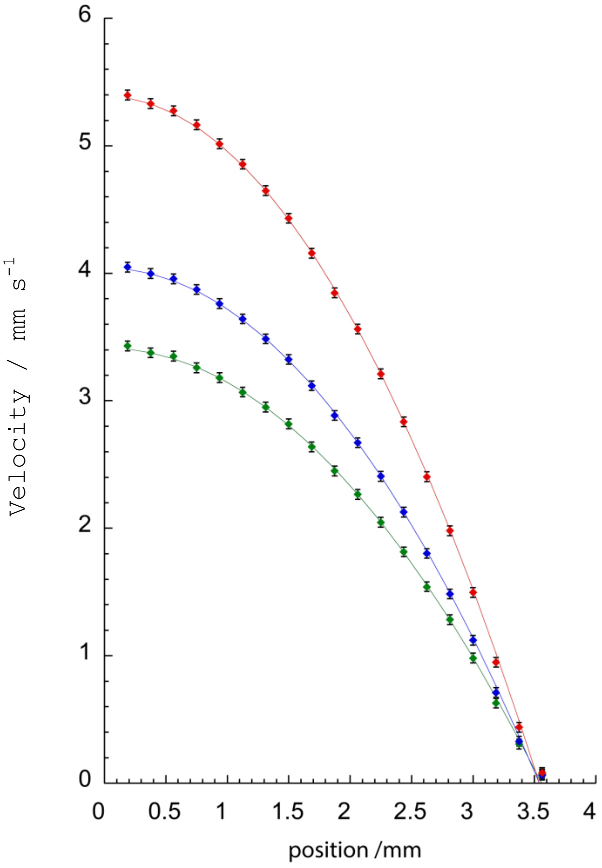

Figure 5.7: A plot of azimuthally averaged velocity profiles of BBM medium pumped through a tube of inner diameter 7 mm at flow rates of 200 ml/hr (green), 300 ml/hr (blue), 400 ml/hr (red). The solid line show the theoretical poiseuille flow for each flow rate. Error bars correspond to standard deviation.

These velocity profiles are shown with the theoretical velocity profiles expected for poiseuille flow at each given flow rate. The theoretical poiseuille plots were generated by using a simple macro to fit data to poiseuille equation[25]. The experimental data can be fitted to the poiseuille flow showing that the BBM medium used in the experiment does not cause any deviation from poiseuille flow.

It would be expected that both cell concentration and flow rate would affect the flow through a pipe. In this preliminary study we present the effect of increased flow rate on any deviations seen from poiseuille flow. In Figure 5.8 the azimuthally averaged flow profiles with *C.Augustae* in BBM medium have been plotted along with the calculated profiles for poiseuille flow at each given flow rate. Experiments at 200 ml/hr and 300 ml/hr were repeated twice and one experiment was run for 400 ml/hr. At all flow rates it can be seen that the experimental flow profiles no longer fit poiseuille flow. At the centre of the pipe, positions less than 0.5 mm, the greatest deviation is seen for each flow rate. The experimental flow is fractionally faster towards the centre of the pipe than would be expected. This would indicate the presence of a bio convection plume. These plumes, created by the sedimentation of cells, are thought to increase the velocity at the centre of the tube. As these deviations from ideal poiseuille flow appear at all flow rates investigated, the deviations of each experiment from ideal flow is plotted to see any dependence on flow rate.

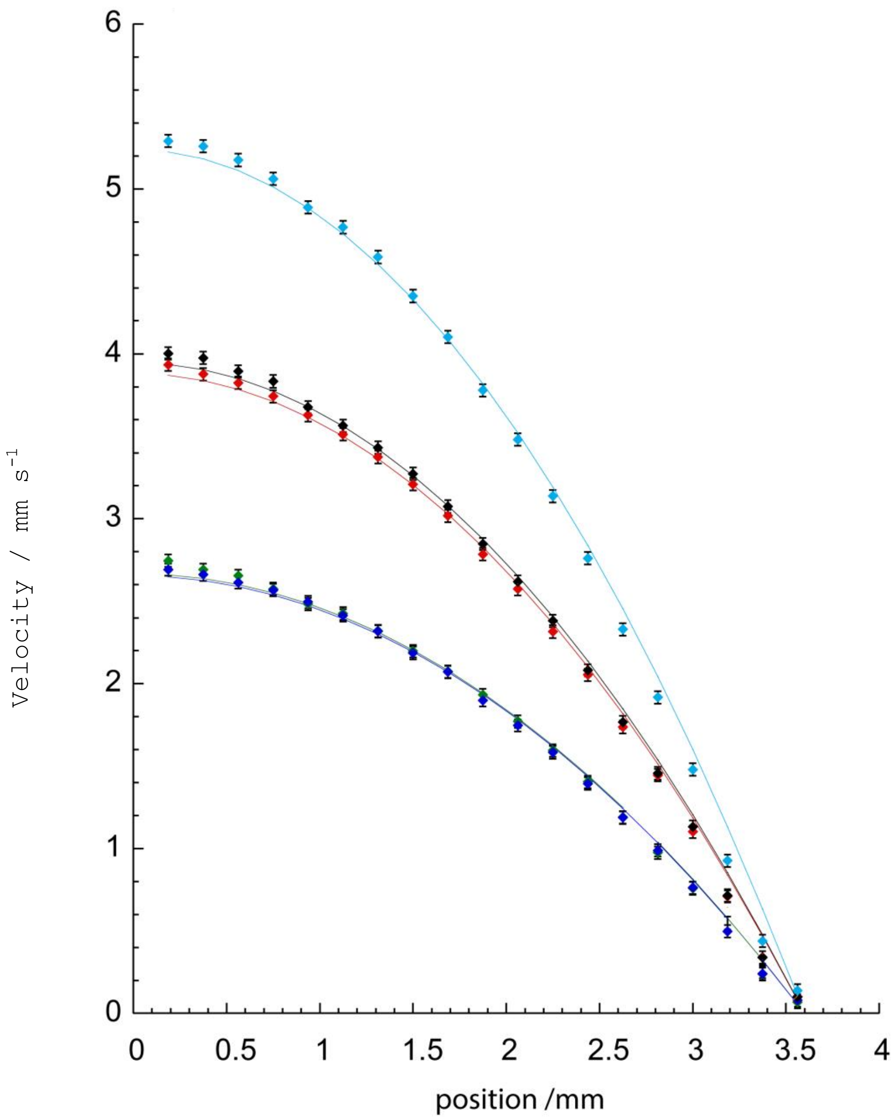

Figure 5.8: A plot of azimuthally averaged velocity profiles of a suspension of *C.Augustae* at concentration 7 × 10^5 cells/ml in BBM medium pumped through a tube of inner diameter 7 mm at flow rates of 200 ml/hr (dark blue & green), 300 ml/hr (black and red), 400 ml/hr (light blue). Where the solid line show the theoretical poiseuille flow for each flow rate. Error bars correspond to standard deviation.

5.3.3 Deviation of flow profiles from poiseuille flow

In Figure 5.9 the deviations from poiseuille flow are shown for the control experiments where only BBM medium was included.

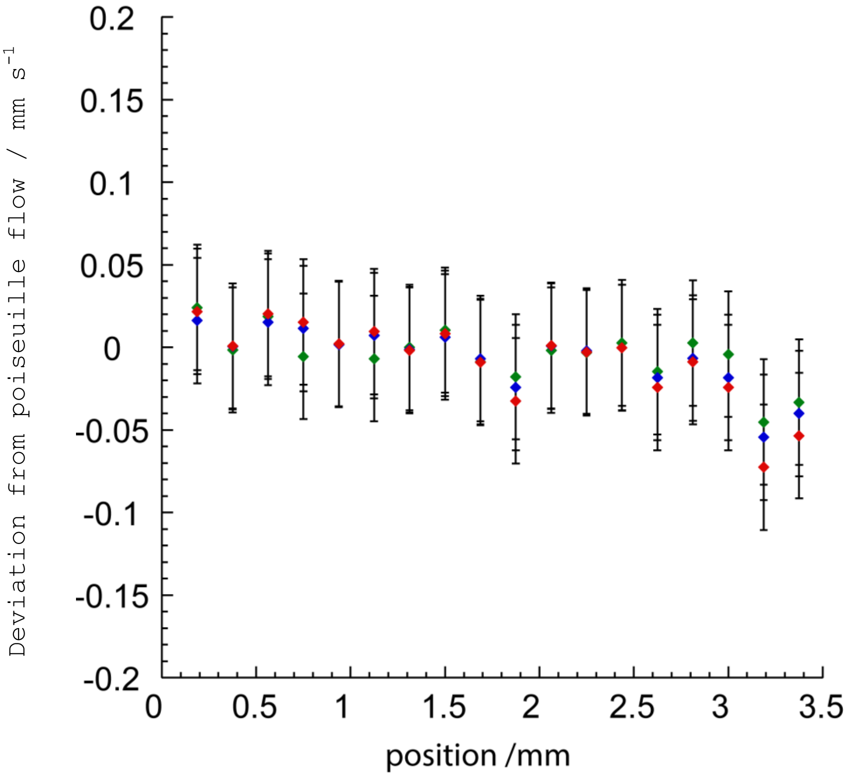

Figure 5.9: A plot show the deviation of experimental flow profile from poiseuille flow for experiment run with only BBM medium at a flow rate of 200 ml/hr (green), 300 ml/hr (blue) and 400 ml/hr (red). Error bars correspond to standard deviation.

Very little deviation is seen from the poiseuille flow. All deviations are less than ± 0.1 mms^{-1} showing that the experimental data fits well to the theoretical flow model.

In Figure 5.10 the deviations from poiseuille flow for the cell cultures at 200 ml/hr are shown. The deviation is greater than that seen in the blank experiments showing that the experimental data does not fit the theoretical profile as well. This shows that the inclusion of the cell culture has affected the flow within the pipe.

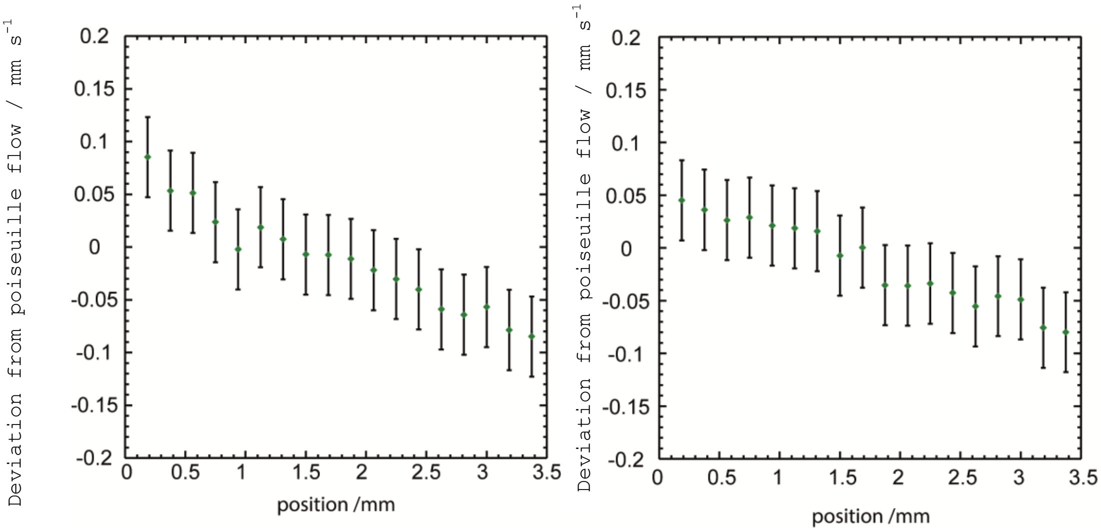

Figure 5.10: A plot show the deviation from poiseuille flow azimuthally averaged velocity profiles of a suspension of *C.Augustae* at concentration 7 × 10^5 cells/ml in BBM medium pumped through a tube of inner diameter 7 mm at a flow rate of 200 ml/hr from poiseuille flow. Two repeats are shown. Error bars correspond to standard deviation.

In Figure 5.11 the deviations plotted are now for experiments run at 300 ml/hr. The flow at the outer edges of the pipe has deviated by a greater amount than seen in the 200 ml/hr experiment. It could be determined that the increase in flow rate means that the cells in the flow system are exposed to greater torque emphasising the bioconvection plumes formed, and therefore resulting in a greater deviation of flow.

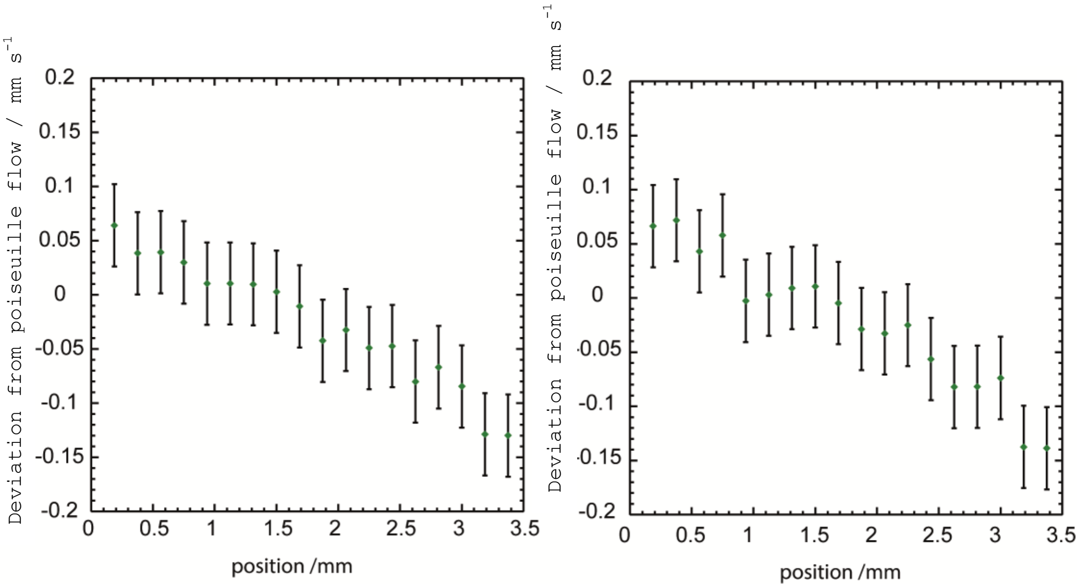

Figure 5.11: A plot showing the deviation from poiseuille flow of azimuthally averaged velocity profiles of a suspension of *C.Augustae* at concentration 7 × 10^5 cells/ml in BBM medium pumped through a tube of inner diameter 7 mm at a flow rate of 300 ml/hr. Two repeats are shown. Error bars correspond to standard deviation.

This would imply that increasing the flow rate emphasises the effect that the cells have on the flow. This effect however has not been previously been thoroughly investigated experimentally and further experiments would be necessary to confirm any trend seen here.

In Figure 5.12 the deviations of the flow are shown when a flow rate of 400 ml/hr is used. Again, the increase in flow rate has increased the deviation from poiseuille flow.

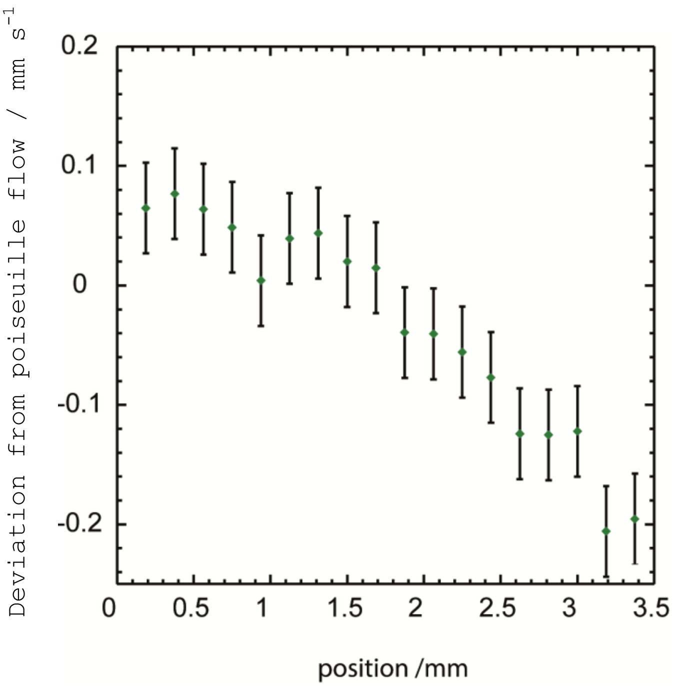

Figure 5.12: : A plot showing the deviation from poiseuille of flow azimuthally averaged velocity profiles of a suspension of *C.Augustae* at concentration 7 × 10^5 cells/ml in BBM medium pumped through a tube of inner diameter 7 mm at a flow rate of 400 ml/hr. Error bars correspond to standard deviation.

Although we do see some deviation from poiseuille flow when motile cells are included in the flow, these are only preliminary experiments and much more work would be required to fully assess the effect of including motile cells in flow and its dependence on flow rate concentration. Previous studies have investigated the effect of increase in cell concentration on the flow[26]. It has been found that increasing the cell concentration increases any deviation from poiseuille flow. From these preliminary studies MRV appears to be a viable experimental technique for investigating these effects, however a great deal more work is needed to fully investigate this flow instability. In all the plots presented here there can be seen, at the walls of the tubes, a negative flow. This deviation in flow was a potential flow feature which was predicted through previous modeling investigations[18]. The modeling carried out is still unable to predict why and how this flow feature may arise and the same model has provided solutions to the flow problem of bioconvection that does and does not show this negative flow. However some discussion has arisen as to whether this negative flow results due to a conservation of flow within the system whereby the fast, central, down-welling regions drives the fluid at the walls to produce a slight negative flow. The initial aim of these experiments was to confirm which theoretical model corresponded to the experimental data. From these initial experiments it is not possible to confirm the accuracy of either model. To provide more accurate data multiple repeats would be needed to confirm any trend. With the minimal number of experiments presented here it would be unsound to attribute these deviations in flow purely to the presence of the algae. Other factors such as the positioning of the experimental setup in the magnet, whether the tube was completely straight, the number of motile cells present and the conditions in which the cells had been kept could all influence the data acquired. The only viable method to confirm the initial results seen here would be to carry out multiple repeats of these experiments with the relocation of cell culture growth the same sit as all flow experiments were carried out. This would reduce many of the factors contributing the varied cell behavior which could occur.

5.4 Conclusion

MRV has been used to investigate the effect of motile cells on pipe flow. Preliminary experiments were carried out to assess the capability of this technique to detect any deviations in flow, caused by the development of bioconvection patterns. Velocity profiles were obtained for control experiments where BBM medium was pumped through a pipe. Azimuthally averaged flow profiles were compared to theoretical flow profiles at 200, 300 and 400 ml/hr. These control experiments were found to fit well with the theoretical flow profile. The experiments were repeated with a cell suspension of *Chlamydomonas Augustae* algae at a concentration of 7×10^5 cells/ml. The flow profiles for these experiments, run at 200, 300 and 400 ml/hr, were found to no longer fit poiseuille flow. The deviation of the experimental flow for each flow rate was plotted and it was found that greater deviation was seen at higher flow rates. This could be attributed to higher flow rates resulting in the cells experiencing a greater torque and so, emphasizing the formation of plumes which cause a deviation in flow. MRV has been demonstrated to be a useful technique in investigating the formation of bioconvection patterns. The next step in such studies would be to investigate the effect of changing the concentration of motile cells within the system.

5.5 References

1. Kunze, E., et al., *Observations of biologically generated turbulence in a coastal inlet.* Science, 2006. **313**(5794): p. 1768-1770.
2. Visser, A.W., *Biomixing of the oceans?* Science, 2007. **316**(5826): p. 838-839.
3. Leshansky, A.M. and L.M. Pismen, *Do small swimmers mix the ocean?* Physical Review E. **82**(2): p. 025301.
4. Guasto, J.S., K.A. Johnson, and J.P. Gollub, *Oscillatory Flows Induced by Microorganisms Swimming in Two Dimensions.* Physical Review Letters, 2010. **105**(16): p. 168102.
5. Rodenborn, B., et al., *Propulsion of microorganisms by a helical flagellum.* Proceedings of the National Academy of Sciences, 2013. **110**(5): p. E338–E347.
6. Be’er, A., et al., *Periodic reversals in Paenibacillus dendritiformis swarming.* Journal of Bacteriology, 2013.
7. Melis, A. and T. Happe, *Hydrogen production. Green algae as a source of energy.* Plant Physiology, 2001. **127**(3): p. 740-748.
8. Chisti, Y., *Biodiesel from microalgae.* Biotechnology Advances, 2007. **25**(3): p. 294-306.
9. Pedley, T.J. and J.O. Kessler, *Hydrodynamic Phenomena in Suspensions of Swimming Microorganisms.* Annual Review of Fluid Mechanics, 1992. **24**: p. 313-358.

10. Kessler, J.O., *Gyrotactic buoyant convection and spontaneous pattern formation in algal cell cultures*, 1984, plenum. p. 241.

11. Roberts, A.M., *Swimming and Flying in Nature*. Vol. 1. 1975: plenum.
12. Pedley, T.J. and J.O. Kessler, *Bioconvection.* Science Progress, 1992. **76**(299): p. 105-123.
13. Kessler, J.O., *Hydrodynamic Focusing of Motile Algal Cells.* Nature, 1985. **313**(5999): p. 218-220.
14. Wager, H., *On the effect of gravity upon the movements and aggregation of Euglena viridis.* Philos, trans R, Soc. London Ser B, 1911. **201**: p. 333-390.
15. Platt, J.R., *Bioconvection patterns in cultures of free swimming organisms.* Science, 1961(133): p. 1766-1767.
16. Kessler, J.O., *Individual and collective fluid dynamics of swimming cells.* Journal of Fluid Mechanics, 1986. **173**: p. 191-205.
17. Childress, S., *Pattern formation in a suspension of swimming micro-organisms:equations and stability theory.* Journal of Fluid Mechanics, 1975(69): p. 591-613.
18. Bees, M.A. and O.A. Croze, *Dispersion of biased swimming micro-organisms in a fluid flowing through a tube.* Proceedings of the Royal Society a-Mathematical Physical and Engineering Sciences, 2010. **466**(2119): p. 2057-2077.
19. Croze, O.A., E.E. Ashraf, and M.A. Bees, *Sheared bioconvection in a horizontal tube.* Physical biology, 2010. **7**(4): p. 046001-046001.
20. Denissenko, P. and S. Lukaschuk, *Velocity profiles and discontinuities propagation in a pipe flow of suspension of motile microorganisms.* Physics Letters A, 2007. **362**(4): p. 298-304.
21. Elkins, C.J. and M.T. Alley, *Magnetic resonance velocimetry: applications of magnetic resonance imaging in the measurement of fluid motion.* Experiments in Fluids, 2007. **43**(6): p. 823-858.
22. van de Meent, J.-W., et al., *Measurement of cytoplasmic streaming in single plant cells by magnetic resonance velocimetry.* Journal of Fluid Mechanics, 2010. **642**: p. 5-14.
23. Andersen, R.A., *Algal Culturing Techniques*2005: Elsevier/Academic Press.
24. Straley, S.C. and V.G. Bruce, *Stickiness to Glass - Circadian Changes in the Cell-Surface of Chlamydomonas-Reinhardi.* Plant Physiology, 1979. **63**(6): p. 1175-1181.
25. Callaghan, P.T., *Translational dynamics and magnetic resonance : principles of pulsed gradient spin echo NMR*2011, Oxford ; New York: Oxford University Press. xvii, 547 p.

26. Croze, O.A., E.E. Ashraf, and M.A. Bees, *Sheared bioconvection in a horizontal tube.* Physical Biology, 2010. **7**(4).

6 Conclusion

In this thesis research was presented that investigated the influence of chemically reactive interfaces and motile organisms on flow.

Both optical imaging and magnetic resonance imaging was used to follow the development of Saffman-Taylor instabilities in both reactive and non-reactive systems. The formation of a wormlike micelle layer when the surfactant, CTAB, and the co-surfactant, sodium salicylate, came into contact was studied. Both T_2 weighted images and RARE images were used to monitor the development of wormlike micelles over time. It was found that due to fast exchange occurring between the water and the sodium salicylate, the water peak in the sodium salicylate solution showed concentration dependence with regard to T_2 relaxation. This enabled the system to be imaged without the addition of an MR contrast agent. The flow rate was found to affect the structure of fingers under flow. An increase in flow rate broadened the fingers which developed and resulted in gradual stabilization of the interface. Both the displacement of sodium salicylate by CTAB and the displacement of CTAB by sodium salicylate underflow were investigated. Differences in finger formation were found, dependent on which orientation was used. The displacement of sodium salicylate demonstrated the fingers that underwent a greater deal of splitting and shielding. This could be attributed to the use of non-stoichiometric concentrations of reactants and possible differences in diffusion coefficients, leading to non-uniform development of the wormlike micelle layer. However, further investigation would be needed to confirm this. Image compression was used to improve our ability to present large volumes of 3-dimensional data, with several instances of finger splitting and shielding being identified. Root mean square pixel deviation analysis was carried out on the displacement of sodium salicylate through a packed bed. Using this analysis qualitative information was obtained from the 3-dimensional images. It was possible to identify the presence, shape and position of fingers through this analysis.

The displacement of Glycerol by a less viscous solution was investigated when the inclusion of a chemical reaction resulted in the depositation of a precipitate at the interface. The flow of this system through a packed bed was investigated through the use of optical images as well as MR images. Due to the stabilizing effect of gravity, higher flow rates were required for instabilities to form. This resulted in difficulties when acquiring MR images. The increase of reactant concentration resulted in a larger volume of precipitate being formed, and so a greater degree of instability development.

The Root mean square deviation analysis was carried out on a nonreactive flow system, where glycerol was displaced by a less viscous solution. From the plots produced, the identification of the instability formation was possible and further detail could be drawn about the structure of the instabilities.

MRI was also employed to investigate the relationship between motile micro-organisms and flow. Through the use of MRV, we were able to show that when the algae, *Chlamydomonas Augustae*, is pumped through a pipe in the direction of gravity, deviation from poiseuille flow is seen. The self-concentrating nature of *Chlamydomonas Augustae* results in the formation of bioconvection plumes through the pipe. These plumes increase the velocity of the fluid where they form, resulting in this deviation from poiseuille flow. By azimuthally averaging flow profiles from the velocity images acquired, we were able to show that a concentrated solution of *Chlamydomonas Augustae* increased velocity at the centre of the pipe. An indication that increased flow rate increased this effect was seen. However further studies would be need to confirm any trend with both flow rate and cell concentration being investigated.

In conclusion we have used several MR imaging techniques to monitor and explain the development of flow instabilities in a variety of systems. A new root mean square analysis technique was developed and applied to the MR images acquired of Saffman-Taylor instabilities to further clarify the development of such instabilities.

6.1 Future work

To develop on the work presented in this thesis several investigations would be suggested. The development of the wormlike micelle layer has been shown to alter dependence on the arrangement of reactants when investigating the formation of instability between CTAB and sodium salicylate. By carrying out diffusion measurements on these reactants it would be possible to further understand the development of the wormlike micelle layer and the affect that altering reactant concentrations and arrangements would have.

We have shown that MRV can be used to understand the formation of bioconvection patterns in flow. However, further experiments would be needed to understand the deviation in flow caused by these motile cells. Further investigation is also needed to understand the effects of flow and cell concentration on these flow instabilities.

While we have shown the ability of MRI to probe these flow systems we have also demonstrated its limitations, with a system involving the deposition of precipitate being troublesome to image due to magnetic susceptibility issues caused by the precipitate and the fast flow rates required. In future studies it would be recommended that an experimental setup where gravity is not stabilizing was used to reduce the flow rate required.

Appendix 1

The first macro included in this appendix was used to general a time series of model plug flow at a variety of flow rates.

```
pb=matrix(256,128,16)
pb=expt160Ft

s=49 #this is the initial postion of interface in 1st image

percent_1=matrix(256,128,16)

mod_1=matrix(256,128,16)
mod_2=matrix(256,128,16)
mod_3=matrix(256,128,16)
mod_4=matrix(256,128,16)
mod_5=matrix(256,128,16)
mod_6=matrix(256,128,16)
mod_7=matrix(256,128,16)
mod_8=matrix(256,128,16)
mod_9=matrix(256,128,16)
mod_10=matrix(256,128,16)
mod_11=matrix(256,128,16)
mod_12=matrix(256,128,16)
mod_13=matrix(256,128,16)
mod_14=matrix(256,128,16)

list_2=matrix(59532)

counter=0

F=2/3600 # flow rate in ml/hr to give volume flow rate in ml per s

t=152 #time for image aquisition and rest period

read_num=0 to 255
x=read_num

phase_num=0 to 127
y=phase_num

slice_num=0 to 15
slice=slice_num
z=slice

for slice_num=0 to 15
slice=slice_num
z=slice
   for y=0 to 127
      for (x=0 to 255)
      intensity=expt160Ft[x,y,z]#change expt#
      result_1=intensity>180000
      pb[x,y,z]=result_1
```

```
      next x
   next y

slice=slice+1
next slice_num

############################################################################
####

for slice_num=3 to 14
slice=slice_num
z=slice
   for y=45 to 85
      for (x=70 to 190)
      intensity=pb[x,y,z]
      result_1=intensity>0
      percent_1[x,y,z]=result_1
      if (result_1>0)
      list_2[counter]=1
      counter=counter+1
      endif
      next x
   next y

slice=slice+1
next slice_num

total=sum(list_2)
pr sum(list_2)

percentage=(total/59532)*100
pr percentage


pr F
area=0.7854 #area units=cm3

p=percentage/100 #porosity
pr p

V=F/(area*p)#cm per s
pr V

pixels =((V*t)*10)/0.156
pr  pixels

pr round(pixels)

a=round(pixels)

s1="smile"
pr s1

############################################################################
###
for slice_num=0 to 15
slice=slice_num
z=slice
 for y=0 to 127
```

```
      for (x=0 to 255)
      intensity=pb[x,y,z]
      if x<=s
      mod_1[x,y,z]=intensity
      elseif mod_1[x,y,z]=0
      endif
      next x
 next y
slice=slice+1
next slice_num

export3dpar("ab","binary","xyrc","real","fls","short","fileheader","0")
export3d("mod_1","mod_1")

s1="image 1"
pr s1


for slice_num=0 to 15
slice=slice_num
z=slice
 for y=0 to 127
      for (x=0 to 255)
      intensity=pb[x,y,z]
      if x<=s+a
      mod_2[x,y,z]=intensity
      elseif mod_2[x,y,z]=0
      endif
      next x
 next y
slice=slice+1
next slice_num

export3dpar("ab","binary","xyrc","real","fls","short","fileheader","0")
export3d("mod_2","mod_2")

s1="image 2"
pr s1

for slice_num=0 to 15
slice=slice_num
z=slice
 for y=0 to 127
      for (x=0 to 255)
      intensity=pb[x,y,z]
      if x<=s+a*2
      mod_3[x,y,z]=intensity
      elseif mod_3[x,y,z]=0
      endif
      next x
 next y
slice=slice+1
next slice_num


export3dpar("ab","binary","xyrc","real","fls","short","fileheader","0")
export3d("mod_3","mod_3")

s1="image 3"
```

```
pr s1

for slice_num=0 to 15
slice=slice_num
z=slice
 for y=0 to 127
      for (x=0 to 255)
      intensity=pb[x,y,z]
      if x<=s+a*3
      mod_4[x,y,z]=intensity
      elseif mod_4[x,y,z]=0
      endif
      next x
 next y
slice=slice+1
next slice_num

export3dpar("ab","binary","xyrc","real","fls","short","fileheader","0")
export3d("mod_4","mod_4")


s1="image 4"
pr s1

for slice_num=0 to 15
slice=slice_num
z=slice
 for y=0 to 127
      for (x=0 to 255)
      intensity=pb[x,y,z]
      if x<=s+a*4
      mod_5[x,y,z]=intensity
      elseif mod_5[x,y,z]=0
      endif
      next x
 next y
slice=slice+1
next slice_num

export3dpar("ab","binary","xyrc","real","fls","short","fileheader","0")
export3d("mod_5","mod_5")


s1="image 5"
pr s1

for slice_num=0 to 15
slice=slice_num
z=slice
 for y=0 to 127
      for (x=0 to 255)
      intensity=pb[x,y,z]
      if x<=s+a*5
      mod_6[x,y,z]=intensity
      elseif mod_6[x,y,z]=0
      endif
      next x
 next y
slice=slice+1
```

```
next slice_num

export3dpar("ab","binary","xyrc","real","fls","short","fileheader","0")
export3d("mod_6","mod_6")


s1="image 6"
pr s1

for slice_num=0 to 15
slice=slice_num
z=slice
 for y=0 to 127
      for (x=0 to 255)
      intensity=pb[x,y,z]
      if x<=s+a*6
      mod_7[x,y,z]=intensity
      elseif mod_7[x,y,z]=0
      endif
      next x
 next y
slice=slice+1
next slice_num

export3dpar("ab","binary","xyrc","real","fls","short","fileheader","0")
export3d("mod_7","mod_7")


s1="image 7"
pr s1

for slice_num=0 to 15
slice=slice_num
z=slice
 for y=0 to 127
      for (x=0 to 255)
      intensity=pb[x,y,z]
      if x<=s+a*7
      mod_8[x,y,z]=intensity
      elseif mod_8[x,y,z]=0
      endif
      next x
 next y
slice=slice+1
next slice_num

export3dpar("ab","binary","xyrc","real","fls","short","fileheader","0")
export3d("mod_8","mod_8")


s1="image 8"
pr s1

for slice_num=0 to 15
slice=slice_num
z=slice
 for y=0 to 127
      for (x=0 to 255)
      intensity=pb[x,y,z]
```

```
      if x<=s+a*8
      mod_9[x,y,z]=intensity
      elseif mod_9[x,y,z]=0
      endif
      next x
 next y
slice=slice+1
next slice_num

export3dpar("ab","binary","xyrc","real","fls","short","fileheader","0")
export3d("mod_9","mod_9")


s1="image 9"
pr s1

for slice_num=0 to 15
slice=slice_num
z=slice
 for y=0 to 127
      for (x=0 to 255)
      intensity=pb[x,y,z]
      if x<=s+a*9
      mod_10[x,y,z]=intensity
      elseif mod_10[x,y,z]=0
      endif
      next x
 next y
slice=slice+1
next slice_num

export3dpar("ab","binary","xyrc","real","fls","short","fileheader","0")
export3d("mod_10","mod_10")


s1="image 10"
pr s1

for slice_num=0 to 15
slice=slice_num
z=slice
 for y=0 to 127
      for (x=0 to 255)
      intensity=pb[x,y,z]
      if x<=s+a*10
      mod_11[x,y,z]=intensity
      elseif mod_11[x,y,z]=0
      endif
      next x
 next y
slice=slice+1
next slice_num

export3dpar("ab","binary","xyrc","real","fls","short","fileheader","0")
export3d("mod_11","mod_11")


s1="image 11"
pr s1
```

```
for slice_num=0 to 15
slice=slice_num
z=slice
 for y=0 to 127
      for (x=0 to 255)
      intensity=pb[x,y,z]
      if x<=s+a*11
      mod_12[x,y,z]=intensity
      elseif mod_12[x,y,z]=0
      endif
      next x
 next y
slice=slice+1
next slice_num

export3dpar("ab","binary","xyrc","real","fls","short","fileheader","0")
export3d("mod_12","mod_12")


s1="image 12"
pr s1

for slice_num=0 to 15
slice=slice_num
z=slice
 for y=0 to 127
      for (x=0 to 255)
      intensity=pb[x,y,z]
      if x<=s+a*12
      mod_13[x,y,z]=intensity
      elseif mod_13[x,y,z]=0
      endif
      next x
 next y
slice=slice+1
next slice_num

export3dpar("ab","binary","xyrc","real","fls","short","fileheader","0")
export3d("mod_13","mod_13")


s1="image 13"
pr s1

for slice_num=0 to 15
slice=slice_num
z=slice
 for y=0 to 127
      for (x=0 to 255)
      intensity=pb[x,y,z]
      if x<=s+a*13
      mod_14[x,y,z]=intensity
      elseif mod_14[x,y,z]=0
      endif
      next x
 next y
slice=slice+1
next slice_num
```

```
export3dpar("ab","binary","xyrc","real","fls","short","fileheader","0")
export3d("mod_14","mod_14")

s1="image 14"
pr s1
```

The second macro included in this appendix was used to calculate the RMS pixel deviation in each experimental image.

```
sub_2=matrix(256,128,16)
sub_3=matrix(256,128,16)

I=200000#intensity freshold#

list_1=matrix(1000000)
list_2=matrix(1000000)
list_3=matrix(1000000)
list_4=matrix(10000000)
list_12=matrix(100000)

h_expt040210_112_x=matrix(301)#
h_expt040210_112_y=matrix(301)#
h_expt040210_112_z=matrix(301)#
h_expt040210_112=matrix(301)#

counter=0
counter_1=0
a=counter+1

read_num=0 to 255
x=read_num

phase_num=0 to 127
y=phase_num

slice_num=0 to 15
slice=slice_num
z=slice

for slice_num=0 to 15
slice=slice_num
z=slice
   for y=0 to 127
      for (x=0 to 255)
      intensity=mod_3[x,y,z]#change number this is the model providing to
comparison#
      result_1=intensity>0
      sub_2[x,y,z]=result_1
      if (result_1>0)
      list_1[counter]=x
      list_2[counter]=y
      list_3[counter]=z
```

```
      list_4[counter]=1
      counter=counter+1
      endif
      next x
   next y

slice=slice+1
next slice_num

N=sum(list_4)
pr N

a=list_1.*list_1
b=list_2.*list_2
c=list_3.*list_3

pr sum(a)
pr sum(b)
pr sum(c)

rms_1=sqrt((sum(a))/N)
rms_2=sqrt((sum(b))/N)
rms_3=sqrt((sum(c))/N)

pr rms_1
pr rms_2
pr rms_3

counter=0
counter_1=0
a=counter+1

list_T=matrix(1200000)

read_num=0 to 255
x=read_num

phase_num=0 to 127
y=phase_num

slice_num=0 to 15
slice=slice_num
z=slice

for slice_num=0 to 15
slice=slice_num
z=slice
   for y=0 to 127
      for (x=0 to 255)
      intensity=expt_112Ft[x,y,z]#change number this should be the image
being analysed#
      result_1=intensity>I
      if (result_1>0)
      list_T[counter]=1
      counter=counter+1
      endif
      next x
   next y
slice=slice+1
```

```
next slice_num

T=sum(list_T)
pr T

l_1_1_112=matrix(T)#
l_2_1_112=matrix(T)#
l_3_1_112=matrix(T)#

counter=0
counter_1=0
a=counter+1

read_num=0 to 255
x=read_num

phase_num=0 to 127
y=phase_num

slice_num=0 to 15
slice=slice_num
z=slice

for slice_num=0 to 15
slice=slice_num
z=slice
   for y=0 to 127
      for (x=0 to 255)
      intensity=expt_112Ft[x,y,z]#change number#
      result_1=intensity>I
      sub_2[x,y,z]=result_1
      if (result_1>0)
      l_1_1_112[counter]=x#
      l_2_1_112[counter]=y#
      l_3_1_112[counter]=z#
      counter=counter+1
      endif
      next x
   next y

slice=slice+1
next slice_num


list_5=l_1_1_112-rms_1#
list_6=l_2_1_112-rms_2#
list_7=l_3_1_112-rms_3#

list_8=list_5.*list_5
list_9=list_6.*list_6
list_10=list_7.*list_7

list_11=sqrt(list_8+list_9+list_10)

s1="end of calculation"
pr s1

T_2=T-1
```

```
r=round(list_5)

s1="rounded list"
pr s1

counter_1=0
a=counter+1

for a=0 to 300
      for (x=0 to T_2)
      value=r[x]
      if a=value+150
      list_12[counter_1]=1
      counter_1=counter_1+1
      endif
      next x
   h_expt040210_112_x[a]=sum(list_12)#
   list_12[~]=0
next a

r=round(list_6)

s1="rounded list"
pr s1


counter_1=0
a=counter+1

for a=0 to 300
      for (x=0 to T_2 )
      value=r[x]
      if a=value+150
      list_12[counter_1]=1
      counter_1=counter_1+1
      endif
      next x
   h_expt040210_112_y[a]=sum(list_12)#
   list_12[~]=0
next a

r=round(list_7)

s1="rounded list"
pr s1

counter_1=0
a=counter+1

for a=0 to 300
      for (x=0 to T_2)
      value=r[x]
      if a=value+150
      list_12[counter_1]=1
      counter_1=counter_1+1
      endif
      next x
   h_expt040210_112_z[a]=sum(list_12)#
   list_12[~]=0
```

```
next a

r=round(list_11)

s1="rounded list"
pr s1

counter_1=0
a=counter+1

for a=0 to 150
      for (x=0 to 770)
      value=r[x]
      if a=value
      list_12[counter_1]=1
      counter_1=counter_1+1
      endif
      next x
   h_expt040210_112[a]=sum(list_12)#
   list_12[~]=0
next a

plot h_expt040210_112#

export1dpar("ab","ascii","xyrc","real")
export1d(h_expt040210_112,"hist_expt040210_112.txt")#

export1dpar("ab","ascii","xyrc","real")
export1d(h_expt040210_112_x,"x_expt040210_112.txt")#

export1dpar("ab","ascii","xyrc","real")
export1d(h_expt040210_112_y,"y_expt040210_112.txt")#

export1dpar("ab","ascii","xyrc","real")
export1d(h_expt040210_112_z,"z_expt040210_112.txt")#

s1="finished_112"#
pr s1
```

Appendix 2

Results from chapter 2 of this thesis were accepted for publication in the journal, Microporous and Mesoporous Materials[120].

A full copy of the paper can be found at http://www.sciencedirect.com/science/article/pii/S1387181113001133.